IMPLEMENTATION OF AN ADVANCED CONTROLLER STRATEGY TO EMULATE FLARE TRAJECTORIES IN A HARDWARE-IN-THE-LOOP SIMULATION ENVIRONMENT

by

Marietjie Blignaut

Submitted in partial fulfillment of the requirements for the degree
Master of Engineering (Electronic Engineering)

in the

Department of Electrical, Electronic and Computer Engineering
Faculty of Engineering, Built Environment and Information Technology

UNIVERSITY OF PRETORIA

February 2022

SUMMARY

IMPLEMENTATION OF AN ADVANCED CONTROLLER STRATEGY TO EMULATE FLARE TRAJECTORIES IN A HARDWARE-IN-THE-LOOP SIMULATION ENVIRONMENT

by

Marietjie Blignaut

Supervisor:	Prof J.D. le Roux
Co-Supervisor:	Dr F.R. Camisani-Calzolari
Department:	Electrical, Electronic and Computer Engineering
University:	University of Pretoria
Degree:	Master of Engineering (Electronic Engineering)
Keywords:	Controller strategy, DC motor control, feed-forward control, flare hardware model, flare trajectory, gain scheduling, Hardware-in-the-Loop Simulation, linear control, linear model, non-linear model, PD control

This study investigates the implementation of a controller strategy to emulate flare trajectories on a Hardware-in-the-loop Simulation (HILS) platform. Flares are employed as countermeasures in aerial defence systems and the counter-countermeasures abilities of missiles against flares can be evaluated on a HILS platform. The HILS platform in this article consists of a flight motion simulator for missile seeker movement simulation and a target motion simulator. The target motion simulator is the gimbal system mounted on an arm which simulates the aircraft in motion with an ejected flare in trajectory. The gimbal system consists of two gimbals which are each controlled with a dc motor and provides the ability to emulate flare trajectory.

The focus of this study is on the control of the two gimbals in the gimbal system in order to emulate flare trajectory. The gimbal system consists of two gimbals which differ in size, a smaller inner gimbal is fitted inside the bigger outer gimbal. The inner gimbal can be fitted with a wafer that relays a light source to be viewed by a guided missile unit. The inner gimbal emulates horizontal movement and the

outer gimbal emulates vertical movement. Each gimbal is actuated with its own dc motor. Current and position feedback are provided from each gimbal to a microprocessor. The microprocessor is inside the gimbal system and is used to control the two gimbals together to emulate flare trajectory. In this study both gimbals in the gimbal system are characterised during a process that involves implementation of a dc motor model with friction properties and other non-linear elements parametrised within the gimbal system. The characterised gimbals are then utilised for development of a control system.

The first step in the study is the investigation of flare dynamic models. A position set point in terms of flare trajectory is developed from the flare models. The position set point is converted for use in gimbal units. With the flare models, 1 m is represented with 5.3 *m*rad on the gimbals. The aim is to control both gimbals as accurately as possible. Accurate control is regarded as a moving Root Mean Square (mRMS) position error below 2.00 *m*rad in the gimbal system, or 0.377 m in the flare model. The second step is modelling each of the two gimbals with the aim of developing a controller for flare trajectory emulation. Controller development is the third and last step.

A non-linear simulation model is developed for each gimbal. The non-linear simulation model incorporates a dc motor characterisation process to determine gimbal system parameters. There are non-linear elements present within both gimbals, mostly attributed to friction in the mechanical system and the electrical harness connected to the outer gimbal. The non-linear elements are modelled with a parameter estimation process. In the parameter estimation process, only measurements from a certain range of input voltages is taken, due to the limited range of movement which is 330 *m*rad on the inner gimbal and 225 *m*rad on the outer gimbal. When the gimbals move too fast into limit switches, measurements are not possible. Therefore, only measurements within a certain range is taken into consideration for development of the simulation models. The mean fit of the non-linear simulation model on to the actual gimbal measurements is 94.17 % for the inner gimbal and 94.04 % for the outer gimbal.

The non-linear simulation models are reduced to simplified non-linear simulation models. The simplified non-linear simulation models each contain a non-linear gain function that approximates the non-linear elements which affects movement of the gimbals. The mean fit of the simplified non-linear simulation model on to the actual gimbal measurements is 91.86 % for the inner gimbal and 83.75 % for the outer gimbal. Lastly, linear simulation models are deduced from the simplified non-linear simulation models. The mean fit of the linear simulation model on to the actual gimbal measurements

is 48.09 % for the inner gimbal and 72.48 % for the outer gimbal. Controllers are then developed based on these models.

Three controller strategies are evaluated. At first, linear controllers are developed for the linear models, and evaluated on the other models, as well as the actual gimbals. A different controller is developed for each gimbal. On the inner gimbal, a Proportional (P) controller is implemented. On the outer gimbal, a P controller with a designed control transfer function is developed. This transfer function is designed using Root Locus and Bode plot tools in Matlab. These linear controllers deliver the least satisfactory results.

The required performance criteria is a maximum mRMS position error of less than 2.00 *m*rad. On the inner gimbal linear control gives a maximum mRMS position error of 3.50 *m*rad, and the outer gimbal a maximum mRMS position error of 7.05 *m*rad is achieved.

Next, non-linear control elements are included with linear control action in the form of gain scheduling. The non-linear parameters present with each gimbal form the base of the gain scheduling control. Gain scheduling aims to compensate for the non-linear parameters. The gain scheduling function is determined with the defined input voltage range. This controller is designed on the simplified non-linear model, and evaluated on the non-linear model as well as the actual gimbal. For the inner gimbal, gain scheduling is implemented with Proportional-Derivative (PD) control action and does not provide much of an improvement. The maximum mRMS position error is 3.08 *m*rad. For the outer gimbal, gain scheduling is also implemented with PD control action and shows improvement over linear control. When the gain scheduling function is extended beyond the defined input voltage range, further improvements on the outer gimbal is observed. The maximum mRMS position error reduces to 4.70 *m*rad.

Lastly, a controller is developed on the non-linear model. It is also evaluated on the actual gimbal. This controller should perform the best, as it combines linear and non-linear control actions from the other models and compensates for their shortcomings. This compensation is in the form of feed-forward control action, which increases response time of the controlling action. For the inner gimbal, feed-forward control is added with PD compensation which gives the best results, a maximum mRMS position error of 2.6 *m*rad. This does not meet the requirement of less than 2.00 *m*rad, but is still seen as good enough as the position error percentage increases from 0.6 % to 0.79 %, which is still

close to the flare trajectory on a HILS platform. For the outer gimbal, feed-forward control is added to the PD compensator with an extended gain scheduling function. This provides the best result of all the controllers, and performs even better than the inner gimbal controller. On the outer gimbal, a maximum mRMS position error of 1.47 *m*rad is obtained, which satisfies the requirement of less than 2.00 *m*rad.

This study contributes to control systems by detailing the system identification process in order to develop a suitable controller for a gimbal system actuated with dc motors. Methods for controlling hardware with non-linear elements that influence its operation are analysed. It allows implementation of a mathematical model in hardware in order to provide additional capability for countermeasures evaluation. It contributes to the HILS environment with development of a flare trajectory. This gives the HILS platform the ability to evaluate counter-countermeasures on missiles.

Although a single flare trajectory result is shown in this study it has the ability to showcase more flare ejection scenarios by following the same procedure as outlined in the modelling section. For future work, different flare trajectories can be implemented and evaluated on the hardware.

LIST OF ABBREVIATIONS

dc	Direct Current
DMC	Dynamic Matrix Controller
DSP	Digital Signal Processing
emf	Electromotive Force
FO	Fractional Order
FPU	Floating Point Unit
GA	Genetic Algorithm
GM	Gain Margin
HILS	Hardware-in-the-loop Simulation
IT2FNN	Type-2 Fuzzy Neural Network
KVL	Kirchhoff Voltage Law
LPV	Linear Parameter Varying
mRMS	moving Root Mean Square
PD	Proportional-Derivative
PI	Proportional-Integral
PID	Proportional-Integral-Derivative
PM	Permanent Magnet
PM	Phase Margin
PSO	Particle Swarm Optimisation
PWM	Pulse Width Modulation
RMS	Root Mean Square

TABLE OF CONTENTS

CHAPTER 1 INTRODUCTION

1.1 PROBLEM STATEMENT

1.1.1 Context of the problem

The context of the problem is to design a control system for the flare trajectory emulation on a Hardware-in-the-loop Simulation (HILS) platform for evaluation of countermeasures in an in-flight motion simulation facility.

The HILS platform allows testing of mathematical models on hardware in a physical environment (Khan and Kadri, 2013; Noda, Tsujita, Abiko, Sato and Nenchev, 2020). It combines mathematical models with mechanical systems which allows evaluation of inaccuracies such as friction and resistance present in the physical system, but not in simulation models (Dixit, Xu, Wang, Zhang, Jin, Zhang and Zhao, 2017). HILS allows realistic testing of the real world at a lower cost, in a reduced risk setting, and in a controlled environment (Hunter, Roe and Wu, 2010). It can lead to reduced development times (Corpino and Stesina, 2014). It is a simulation conducted in real time, and combines one or several of the physical elements with a real time software simulation (Buccella, Cecati and Latafat, 2012). Hardware simulations are an accepted technique widely used to develop control systems (Bacic, 2005).

HILS applications are found in different environments, such as the traffic control research industry (Bullock, Johnson, Wells, Kyte and Li, 2004; Stevanovic, Abdel-Rahim, Zlatkovic and Amin, 2009; Li, Kyte and Johnson, 2004; Hunter *et al.*, 2010), functional verification of small satellites (Corpino and Stesina, 2014), electric drives (Bouscayrol, 2008), as well as power electronics (Buccella *et al.*, 2012; Ren, Sloderbeck, Steurer, Dinavahi, Noda, Filizadeh, Chevrefils, Matar, Iravani, Dufour, Belanger, Faruque, Strunz and Martinez, 2011). HILS is popular in the automotive industry (Nissimagoudar, Mane, Gireesha and Iyer, 2020; Lin, Tseng and Tseng, 2006; Short and Pont, 2008), as well as in the

autonomous vehicles environment (Dixit *et al.*, 2017; Van der Auweraer, Anthonis, De Bruyne and Leuridan, 2013).

HILS is used for aerial vehicle flight planning (Al-Jarrah and Hasan, 2011). It has also been applied for several years in the seeker investigation and countermeasures evaluation research field (Schildkraut, Flanagan, Lewis and Dillon, 1988; Ben-David and Cabib, 1992; Robinzon, Motovilov, Mangoubi and Ben-David, 1993; Cole Jr. and Jolly, 1996; Courtney and Huber Jr., 1997; DiMarco, Kemper Jr. and Pringle, 1999; Gross, 1999; Morin and Lessard, 1999; Bacic, 2005). The function of the HILS platform is to facilitate countermeasures evaluations with guided missile seeker heads.

The hardware simulation in these facilities focus mostly on the infrared properties of the seekers and the target, and the influence of countermeasures on seeker performance in the spatial, spectral, and temporal fields. Ben-David and Cabib (1992) describes a facility that simulates infrared scenes controlled in an electro-optical system as would be observed by an approaching missile. Robinzon *et al.* (1993), Courtney and Huber Jr. (1997), and Cole Jr. and Jolly (1996) describe a scene generator with target and background effects that are used to evaluate infrared seekers. Their respective HILS facilities contain a flight motion simulator which addresses the motion of the seeker closing in on a target. Robinzon *et al.* (1993), and Courtney and Huber Jr. (1997) describe facilities that contain a dynamic flare simulation model, but does not emulate its trajectory. They place the flare with the correct spectral properties in the seeker field of view. The movement towards the seeker and attenuation is simulated with a dynamic neutral density filter. Before the use of the filter, a shutter was used to simulate the flare as decoy model into the seeker field of view (Courtney and Huber Jr., 1997). The facility described by Cole Jr. and Jolly (1996) also does not consider flare trajectory, but rather the target range and spectral properties.

The HILS platform in this study consists of two main components, a missile flight motion simulator and a target motion simulator. It is used for missile countermeasures and counter-countermeasures evaluation. The target motion simulator includes a flare motion simulator. The HILS facility has the capability to test missile guidance units by mounting them on the flight motion simulator. The flare motion simulator is part of the target motion simulator which mimics flight motion of the target. In-flight simulations can then be performed in the hardware environment for tests with missile guidance units. It is similar to the facilities described in Morin and Lessard (1999), Schildkraut *et al.* (1988), and Sidery and Pyle (2001). The target motion simulator simulates an aircraft in flight and a single

flare ejected from the aircraft.

Morin and Lessard (1999) describe a HILS facility for infrared seeker evaluation which incorporates a flare trajectory simulation that considers drag coefficient of the flare trajectory. They use the flare as decoy to develop target tracking algorithms on their missile seeker. Schildkraut *et al.* (1988) combines two infrared targets and a background with a beam splitter. A shutter is used to simulate rapid ignition of a flare, but the study focusses on the optics and does not investigate flare flight paths.

Sidery and Pyle (2001) employs mirrors with a motorised aperture system to represent the approaching movement of a seeker to an aircraft. Sidery and Pyle (2001) uses a countermeasures system with two channels which are each capable of moving in three dimensions. Light sources whose intensity can be controlled are applied as flares. The flare sources are controlled with mirrors and a shutter is employed which allows recycling of the flares to simulate a scenario with more than one flare. They do not focus on emulating flare trajectory, but just the speed and acceleration of the light sources in a straight line.

There is considerable literature on infrared properties of infrared imaging systems (Bingtao, Xiaorui, Yujiao, Zhaohui and Jianlei, 2015; Willers and Willers, 2012; Labonté and Deck, 2010), but less on the trajectory of flares (Zhang, Jia, Mkumbuzi and Wu, 2020; Willers and Willers, 2012).

Koch (2006) looks at different flare properties and characteristics. He and Baqar (2008) argue that flares are a simple and inexpensive countermeasures method. Koch (2006) does not evaluate flare dynamics in a mathematical model. Baqar (2008) states that conventional flares confuse heat-seeking missiles by appearing as a hot spot in the field of view of the missile. The missile confuses the heat signature of the flare with the heat signature of the aircraft and tracks the flare rather than the aircraft or actual target. Advancements in flare technology increase the ability to defend against missile attacks. According to Ragesh, Ratnoo and Ghose (2016) various parameters such as flare timing, velocity, direction, and the number of flares influence the effectiveness of flares as a defence tactic against missiles. There are studies that employ target tracking algorithms to implement counter-countermeasures against flares (Labonté and Deck, 2010; Ramaswamy, Vaitekunas, Gunter and February, 2017). These studies focus on discriminating between flare targets.

In the HILS platform of this study, the flare motion simulation system combines optics, mechanics,

and electronic hardware to recreate the image of an aerial vehicle on a cold background as seen by a missile seeker head during flight. Two gimbals, two dc motors, and optics are used to create the image of a flare exiting the aerial vehicle.

The focus of the study is on the control of two gimbals with dc motors to emulate flare trajectory. In order to develop a flare trajectory mathematical model, the kinematic model in Willers and Willers (2012) is used. It looks at the second law of Newton, as well as drag and flare characteristics. Wolff (2013), Polasek, Nemecek and Pham (2016), Mudau, Willers, Hlakola, le Roux, Theron, Calitz and Plooy (2011), Li, Hua, Wang and Ren (2016), and Jackman (2012) investigated simulation of flares and implementing flare trajectories in their simulations on software, but not in a HILS system.

Control strategies and methods are investigated in order to develop a controller for each gimbal that can deliver satisfactory results and emulate flare trajectory as accurately as possible.

1.1.2 Research gap

The research gap pertains to the development of flare path control on hardware. A flare mathematical model is implemented on two gimbals with the purpose of evaluating countermeasures in hardware simulations. The two gimbals which are modelled in this study exhibit non-linear traits that have to be considered in controller design. Controller strategies include conventional linear control strategies, like Proportional-Derivative (PD) control and feed-forward compensation, as well as non-linear controller strategies such as gain scheduling.

In the current field of countermeasures and guidance units, several studies investigate simulation of infrared signatures and images in an aerial environment (Zhou, Wang, Li and Hu, 2017; Wu, Lu, Zhao and Zhang, 2016). In the current work, simulations are carried out on a software platform to investigate flare measurements. This study will allow hardware implementation of flare path trajectories that will allow real-time testing of countermeasures on missile seeker heads and can contribute to developing HILS platforms and other countermeasures investigations (Xu, Li, Yang, Ju and Huang, 2016; Polasek *et al.*, 2016). To date, the author has not found similar studies on flare motion.

In this study, the results from the flare mathematical models and the developed controllers are utilized on a practical system that emulates flare trajectories.

1.2 RESEARCH OBJECTIVES AND QUESTIONS

The study aims to implement a controller on a hardware platform which will emulate the trajectory of a flare as it exits an aircraft within a HILS environment. The goal is to control two gimbals so that the flare trajectory can be emulated. The study aims to investigate controller strategies and develop them on gimbal models to obtain satisfactory results on hardware in a HILS countermeasures environment. A further goal is to develop three controller strategies on an embedded firmware processor and evaluate the controllers against each other.

The following statements describe the research questions:

- Investigate strategies to adapt a conventional control system to emulate flare trajectories in a HILS environment.
- Determine the suitability of applying said strategies on a practical system that includes two dc motors and one embedded processor to emulate flare trajectories.
- Determine if an advanced controller strategy is more effective than conventional controllers.

1.3 APPROACH

The proposed approach is to study linear and non-linear control system strategies and implement the strategies on existing hardware with the aim to emulate flare trajectories as accurately as possible on a HILS platform. The strategy includes modelling of systems with significant behavioural non-linear elements.

To emulate the trajectory of a flare, non-linear models of the two gimbals are initially developed. The non-linear elements of the non-linear model are then reduced to a simplified non-linear model. Model complexity is reduced in order to develop a linear model that is representative of the movement of the gimbals.

Three different controller strategies are developed based on the different models. The controller strategies differ in complexity as they are evaluated in simulation on the different models. The three controller strategies are PD control, gain scheduling control, and feed-forward control.

1.4 RESEARCH GOALS

The following items are listed as research goals:

- Develop a validated model to model each gimbal.
- Develop and evaluate suitable controllers for each gimbal.
- Test the developed controllers using the flare trajectories as set points on the actual gimbals.

1.5 RESEARCH CONTRIBUTION

The study contributes to the HILS environment and counter-countermeasures evaluation fields. It employs a mathematical model on simulation models in order to develop an efficient controller. The study shows how to identify non-linear elements present in a system, parametrise it and model it. It contributes to the non-linear control field with implementation of control with linear and non-linear elements. The results of this study were submitted to a peer-review journal:

- Blignaut, M., Camisani-Calzolari, F., and le Roux, J.D., (2021), Implementation of an advanced controller strategy to emulate flare trajectories in a Hardware-in-the-loop Simulation environment, *Mechatronics*, Submitted.

1.6 OVERVIEW OF STUDY

Section 2 contains theoretical information regarding flare trajectories and converts flare trajectory for use with the gimbal system as a set point. Section 3 applies information related to the modelling of the dc motors in modelling the gimbals in Simulink (Mathworks, R2020b). Three simulation models are developed for each gimbal, namely a non-linear model, a simplified non-linear model, and a linear model.

Section 4 takes a theoretical look at controller strategies. It shows development of different controller strategies on the different models. The different controllers are evaluated on the actual gimbals, and the results are compared. The study concludes with Section 5.

CHAPTER 2 OVERVIEW OF THE SYSTEM

In this section aspects related to the gimbal system are described. This comprises a description of the HILS platform in which the gimbal system fits. This section also describes flare models and flare trajectories which are applied as a set point for control of the gimbal system.

2.1 OVERVIEW OF THE HILS PLATFORM

A HILS platform provides the capability to perform real-time simulations in a laboratory environment. In this instance, aircraft countermeasures are evaluated against guided missile unit attacks. A flare is used as a countermeasure to protect an aircraft under missile attack. The actual guidance unit forms part of the simulation.

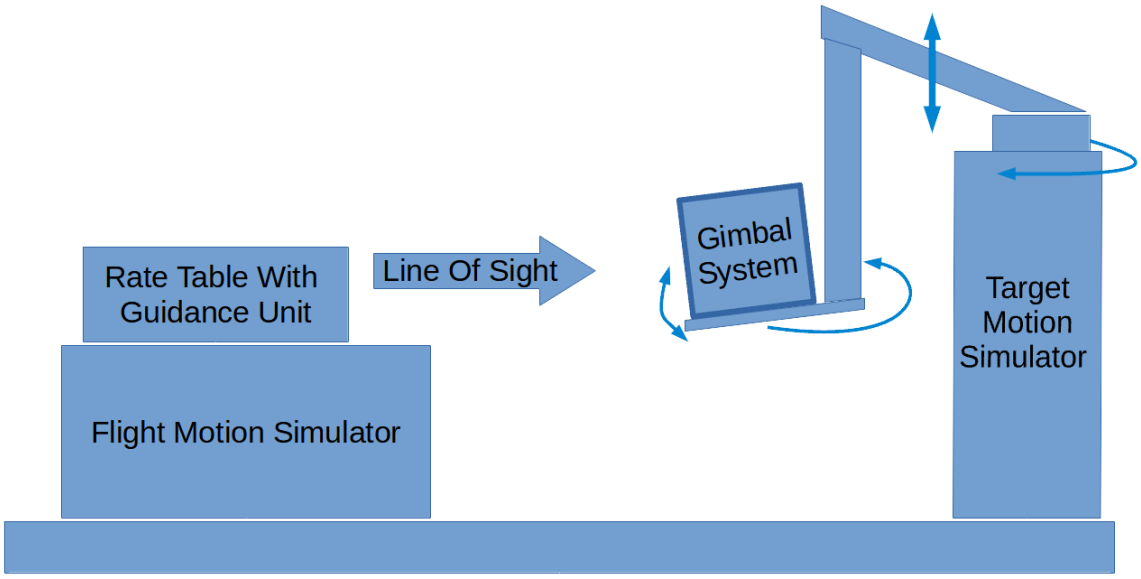

Figure 2.1. A diagram of the HILS platform which shows the mounting plate of the gimbal system which is considered for this study.

In this study a gimbal system is employed as a flare motion simulator on the HILS platform. A presentation of the HILS platform in Fig. 2.1 shows the target motion simulator with the plate on which the gimbal system fits. This is a typical HILS platform for such a study as shown in Carter and Willis (1998). This target motion simulator with gimbal system emulates an aircraft in flight from which one flare is deployed in the simulation. The target motion simulator can move the gimbal system with six degrees of freedom. In most simulations, however, the target motion simulation system has to move the gimbal system on the edge of a constant radius sphere while pointing the aperture of the gimbal system directly at the seeker which is situated in the center of the sphere. This movement emulates a target in the far field of the seeker. The gimbal system moves its mirror with an additional two degrees of freedom, namely yaw and pitch, to project a moving flare in the field of view of the seeker. The HILS platform also consists of a flight motion simulator which is fitted with a rate table on which a guidance unit can be mounted. This allows the simulation of a guidance unit in flight and evaluation of counter-countermeasures of relevant missiles in a laboratory set-up.

2.2 OVERVIEW OF THE GIMBAL SYSTEM

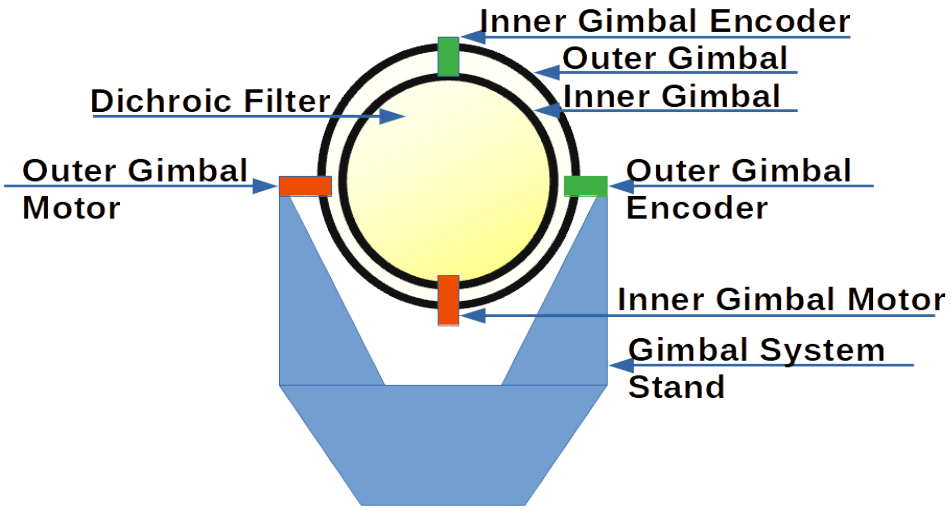

Figure 2.2. Two axis gimbal system with encoders and motors.

The gimbal system typically consists of two gimbals which can be controlled to facilitate a flare trajectory (Wein, Targove, Menikoff, Bowler and Korwan, 2011; Newport, 2021; CMM Optic, 2021).

Each gimbal has its own dc motor and encoder as shown in its depiction in Fig. 2.2. This is typical of such gimbal systems as seen in Wein *et al.* (2011), Newport (2021), and CMM Optic (2021). The system typically contains light sources that can represent an aircraft and the flare. The aircraft can deploy a flare, which allows evaluation of counter-countermeasures of different missiles in a laboratory set-up. This reduces the cost and risk associated with real life counter-countermeasures capability testing.

The inner gimbal is fitted with a dichroic filter that projects light sources from within the gimbal system to the rate table. The gimbal system has the ability to use a white light source with a cold plate to project the image of a plane in flight, as well as a high temperature source to project the flare ejected from an aerial vehicle. The gimbals are used to move the projection of the high temperature source to emulate flare trajectory, with the filter acting as a mirror. For the purpose of this study, none of the possible optic elements are used in developing motion control strategies.

Gimbal movement is used to emulate flare trajectory, and actuation of both gimbals show the flare trajectory in two dimensions. The movement of each gimbal is limited with limit switches to 330 *m*rad on the inner gimbal and 225 *m*rad on the outer gimbal. A motor driver is used to control the dc motors, which are fitted on each gimbal. The motors were chosen to actuate each gimbal and to provide the foundation for the system identification process. The driver provides each dc motor with -24 V to $+24$ V depending on a Pulse Width Modulation (PWM) index.

Feedback on the position of the gimbals as well as the status of the motors are provided in terms of position, rate, and current measurements. These measurements are used to develop the control system as well as to parametrise the gimbals for a Simulink simulation model. Position feedback for the control system is provided with a position sensor mounted on the axis of each gimbal. The rate of rotation is calculated using an α-β filter implemented in software on the microprocessor. Current consumption of each dc motor H-bridge driver is measured with a current sensor. The current can range from -4.095 A to $+4.095$ A. Communication with a desktop computer and communication with, as well as, control over all peripherals is facilitated with a microprocessor.

2.3 FLARE TRAJECTORY STUDY

In this section the dynamics of flare motion is studied. The results of this section are applied to establish the flare trajectory as position set points for each gimbal as shown in Fig. 2.2. In this application, flare motion is studied in two dimensions, horizontal and vertical. Horizontal motion is represented by movement of the inner gimbal. Vertical motion is represented by moving the outer gimbal.

2.3.1 Flare characteristics

The flare emulated in this study is an MTV (Magnesium-Teflon-Viton) 118 flare (Chemring, 2017). It is a flare chosen from a wide selection of flares available from the manufacturer website, e.g., MTV 218, M206, MJU-50A/B, KC-38 etc. The selection of the flare has no implied or historical significance beyond its use in this paper, and it was chosen to establish a set point trajectory for the control system. It is a flare built for its countermeasures capability against heat seeking infrared missiles. The flares are also known as infrared decoy instruments. The flare is manufactured using Magnesium, Teflon, and Viton materials that determine the pyrotechnic composition of the flare. The 118 refers to its calibre, $1 \times 1 \times 8$ inch or $25.4 \times 25.4 \times 203.2$ mm. The MTV118 has the following characteristics that are considered for the dynamic model and are derived from the data of the manufacturer (Chemring, 2017):

- Minimum burn time: $t = 2.5$ s
- Ejection velocity: $v > 30.48$ m/s

The ejection velocity is used with the ejection angle to determine the initial horizontal and vertical velocities. During its flight the flare will burn out, which reduces its effective physical mass and area during flight. Flare area is defined with $A(t)$ (m^2), and mass is defined with $m(t)$ (kg), where t indicates time (s).

The flare mass and area profiles were estimated as no measured data is available. The flare area and mass reductions are shown in Fig. 2.3 and described in (2.1). The shape of the graphs are deduced from work in Toothman and Loughmiller (1971), and Willers and Willers (2012), and information from the flare manufacturer (Chemring, 2017).

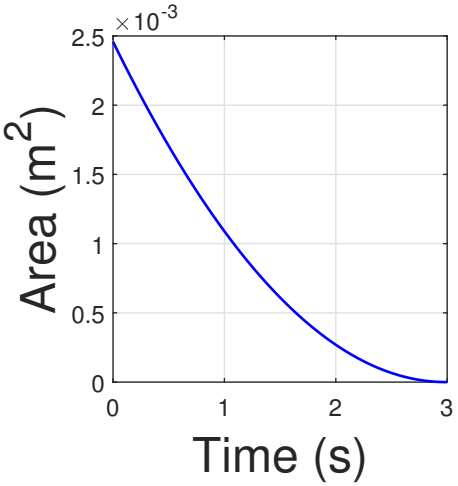

(a) Flare area reduction during flight.

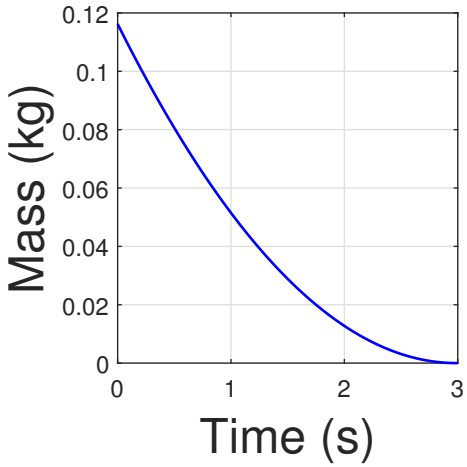

(b) Flare mass reduction during flight.

Figure 2.3. Flare area reduction, (a), and flare mass reduction, (b), over burn time.

These mass and area reductions over time are used in the flight dynamics calculations (for $0 \leq t \leq 3s$).

$$A(t) = 0.000275(t - 3.0)^2 \tag{2.1a}$$

$$m(t) = 0.013(t - 3.0)^2 \tag{2.1b}$$

Flares can be ejected under different scenarios, mainly at different heights and ejection angles. Although these will have to be considered and implemented in future for the target motion simulation system, a single ejection height of 3000 m and angle θ of 0 $^\circ$ was chosen for this study. The ejection angle is the angle at which the flare is ejected from the aircraft relative to the horizontal wing, positive upward. Further assumptions related to the flare motion in this study are based on the platform where it is utilised. These assumptions indicate that the flight of motion happens in two dimensions, with the aircraft flying in a straight line and that the flare is ejected in the vertical plane of flight of the aircraft. The flare is not tumbling and the flare geometry remains symmetrical with respect to the plane. The flare therefore travels in two dimensions, with horizontal and vertical flight components in the same plane as the aircraft, with no lateral forces acting on it.

2.3.2 Flare dynamics

The flare dynamics model is based on the flare aerodynamics estimation flight model in Willers and Willers (2012) and is a complex problem. The movement is analysed with the second law of Newton. Air turbulence is not included in this study. Therefore, turbulence velocity is not included in the dynamics model. Forces that influence the aerodynamic behaviour of the flare are gravitational force, drag force $F_d(t)$ (N), and the change in momentum due to initial ejection velocity. Drag force on the flare is calculated as

$$F_d(t) = 0.5\rho(h)C_dA(t)||v_r(t)||^2, \tag{2.2}$$

where $\lambda(t) = 0.5\rho(h)C_dA(t)$ (kg/m) denotes linear density, $\rho(h)$ (kg/m^3) is the air density at altitude h (m), C_d (-) is the drag coefficient of a long cylinder, and $||v_r(t)||^2$ (m/s) is the magnitude of the velocity vector in two dimensions. As there are two gimbals, the trajectory of the flare is modelled in the horizontal and vertical directions. The variables and constants related to the flare dynamics model are summarised in Tables 2.1 and 2.2.

Table 2.1. Nomenclature for flare trajectory modelling and dynamics variables

Variable	Unit	Description
$F_d(t)$	N	Drag force
$\rho(h)$	kg/m^3	Air density at altitude h (m)
$A(t)$	m^2	Physical area at time t (s)
$\lambda(t)$	kg/m	Linear density at time t (s) and altitude h (m)

Air density is derived as a function of altitude as shown here.

$$\rho(h) = \frac{M}{R(T_0 - Lh)}P_0\left(1 - \left(\frac{Lh}{T_0}\right)\right)^{\left(\frac{gM}{RL}\right)} \tag{2.3}$$

Here M (kg/mol) is the molar mass of dry air, R (mol.K) is the ideal gas constant, T_0 (K) is the sea level standard temperature, and L (K/m) is the temperature lapse rate. Sea level atmospheric pressure is indicated with P_0 (Pa). For the purpose of modelling, changes in the gravitational acceleration g (m/s^2) with regards to location and altitude is ignored and only an approximate value is used.

Table 2.2. Nomenclature for flare trajectory modelling and dynamics constants

Constant	Value	Description
g	9.81 m/s^2	Gravitational acceleration
C_d	0.82	Drag coefficient of a long cylinder
M	0.029 kg/mol	Molar mass of dry air
R	8.31 J/(mol.K)	Ideal gas constant
T_0	288.15 K	Sea level standard temperature
L	0.0065 K/m	Temperature lapse rate
P_0	101325 Pa	Sea level atmospheric pressure

The flare body dynamics model from Willers and Willers (2012) is modelled in three dimensions. In this study, there are only two gimbals and the flare dynamics model is adapted to two dimensions. The simplified version of the equation as derived from Willers and Willers (2012) is shown in (2.4). The x-axis contributes horizontal movement of the inner gimbal and the y-axis attributes vertical movement on the outer gimbal.

$$m\frac{d^2(x,y)}{dt^2} = +m(0,-g) + \frac{\rho(h)C_dA(t)}{2}||v_r(t)||^2\widehat{v}_r(x,y) \tag{2.4a}$$

$$v_r(t) = \frac{d(x,y)}{dt} \tag{2.4b}$$

In (2.4), (x,y) (m) is the location in space, $(0,g)$ is gravitational acceleration, which represents 0 m/s^2 in the horizontal x direction, and 9.81 m/s^2 in the vertical y direction, $m(t)$ (kg) represents the mass at time t (s), $\widehat{v}_r(x,y)$ (-) is the normalised direction vector of the flare velocity in each dimension.

The flare dynamics equations (2.4) are discretized using the Euler method as described by Edwards and Penney (2000). The fixed time step size is $\delta = 10$ ms. The discretized equations as shown in (2.5) calculates horizontal and vertical positions $x[k]$ and $y[k]$, velocities $v_x[k]$ and $v_y[k]$, as well as accelerations $a_x[k]$ and $a_y[k]$ during flight.

$$x[k+1] = x[k] + v_x[k]\delta + 0.5a_x[k]\delta^2 \tag{2.5a}$$

$$y[k+1] = y[k] + v_y[k]\delta + 0.5a_y[k]\delta^2 \tag{2.5b}$$

$$v_x[k+1] = v_x[k] + a_x[k]\delta^2 \tag{2.5c}$$

$$v_y[k+1] = v_y[k] + a_y[k]\delta^2 \tag{2.5d}$$

$$a_x[k+1] = -\frac{\lambda[k]}{m[k]} v_x[k] \sqrt{(v_x^2[k] + v_y^2[k])} \tag{2.5e}$$

$$a_y[k+1] = -g - \frac{\lambda[k]}{m[k]} v_y[k] \sqrt{v_x^2[k] + v_y^2[k]} \tag{2.5f}$$

The ejection height h and angle θ are used as inputs for (2.5). The ejection height is used to compute air density value $\rho(h)$ (2.3). Area, mass, and the linear mass density part of the drag force are calculated as shown in (2.6) and is obtained from (2.1) and (2.2).

$$\lambda[k] = 0.5\rho(h[k])C_d A[k] \tag{2.6a}$$

$$A[k] = 0.000275(k\delta - 3.0)^2 \tag{2.6b}$$

$$m[k] = 0.013(k\delta - 3.0)^2 \tag{2.6c}$$

The next step is to determine the polynomial functions for horizontal and vertical flare paths in order to arrive at a time dependent set point function for each gimbal control system.

2.4 FLARE MODEL

The flare dynamics models in (2.5) and (2.6) are used to calculate the flare trajectory polynomial equations. A lookup table was initially considered instead of polynomial functions. Polynomial functions were chosen to free up space on the processor. With HILS platform integration, the gimbal system receives commands from an external computer. The user can therefore define different flare trajectories, the external computer computes the trajectory and send the set-point through to the gimbal system. This functionality is configured on a graphical user interface. This is another reason why the functions were chosen as this is the format over which the gimbal system receives the set point information.

2.4.1 Polynomial approximation of flare trajectory

The initial horizontal velocity $v_x[0]$ is 30.48 m/s and vertical velocity $v_y[0]$ is 0 m/s. It is determined using the ejection angle and flare characteristics (Chemring, 2017). At the height of 3000 m, the initial air density is 0.9 kg/m^3. The initial physical area and initial mass as given by (2.1) is 0.002475 m^2 and 0.117 kg respectively. The mass at time step k is $m[k]$, the time step difference is $\delta = 0.01s$.

The air drag force is calculated with $F_d[k]$, as described in (2.2). To compute the trajectory without drag $\lambda[k]$ is set equal to zero. When computing the trajectory with drag $\lambda[k]$ is calculated as shown in (2.6a). Fig. 2.4 shows the flight path in the vertical and horizontal direction of the flare model with drag and without drag, using the given initial values. Drag influences the trajectory of the flare and is included in the flare trajectory model.

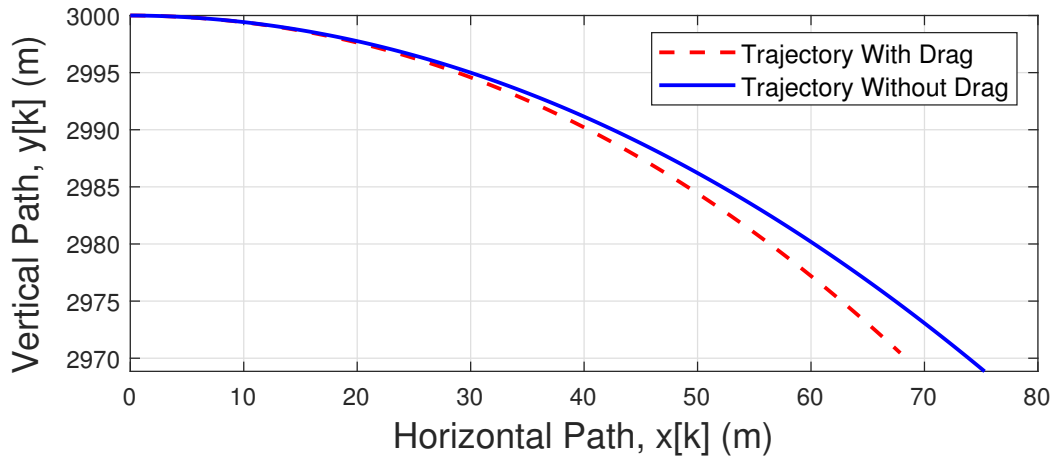

Figure 2.4. Flare trajectory with drag compared to trajectory without drag.

The ejection angle, height, and velocity can be changed between different simulation runs to configure different flare trajectories. In Fig. 2.5 the flight paths at different ejection angles are shown with drag at two different ejection heights. This is determined with a Matlab function simulation of (2.5) and (2.6).

Horizontal and vertical flare trajectories as given by (2.5) and (2.6) with an ejection angle of 0 ° and ejection height of 3000 m as a function of time are shown in Fig. 2.6. These trajectories are scaled for use as a time dependent set point on the gimbal control systems.

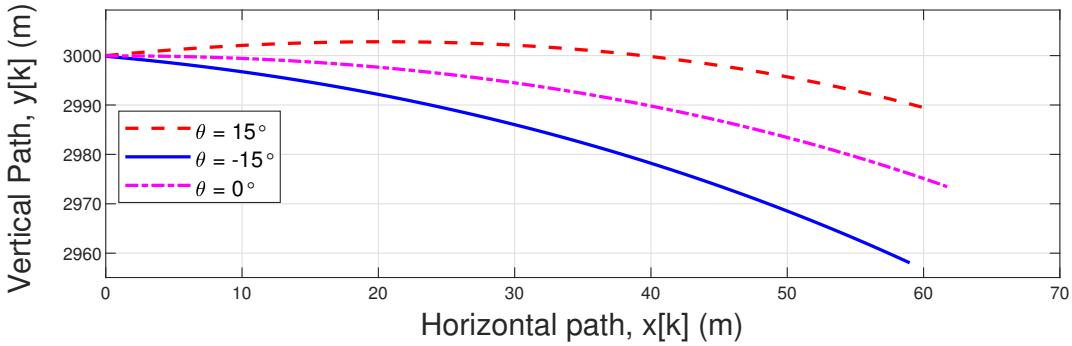

(a) Flare trajectories for different ejection angles at an initial height of 3000 m.

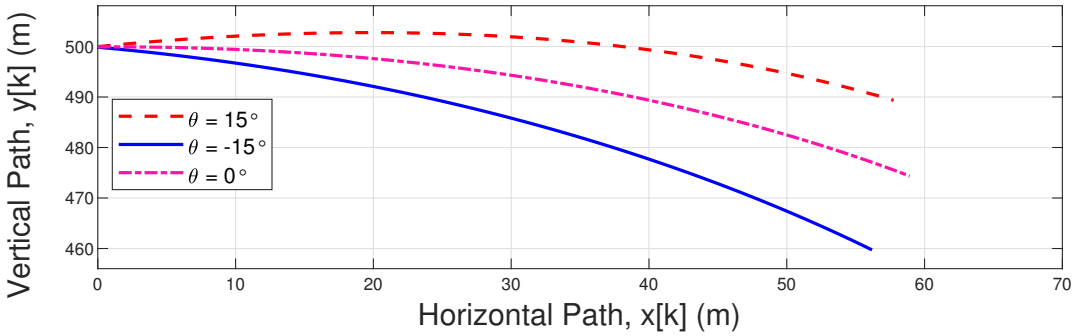

(b) Flare trajectories for different ejection angles at an initial height of 500 m.

Figure 2.5. Flare trajectories for different ejection angles and at different heights, e.g. 3000 m, (a), and 500 m, (b).

In order to implement the trajectories as set point on hardware, a polynomial function of time is required in the gimbals units. In order to arrive at the gimbal reference frame set points, a polynomial function is obtained in real world units. The polynomial equations in (2.7) are obtained from implementing Matlab $''polyval''$ and $''polyfit''$ fitting functions on Fig. 2.6, where $x_{flare}[k]$ is the horizontal flare path polynomial equation and $y_{flare}[k]$ is the vertical flare path polynomial equation. The flight paths are approximated in the least square sense. The time dependent polynomial functions are scaled into gimbal units as shown in the following section.

$$x_{flare}[k] = -2.347[k]^2 + 30.59[k] \tag{2.7a}$$

$$y_{flare}[k] = 0.504[k]^3 - 5.63[k]^2 + 0.41[k] + 3000 \tag{2.7b}$$

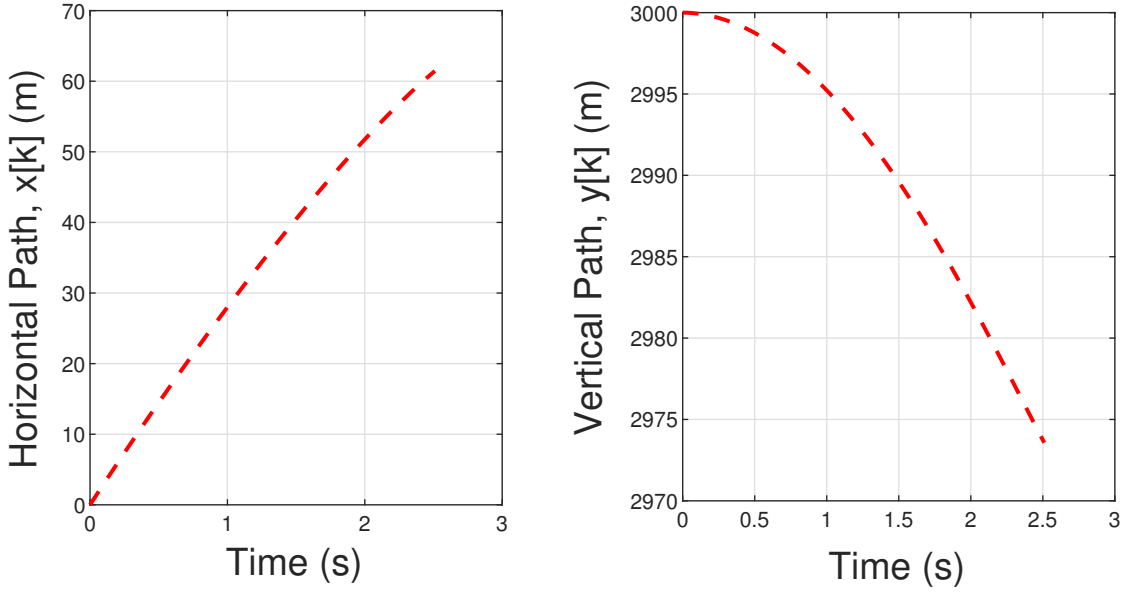

(a) Flare horizontal flight path.

(b) Flare vertical flight path.

Figure 2.6. Horizontal, (a), and vertical, (b), flare flight paths as a function of time for an ejection height of 3000 m and angle of 0 °.

The RMS error of the polynomial fit for the horizontal movement is $8.25x10^{-14}$ m and for the vertical movement is $1.26x10^{-11}$ m. The RMS error equation is given as

$$RMS\,error = \sqrt{\frac{\sum_{i=1}^{N}(y_i - \widehat{y}_i)^2}{N}}, \tag{2.8}$$

where y_i is the actual time series, $\widehat{y}_i$ is the estimated time series, i is the data point, and N is the total number of data points.

2.4.2 Flare path set point in gimbal reference frame

The flare trajectory polynomial functions as determined in the previous section are converted into hardware employable units as specified by the encoder output of radians. The range of the inner gimbal is 4.805 rad to 5.135 rad and for the outer gimbal is 1.855 rad to 2.08 rad. The horizontal flare motion travels from 0 m to 62 m and will occupy the whole inner gimbal range of 330 *m*rad. The vertical flare

motion travels from 3000 m to 2975 m and will require movement from 2.08 rad to 1.947 rad on the outer gimbal range. This implies a movement of 0.188 m in flare trajectory for every 1 *m*rad of gimbal movement, or 5.3 *m*rad gimbal rotation for 1 m of flare travel.

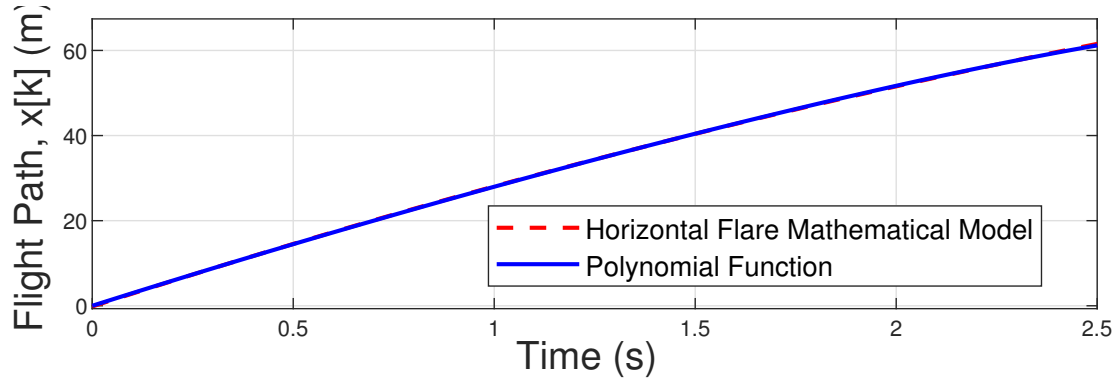

(a) Mathematical model and polynomial function presentation.

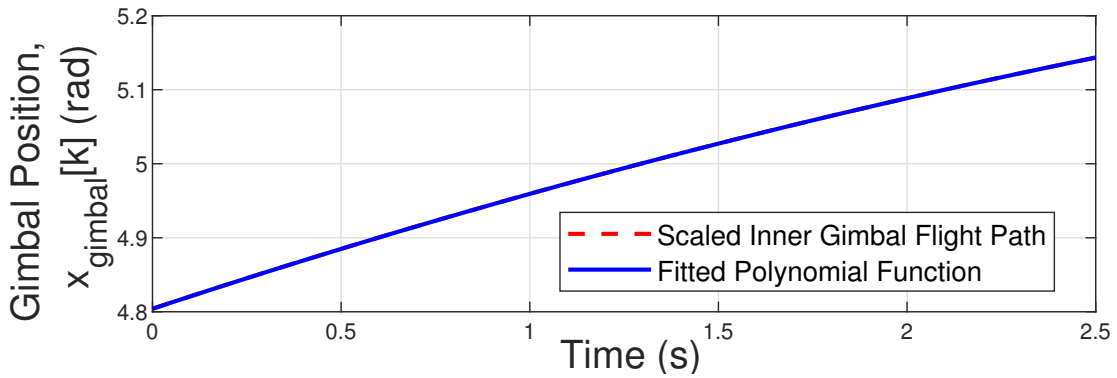

(b) Scaled horizontal flight path with fitted polynomial function.

Figure 2.7. Horizontal real world flare path, (a), scaled to the inner gimbal and its fitted function, (b).

Using (2.7) the flare trajectory in gimbal units is obtained by implementing Matlab scaling and fitting functions. The top part of Fig. 2.7 shows the horizontal flare path as determined with (2.5) and (2.6) with the polynomial function (2.7a). The bottom part shows the scaled function from (2.7a) and its fitted polynomial function as indicated here

$$x_{gimbal}[k] = -0.0139[k]^2 + 0.175[k] + 4.805, \tag{2.9}$$

where $x_{gimbal}[k]$ (*m*rad) is the horizontal flare path on the inner gimbal. The gimbal equation contains a initial position where the gimbal position measurements will start.

The process is repeated for vertical gimbal set point as Fig. 2.8 shows. The top part contains the vertical flare model path from (2.5) and (2.6), with its fitted polynomial function (2.7b). The real world flare model function (2.7b) is scaled to gimbal units and the results are shown in the bottom part of Fig. 2.8, with its function as indicated here

$$y_{gimbal}[k] = 0.002702[k]^3 - 0.03016[k]^2 + 0.00022[k] + 2.08, \tag{2.10}$$

where $y_{gimbal}[k]$ ($m$rad) is the vertical flare path on the outer gimbal.

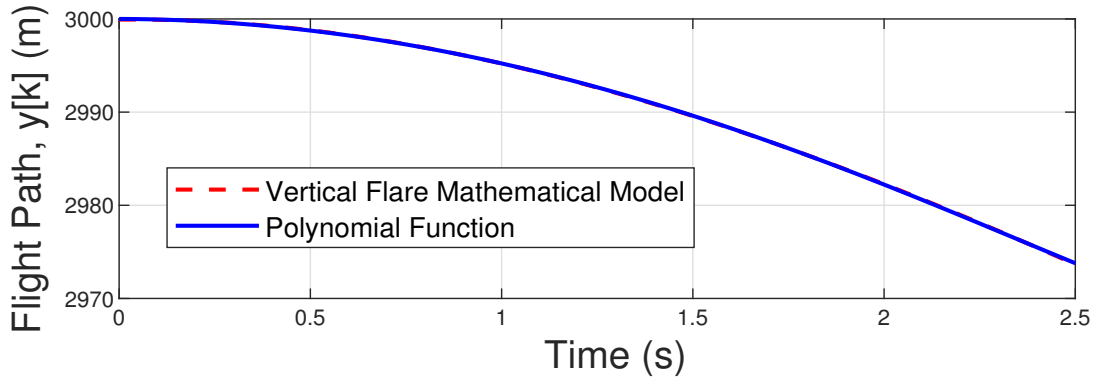

(a) Mathematical model and polynomial function presentation.

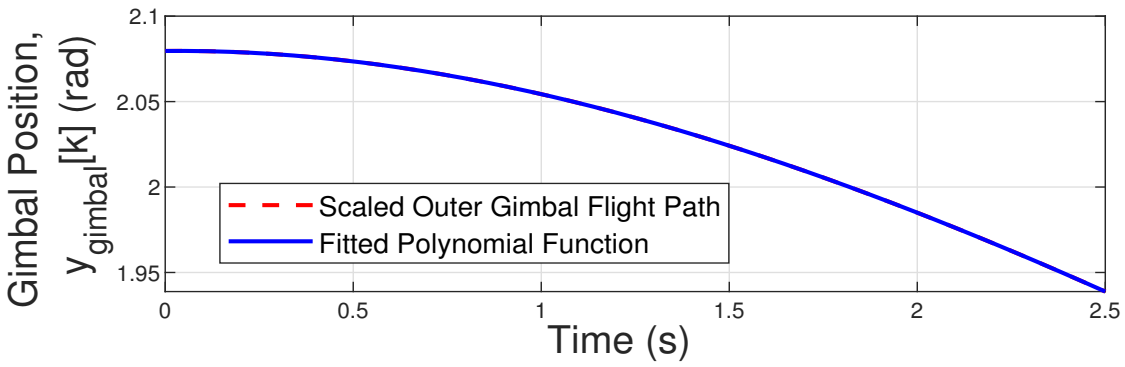

(b) Scaled vertical flight path with fitted polynomial function.

Figure 2.8. Vertical real world flare path, (a), scaled to the outer gimbal and its fitted function, (b).

In this section, the flare mathematical model theory, from Section 2.3.2, is applied in order to develop flare trajectories for the hardware. The flare trajectories are employed on the outer and inner gimbals as position set points for the respective control systems. The flares can be ejected at different altitudes and angles. For the purpose of simplification in this study, a flare ejected at 3000 m and an ejection

angle of 0 ° is utilised as flare trajectory for controller development on the gimbals. The aim is to control both gimbals as accurately as possible. It was decided that the mRMS position error below 2.00 *m*rad will provide good enough emulation. This value corresponds to an error of 0.377 m in the real world horizontal and vertical flare paths and a value of 0.6 % of the total flare flight range.

2.5 CONCLUSION

In this chapter aspects related to the target motion simulation system is discussed. This includes an overview of the HILS platform and how the gimbal system fits in. It also shows the flare models and its application in the gimbal system. In the next section, gimbal simulation models are developed. Based on the simulation gimbal models, a controller can be evaluated. The flare polynomial functions in gimbal units (2.9) and (2.10) are applied as position set points to evaluate the controllers.

CHAPTER 3 MODELLING

The purpose of the gimbal system in this study is to evaluate countermeasures in a HILS platform by acting as flare motion simulator. The control of two gimbals in the gimbal system allows emulation of a flare trajectory in two dimensions. The gimbal system therefore simulates a flare during flight, and this allows evaluation of missile seekers on the HILS platform. The flare flight paths that act as set points for the control systems are shown in Section 2.4.

In order to develop a control system for each gimbal, a simulation model is developed in this section for each gimbal. The simulation model includes aspects related to dc motor modelling and the influence of friction on the operation of the gimbals. A non-linear simulation model is developed for each gimbal that describes its operation accurately. The non-linear simulation model is then reduced to a simplified non-linear simulation model, and then further reduced to a linear simulation model. These simulation models are applied in Section 4 to develop different sets of control systems.

3.1 GIMBAL ACTUATION

Each gimbal is actuated with a dc motor. In this section the theory behind dc motor operation is described. It includes a glimpse into the non-linear friction of dc motors. A geared motor was tried out during the initial phase of the study, but better results were obtained with the gear-less motor. There were issues experienced with accurate modelling and control due to slow movement, and the presence of gears caused issues with the momentum as well as difficulty in balancing the gimbal.

3.1.1 Equations of motion for a dc motor

The equations in (3.1) govern the motion and operation for a brushed Permanent Magnet (PM) dc motor.A dc motor diagram is shown in Fig. 3.1 and is based on the work from Golnaraghi and Kuo

(2003). In the figure, the dc motor is modelled with its armature resistance R_a (Ω) and armature inductance L_a (H). The circuit further shows armature current $i_a(t)$ (A), that flows through the motor, as well as applied voltage $u_a(t)$ (V). The motor torque $T_m(t)$ (Nm) is a function of the armature current. Back electromotive force (emf) voltage $u_{emf}(t)$ (V) is a function of the rotational velocity $\omega_m(t)$ (rad/s). The load torque $T_L(t)$ (Nm) influences the motor velocity and is related to rotational inertia J_m (kgm^2). The viscous friction coefficient B_m (Nms/rad) also influences the gimbal movement. The equations are derived using Kirchhoff Voltage Law (KVL) and mechanical equations (Golnaraghi and Kuo, 2003).

$$T_m(t) = K_i i_a(t) \tag{3.1a}$$

$$u_{emf}(t) = K_b \omega_m(t) \tag{3.1b}$$

$$\frac{di_a(t)}{dt} = \frac{1}{L_a}u_a(t) - \frac{R_a}{L_a}i_a(t) - \frac{1}{L_a}u_{emf}(t) \tag{3.1c}$$

$$\frac{d\omega_m(t)}{dt} = \frac{1}{J_m}T_m(t) - \frac{1}{J_m}T_L(t) - \frac{B_m}{J_m}\omega_m(t) \tag{3.1d}$$

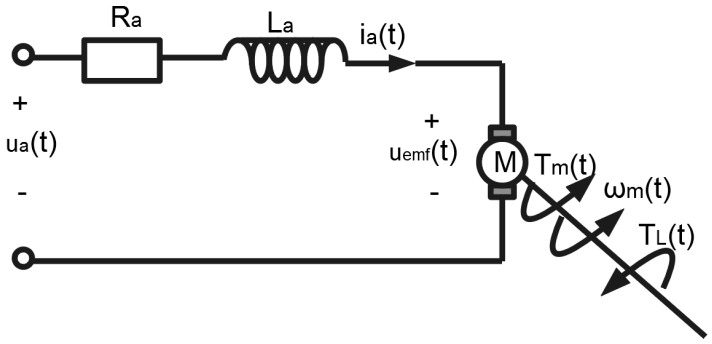

Figure 3.1. Drawing of a dc motor model.

The torque constant K_i (Nm/A) and back emf constant K_b (Vs/rad), are equal to each other and equal 25.9 mNm/A or 25.9 mVs/rad respectively. They are equal to each other in instances where SI units are used.

In order to complete the parameter estimation process to obtain a mathematical model for Simulink, (3.1) is placed in state space form as

$$\begin{bmatrix} \frac{di_a(t)}{dt} \\ \frac{d\omega_m(t)}{dt} \\ \frac{d\theta_m(t)}{dt} \end{bmatrix} = \begin{bmatrix} \frac{-R_a}{L_a} & \frac{-K_b}{L_a} & 0 \\ \frac{K_i}{J_m} & \frac{-B_m}{J_m} & 0 \\ 0 & 1 & 0 \end{bmatrix} \begin{bmatrix} i_a(t) \\ \omega_m(t) \\ \theta_m(t) \end{bmatrix} + \begin{bmatrix} \frac{1}{L_a} \\ 0 \\ 0 \end{bmatrix} \cdot u_a(t) - \begin{bmatrix} 0 \\ \frac{1}{J_m} \\ 0 \end{bmatrix} \cdot T_L(t), \tag{3.2}$$

with the output state as the measured position $\theta_m(t)$. It is related to measured rotational velocity as

$$\theta_m(s) = \frac{1}{s}\omega_m(s), \tag{3.3}$$

and the model states are

$$x(t) = [i_a(t), \omega_m(t), \theta_m(t)]^T. \tag{3.4}$$

The applied voltage $u_a(t)$ is used in the frequency domain as $E_a(s)$. During normal operation within the gimbal range, there is no disturbance on the load. The gimbal range is physically enforced in the gimbal system with limit switches. The Laplace transform of the output position $\theta_m(s)$ to applied voltage $E_a(s)$ is derived from (3.1), (3.2) and (3.3) as

$$\frac{\theta_m(s)}{E_a(s)} = \frac{K_i}{s((J_m s + B_m)(L_a s + R_a) + K_i K_b)}, \tag{3.5}$$

where $E_a(s)$ is the applied voltage $u_a(t)$ in its Laplace form.

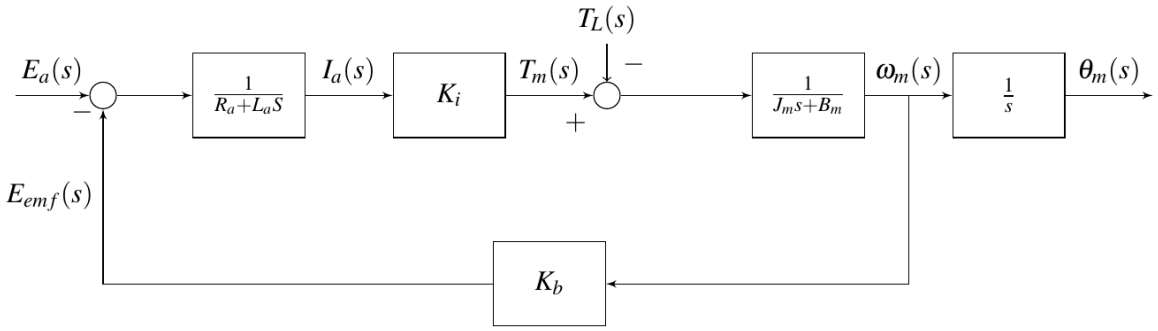

Figure 3.2. A block diagram of a brushed PM dc motor model.

A block diagram of the brushed PM dc motor model representation is given in Fig. 3.2 (Golnaraghi and Kuo, 2003). In this block diagram $E_{emf}(s)$ is the frequency domain version of $u_{emf}(t)$. This block diagram is used to model each gimbal in Simulink.

This section discussed the equations and variables involved in describing and modelling the operation of a dc motor. The equations and block diagram described are implemented in the simulation model for each gimbal in Simulink and shown in the following section.

The inner and outer gimbals are decoupled and do not influence each other. Each gimbal functions independently from the other.

3.2 GIMBAL MODELS

The simulation model for each gimbal is developed in Simulink. It is developed using (3.1) to (3.5) and Fig. 3.2. The values of the variables, such as J_m, B_m, R_a, and L_a, are needed to portray gimbal movement in the simulation model. The non-linear effects present in the systems are incorporated into the non-linear simulation model. They are incorporated as a load torque $T_L(t)$ function. Friction contributes to the non-linear behaviour of the gimbals, and different friction types are therefore investigated next.

3.2.1 Friction

This section discusses friction properties attributed to the dc motors utilized for actuating gimbal movement. The parameters are determined for the purpose of including it in the simulation model. The movements of the gimbals are very slow, as dictated by the flare trajectory, which implies that the non-linear properties of friction play a significant role.

Friction is described as a complex phenomenon (Olsson, Astrom, de Wit, Gefvert and Lischinsky, 1998; Virgala, Frankovsky and Kenderova, 2013; Pennestri, Rossi, Salvini and Valentini, 2016). It is present where contact occurs between two surfaces and exists in all mechanical systems. Friction is a key element in accurate and reliable dynamic system simulations. Friction introduces non-linear effects in the system. In mechanical systems, it can influence the modelling and identification stage during the practical control design process.

It is favourable to use dc motors as actuators in speed and position control applications as it is relatively easy to control and can be applied in a wide field of applications. To model a dc motor that has a load connected to its shaft, the first step is normally to neglect non-linear parameters such as friction. A linear transfer function can then be determined with the mathematical model of a dc motor as described in (3.5). If it is known how to describe the friction of the motor, the rotational velocity or speed and position can be controlled with relative ease (Virgala *et al.*, 2013). In this case, the non-linear parameters due to friction should be included in the system analysis.

Friction modelling is important in control systems as it can result in steady-state errors and poor performance according to Olsson *et al.* (1998). Understanding problems associated with friction and its effects are important in order to improve reliability, economy and safety of a system. It is important to reduce friction as much as possible early in the design stage with a proper hardware design. It is important for the benefit of the control engineer to understand the influence of friction in a system and to deal effectively with friction, by reducing it or compensating for it (Virgala *et al.*, 2013).

There are four different types of friction: break-away force or stiction, Coulomb, Stribeck, and viscous friction.

- Stiction is the retarding force which prevents movement in the system where two surfaces seem stuck. Break-away force F_s is the force required to overcome stiction, also known as static friction, and initiate movement (Olsson *et al.*, 1998; Virgala *et al.*, 2013). Virgala *et al.* (2013) shows how to determine break-away force experimentally and describes it with (3.6), where the resultant torque is $T(t)$.

$$T(t) = \pm(F_s)|_{\theta'=0} \tag{3.6}$$

- Virgala *et al.* (2013) states that Coulomb friction F_c is independent of velocity. It is always present and is directly opposite to the direction of velocity. Coulomb friction is normally smaller than break-away force. It is also known as kinetic friction and has a constant amplitude as described here.

$$T(t) = F_c \cdot \frac{\frac{d\theta(t)}{dt}}{|\frac{d\theta(t)}{dt}|} \tag{3.7}$$

- The Stribeck effect is a non-linear force and is seen where the friction force decreases at low velocities. It is observed at the beginning of movements, just after stiction is overcome. The Stribeck effect varies with material properties, temperature, etc. Olsson *et al.* (1998) observes that a Stribeck curve shows how the force is a function of velocity for a motion with constant velocity. A friction-velocity curve can be established for a dc motor. It is recommended

to establish a friction-velocity curve as part of the dc motor model which can be utilized in simulations.

- According to Virgala *et al.* (2013), the viscous friction depends on velocity as it increases with an increase in velocity. It is a retarding force that relates the applied force to velocity as shown here.

$$T(t) = B \cdot \frac{d\theta(t)}{dt} \tag{3.8}$$

Coulomb and Stribeck friction models introduce non-linear parameters in the model which produces more precise results when compared to instances where only viscous friction is applied. Olsson *et al.* (1998) explains that frictional lag has hysteresis as velocity varies. The size of the hysteresis loop increases with normal load, viscosity, and frequency of the velocity variation. These experiments indicate the necessity of using dynamic friction models.

Models by Olsson *et al.* (1998) showcase classical static models which include stiction, Coulomb friction, and viscous friction. Dynamic models are needed to satisfy precision requirements as allowed by advances in hardware. According to Virgala *et al.* (2013) building an accurate model is a crucial requirement for the reliable design of a control system. It can be hard to obtain a model when the plant has uncertainties or time dependencies, which means its parameters cannot be determined. In this instance, system identification techniques can be used to determine system parameters. Friction identification can be executed when all the dc motor variables are known.

Olsson *et al.* (1998) states that the behaviour of small displacements is of particular importance where precise position control is required. At these small displacements, the dc motor operates in a region where friction force changes rapidly. Olsson *et al.* (1998) describes an experiment that reveals much about the behaviour at small displacements.

It is important to note that due to the small operating range of the gimbal, the gimbals will probably be actuated with small displacements. This may influence the accuracy of its operation.

3.2.2 Gimbal simulation model

In order to accurately simulate the gimbals, the input voltage $u_i(t)$ (V) is applied to a low pass filter function and dead zone function. The output of these functions are the applied voltage $u_a(t)$ that is applied to the dc motor model. The input voltage $u_i(t)$ is used in the frequency domain as $E_i(t)$.

Each gimbal is characterised with input voltage step tests. The outputs of the input voltage step tests are obtained through measurements on the gimbals or simulations in the form of the measured position, rate, or current. The measured position $\theta_m(t)$ (rad) is obtained from the output of the encoder on each gimbal and indicates the position of the gimbal. The rotational velocity $\omega_m(t)$ is determined with the use of an α-β filter that is implemented on the software. Finally, current measurement $i_a(t)$ is obtained from current sensors on the motor drivers. Through several iterations and experimentation, the parameters of the simulation model are determined by comparing measured data sets to simulation output data sets. The simulation results are compared with a different set of measurements than the measurements used to establish the models.

A comparative measurement of all the simulated and measured position data sets $\theta_m(t)$ at the different input voltages $u_i(t)$ are computed in Matlab with a goodness of fit fitness test. The function determines how well the simulated model matches measured or reference data sets. The goodness of fit test cost function is a normalised RMS error function. The fitness is established by determining the fit in percentage (%). This gives an indication of how close the simulated data is to the measured data. The normalised RMS error function with the percentage calculation is shown here

$$\text{Fit} = \left(1 - \sqrt{\frac{\sum_{i=1}^{N} |(x_{ref,i} - x_i)|^2}{\sum_{i=1}^{N} |(x_{ref,i} - \bar{x}_{ref})|^2}}\right) \times 100, \tag{3.9}$$

where Fit (%) indicates the normalised RMS fit, x_{ref} is the measurement, x is the simulated value, and i is the test pair.

In order to obtain the values of R_a and L_a, the data sheet of the motor is consulted. Both gimbals have the same dc motor. On the data sheet, resistance R_a equals 0.611 Ω and the inductance L_a equals 0.119 mH. The values are slightly adjusted in order to obtain a good fit of measured data onto simulated data.

Rotational inertia J_m is the inertia due to mechanics and can be obtained from parameter estimation and experimentation. The viscous friction coefficient B_m and other possible friction parameters are obtained with parameter estimation. Parameter estimation can be considered as the process of adjusting values in a mathematical model so that the results of the mathematical model deliver the same response as the actual system.

To determine the break-away force on each gimbal, the procedure outlined by Virgala *et al.* (2013) is used. The input voltage on each dc motor is slowly increased, by increasing the duty cycle with one count, until gimbal rotation starts. The break-away force is then calculated using the current measured just before break-away happens. This characteristic is included in the simulation model as a dead zone function.

Both gimbals exhibit non-linear behaviour, which can be attributed in a certain extent to friction. It was initially thought that Stribeck and Coulomb friction may be excluded from the model and that only the viscous friction parameter should be determined. However, as the gimbals rotate slowly to emulate flare trajectory, the dc motor operates in the non-linear Stribeck friction range at times, due to low input voltage values. Stribeck and Coulomb friction are very difficult to measure because of their non-linearity and the small range of motion of the gimbals.

To simulate non-linear behaviour, total load torque $T_L(t)$ (Nm) as used in (3.1) and (3.2) is the sum of load torque because of the limit switch functionality $T_{LS}(t)$ (3.11) and load torque because of non-linear effects $T_{LG}(t)$ as shown here.

$$T_L(t) = T_{LS}(t) + T_{LG}(t) \tag{3.10}$$

Limits on the inner and outer gimbal positions are implemented in the physical system by limit switches. The limit switches are mechanical stops. They are triggered when the gimbals run into them. The switches trigger the processor to stop all gimbal activities, by electrically stopping the drives.

The load torque as a result of the limit switches is defined in simulation for both gimbals as

$$T_{LS}(t) = \begin{cases} K_{LL}(\theta_{LL} - \theta_m(t)) & \theta_m(t) < \theta_{LL}(t), \\ K_{UL}(\theta_{UL} - \theta_m(t)) & \theta_m(t) > \theta_{UL}(t), \\ 0 & \theta_{LL}(t) \leq \theta_m(t) \leq \theta_{UL}(t), \end{cases} \tag{3.11}$$

where $\theta_m(t)$ is the measured position, $\theta_{LL}(t)$ (rad) is the lower limit, $\theta_{UL}(t)$ (rad) is the upper limit, K_{LL} (Nm/rad) is the gain employed when the gimbal passes the lower limit and K_{UL} (Nm/rad) is the gain used when the gimbal passes the upper limit.

The limit switches are imposed in simulation by artificially increasing the load torque $T_{LS}(t)$ (Nm) due to the limit switches once the gimbal exceeds its possible range. Once a gimbal exceeds the lower position limit, the limit switch load torque is increased in relation to the difference between the measured position $\theta_m(t)$ (rad) and the lower limit as shown in (3.11). Once the gimbal passes the upper position limit, the load torque is increased in relation to the difference between the measured position and the upper limit as shown in (3.11).

The Simulink model implementation of (3.11) is shown in Fig. 3.3. In this picture there are switches, summing functions, and amplifiers that determine when the position exceeds the physical constraints and causes the load torque to increase for gimbal movement to stop, copying the functionality of the physical limit switches. This functionality is part of the bigger simulation model for both the inner and outer gimbals.

The load torque as a result of non-linear effects $T_{LG}(t)$ is a function of the applied voltage $u_a(t)$ and the rotational velocity $\omega_m(t)$. It is defined separately in the next sections for the inner and outer gimbals.

The Laplace equation in (3.5) is rewritten to include the effect of load torque.

$$\theta_m(s) = \frac{K_i E_a(s) - (R_a + L_a s) T_L(s)}{s(K_i K_b + (J_m s + B_m)(R_a + L_a s))} \tag{3.12}$$

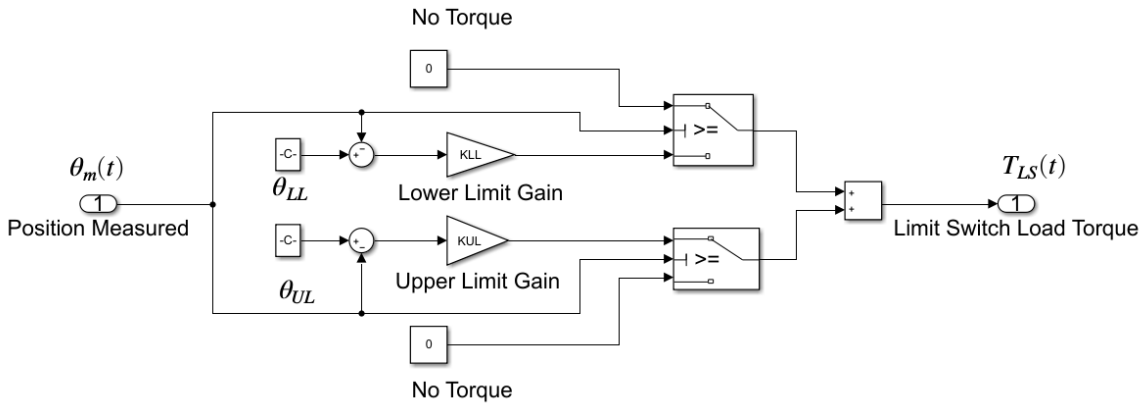

Figure 3.3. Physical position limits imposed as a load torque force.

The parameters related to characterising each gimbal is determined in the following sections respectively for the inner gimbal and the outer gimbal. The non-linear behaviour is represented most accurately with the non-linear simulation model. The complete non-linear simulation model contains all the state variables and constants as described in Section 3.1, with non-linear load torque functions and a limit switch implementation function. The simulation models are then simplified and linearised in order to develop controllers. The simplified non-linear simulation model contains a transfer function and a gain function that represent the gimbal dc motor simulation model. The linear simulation model contains only linear functions. All simulation models are established by comparing and fitting the simulation model current $i_a(t)$, rate $\omega_m(t)$, or position $\theta_m(t)$ output data sets with measurement data sets obtained from the actual gimbals. Each gimbal is designed to function independently from any other objects. During each test, the applied voltage $u_a(t)$ is adjusted, the parameters in the model are then adjusted until the output data sets of the simulation follows the response of the measured data sets.

3.3 INNER GIMBAL SIMULATION MODEL

The inner gimbal is smaller than the outer gimbal and rotates inside the outer gimbal. There are no wires attached that can influence its movement. The aim is to obtain the parameter values for the parametrised inner gimbal non-linear model as represented by (3.12). The dc motor model parameters are determined using a small range of input voltage step values. Once input voltage step sizes become too large, the gimbal moves too quickly into a limit switch. This makes data measurement difficult. The motor constants K_i and K_b, which are equal in value, are represented as K_f in this section.

In this section an inner gimbal non-linear simulation model is developed using the parameter estimation

process. A simplified non-linear model is derived from the non-linear model and a linear model is derived from the simplified non-linear model.

3.3.1 Inner gimbal non-linear simulation model

The motor resistance R_a is determined as 1.2 Ω, by adjusting the resistance value obtained from the data sheet, until the model simulation current $i_a(t)$ matches the actual measured current. The comparison between simulated response and measured response are evaluated with a goodness of fit test (3.9) as 67.8 %. The motor inductance value stays at 0.119 mH.

The motor rotational inertia J_m and friction B_m are determined iteratively by adjusting their values based on the gimbal rotation rate. For these two variables, the measured rotation rate was fitted onto the model output rate, until the response curves matched. The match was evaluated with a goodness of fit test (3.9) as 89.75 %. The results are shown below. The friction B_m is set at 0.003 Nms/rad, while inertia J_m is set at 0.004375 kgm^2.

With the implementation of a 20 Hz low pass filter (3.13) the simulation results show a response time similar to how the inner gimbal reacts from input voltage $E_i(s)$, where

$$E_f(s) = \frac{1}{1/(2\pi 20)s+1} E_i(s), \tag{3.13}$$

is the resultant signal from the input filter which is denoted as $E_f(s)$ (V), where $E_f(s) = \mathcal{L}(u_f(t))$. It is applied to the dead zone function $D_i(u_f(t))$. This represents the delay in the response present in the system. The inner gimbal break-away force was determined to be overcome from voltages below -0.22 V and above 0.22 V. This is simulated with a dead zone function.

$$D_i(u_f(t)) = \begin{cases} 0 & |u_f(t)| \leq 0.22\ V, \\ 1 & |u_f(t)| > 0.22\ V. \end{cases} \tag{3.14}$$

The output signal from the dead zone is denoted by applied voltage $u_a(t)$, where $E_a(s) = \mathcal{L}(u_a(t))$ and is fed into the dc motor simulation model (3.12).

$$u_a(t) = D_i(u_f(t))u_f(t) \tag{3.15}$$

The inner gimbal non-linear torque function addresses the changes in the motion or the rate of the gimbal at different applied voltage values, i.e., it addresses the change in gimbal behaviour when it starts and stops rotating. This is not addressed with the linear model. The inner gimbal load torque $T_{LG}(t)$ is defined as

$$T_{LG}(t) = t_0(u_a)\omega_m(t)^2 + t_1(u_a)u_a(t), \tag{3.16}$$

where $t_0(u_a)$ (Nms^2/rad^2) and $t_1(u_a)$ (Nm/V) are functions of the applied voltage. Function t_0 is defined as

$$t_0(u_a) = \begin{cases} 0.0005 & u_a > 0\ V, \\ -0.0007 & u_a < 0\ V, \\ w(\omega_m) & u_a = 0\ V, \end{cases} \tag{3.17}$$

where

$$w(\omega_m) = \begin{cases} 0.0025 & \omega_m < -1\ rad/s, \\ 0.01 & -1\ rad/s \leq \omega_m < -0.5\ rad/s, \\ 1.00 & -0.5\ rad/s \leq \omega_m < 0\ rad/s, \\ -0.1 & 0\ rad/s \leq \omega_m < 0.2\ rad/s, \\ -0.06 & 0.2\ rad/s \leq \omega_m < 0.75\ rad/s, \\ -0.01 & 0.75\ rad/s \leq \omega_m < 1\ rad/s, \\ -0.0025 & \omega_m \geq 1\ rad/s. \end{cases} \tag{3.18}$$

These values were obtained heuristically. The influence of t_0 when the applied voltage is 0 V is to simulate the stopping movement of the gimbal when the voltage is removed while the gimbal is still moving. This is influenced by the rate and direction of the gimbal when the applied voltage is reduced to 0 V. This gives the position of the gimbal when it has come to a standstill. The result from a goodness of fit test according to (3.9) is 94.17 %.

The function $t_1(u_a)$ is derived through measuring $\frac{d\omega_m(t)}{dt}$ in the simulation model and changing it to fit the actual gimbal rate with different applied voltage steps $u_a(t)$. The derived t_1 values at each positive

and negative voltage step are shown in Figs. 3.4 and 3.5. The t_1 value depends on the applied voltage $E_a(s)$, or in the time domain $u_a(t)$, and shows different characteristics for positive and negative applied voltage steps. Therefore, the same polynomial equation cannot be implemented for both positive and negative voltage ranges.

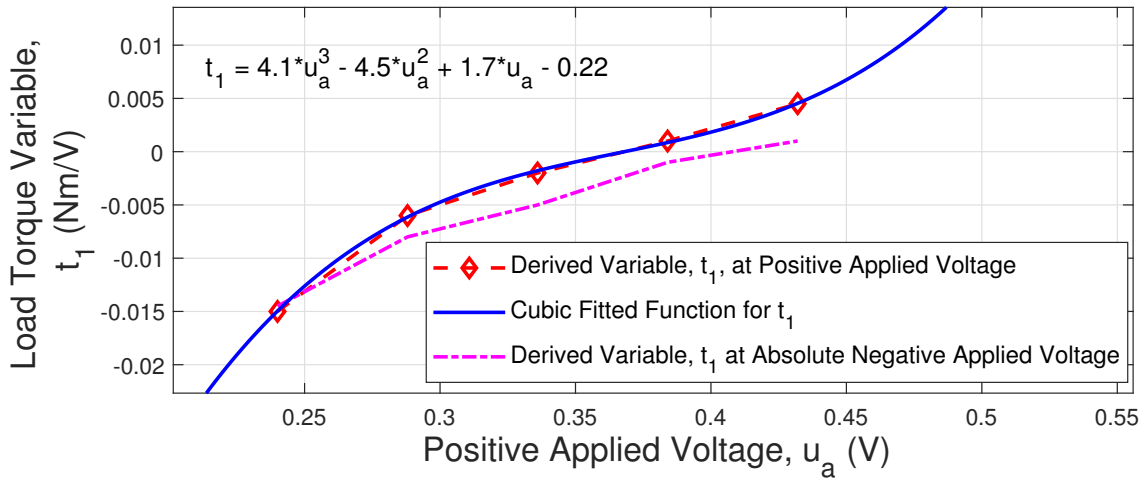

Figure 3.4. Inner gimbal non-linear model torque function variable with fitted functions for positive applied voltages.

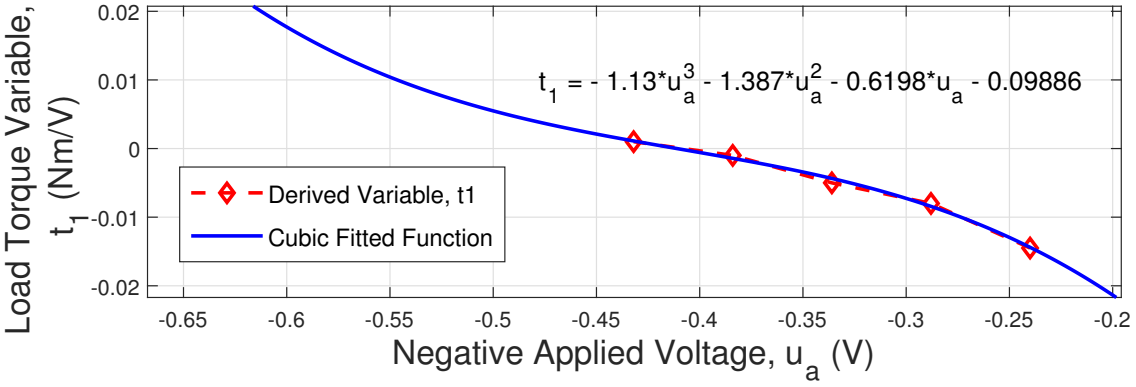

Figure 3.5. Inner gimbal non-linear model torque function variable with fitted functions for negative applied voltages.

The t_1 polynomial equation fitted to the data in Fig. 3.4 for positive applied voltages and negative applied voltages from Fig. 3.5 is

$$t_1(u_a) = \begin{cases} 4.1u_a^3 - 4.5u_a^2 + 1.7u_a - 0.22 & u_a > 0\,V, \\ -1.13u_a^3 - 1.387u_a^2 - 0.6198u_a - 0.9886 & u_a < 0\,V, \\ 0 & u_a = 0\,V. \end{cases} \tag{3.19}$$

The polynomial function is obtained using Matlab basic fitting tools and the $"polyfit"$ function. This function determines the best fit for the polynomial degree in a least-squares sense and the fit results in a RMS error of 0.00029 Nm/V for the positive voltage steps and 0.00089 Nm/V for the negative applied voltage steps. The RMS error is determined using (2.8).

Finally, the inner gimbal non-linear simulation model is given in Fig. 3.6. In the simulation model $T_{LS}(t)$ is given by (3.11), the applied voltage $u_a(t)$ by (3.15), and $T_{LG}(t)$ by (3.16).

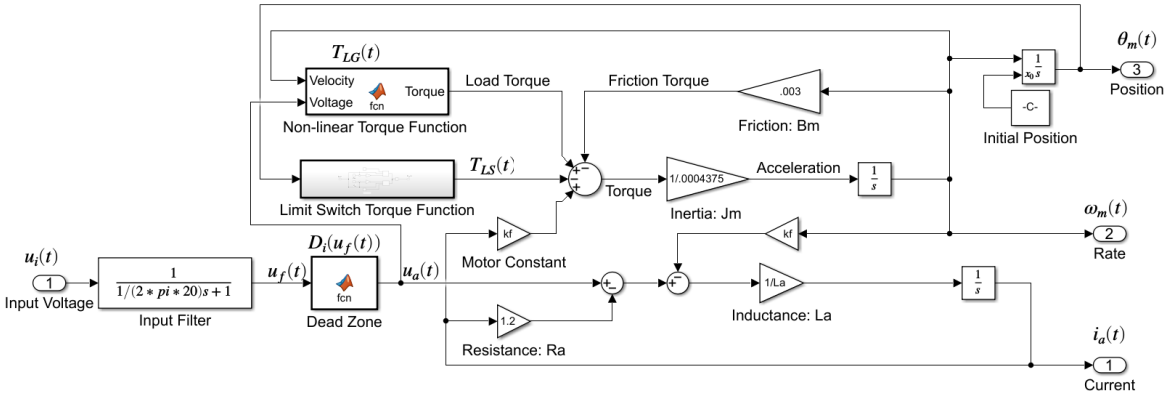

Figure 3.6. The inner gimbal non-linear simulation model.

The results from simulating the non-linear model in Fig. 3.6 are shown with a response to a step input voltage in Fig. 3.7. It is clear that the model follows the measured data set from the gimbal accurately. The step input voltage of 0.432 V is also shown in the graph in order to show how the gimbal stops when input voltage is removed.

Fig. 3.8 shows the goodness of fit as given in (3.9) for the gimbal position $\theta_m(t)$ at each input voltage. The average goodness of fit is 94.17 %.

In the following section this non-linear model is reduced to the simplified non-linear model with the introduction of a gain function to represent the non-linear characteristics.

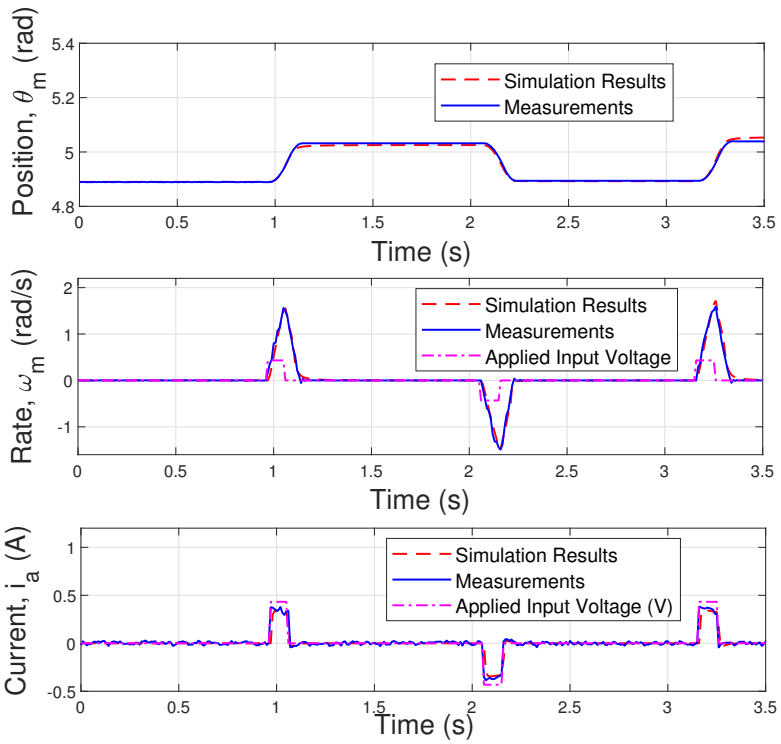

Figure 3.7. Inner gimbal non-linear model results with input voltage steps of ± -0.432 V, plotted with the corresponding gimbal measured data sets.

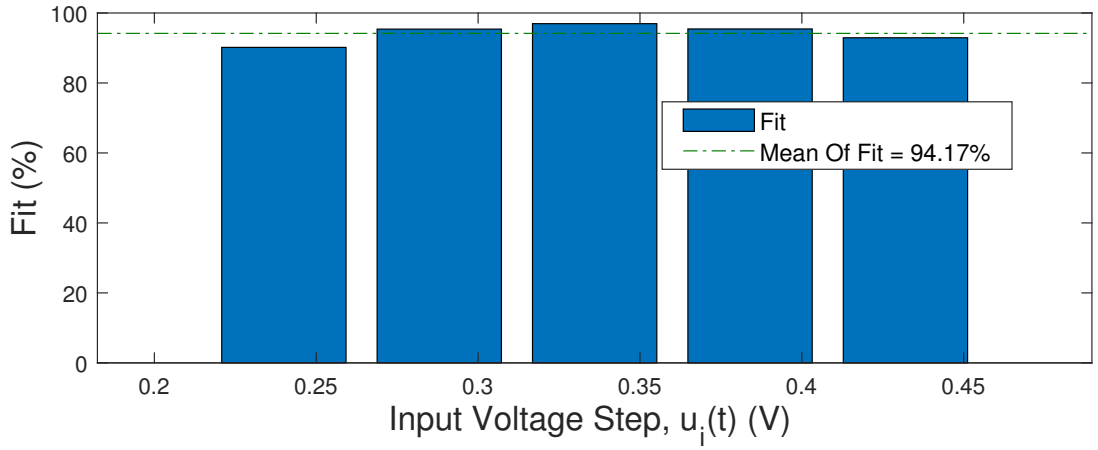

Figure 3.8. Comparison of inner gimbal non-linear model position output and gimbal measured position data sets.

3.3.2 Inner gimbal simplified non-linear simulation model

The aim of the simplified non-linear model is to simplify Fig. 3.6. It is developed by tuning gain values at the different applied voltage steps as well as filter values, in order to obtain a good fit of the simulation rate and position onto the inner gimbal measured rate and position.

The system reacts differently at different applied voltage steps. These reactions are incorporated into a gain function $v(u_a)$ (V/V), with two polynomial functions, one for positive applied voltages and one for negative applied voltages. These functions can compensate for non-linear movement of the inner gimbal. The gain values are plotted in Fig. 3.9 and the polynomial function derived from the data points are shown in (3.20). The polynomial functions are functions obtained with Matlab basic fitting tool and uses the $''polyfit''$ function. The RMS error between the polynomial equation results and measured values is 0.01793 V/V for the negative applied voltage polynomial function. The RMS error for the polynomial function of the positive applied voltage is 0.09562 V/V. The RMS error is determined using (2.8).

$$v(u_a) = \begin{cases} 941.9u_a^3 - 1078u_a^2 + 409u_a - 47.54 & u_a \geq 0\ V, \\ -226.1u_a^3 - 331.7u_a^2 - 153.6u_a - 19.28 & u_a < 0\ V. \end{cases} \tag{3.20}$$

Through tuning, a low pass filter (3.21) is added in order to assist with emulating non-linear model behaviour in a simplified form. The applied voltage $u_a(t)$ is amplified with the gain $v(u_a(t))$ as shown with (3.22) and passed through the low pass filter (3.21). The input to the low pass filter is $\Gamma(s) = \mathcal{L}(\gamma(t))$. The input function (3.15) remains unchanged in the simplified non-linear model.

$$\frac{\theta_m(s)}{\Gamma(s)} = \frac{1}{s}\left(\frac{1}{1/(2\pi 4.5)s+1}\right) \tag{3.21}$$

$$\gamma(t) = v(u_a(t))u_a(t) \tag{3.22}$$

The input voltage function (3.15), gain function (3.20) is implemented on the simplified non-linear model, with the low pass filter (3.21), as well as the amplification function (3.22) as shown in Fig. 3.10. The inner gimbal simplified non-linear simulation model in Fig. 3.10 does not emulate actual gimbal behaviour as accurately as the non-linear model, but does show a similar response as can be seen in Fig. 3.11.

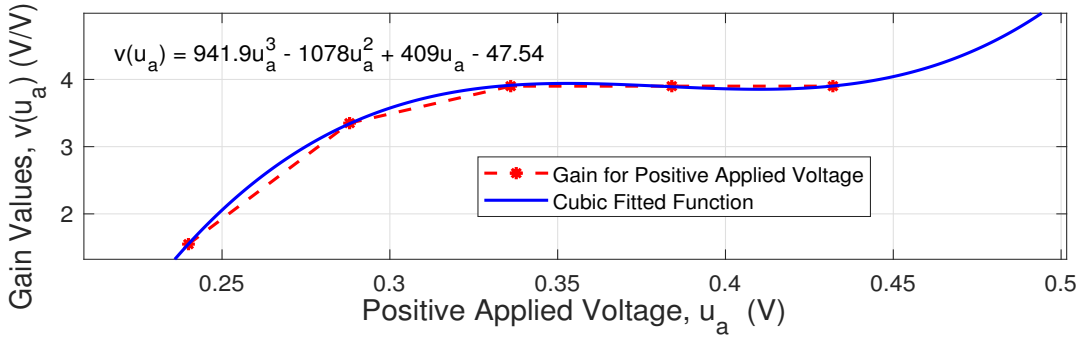

(a) Inner gimbal simplified non-linear model gain values for positive applied voltages.

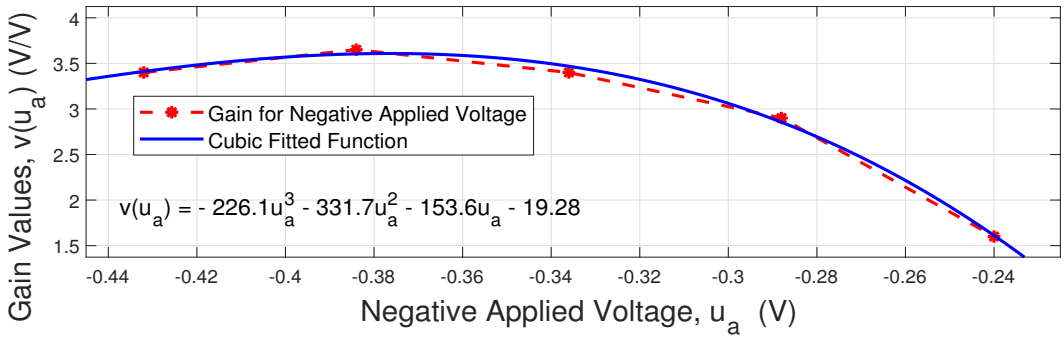

(b) Inner gimbal simplified non-linear model gain values for negative applied voltages.

Figure 3.9. Inner gimbal simplified non-linear model gain and its fitted gain function for positive applied voltages,(a), and negative applied voltages, (b).

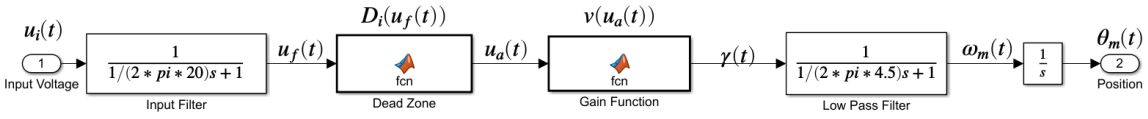

Figure 3.10. Inner gimbal simplified non-linear simulation model.

Fig. 3.11 graphs show the simulated position and rate data set with gimbal measured position and rate data for an input voltage step of 0.336 V. To illustrate the gimbal movement when power is removed, the input voltage step is added to the rate graph.

A goodness of fit (3.9) between the simulation position results and inner gimbal position measurements are shown in Fig. 3.12. The average fit of the simulation data is 91.86%, which is less than the non-linear model. In the following section a linear model is evaluated that is derived from this simplified non-linear model.

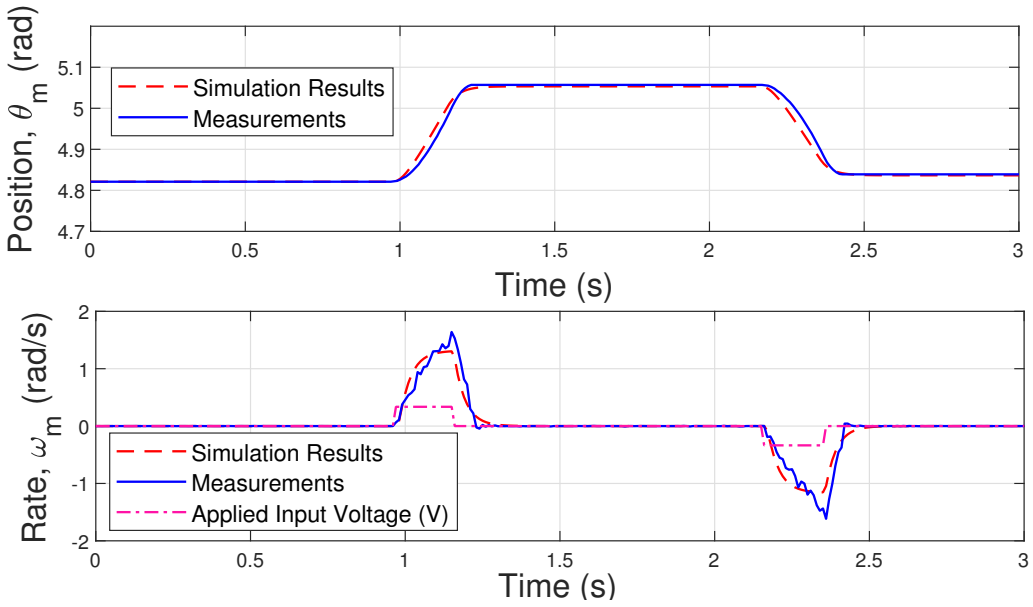

Figure 3.11. Inner gimbal simplified non-linear model results with input voltage steps of $\pm$ 0.336 V.

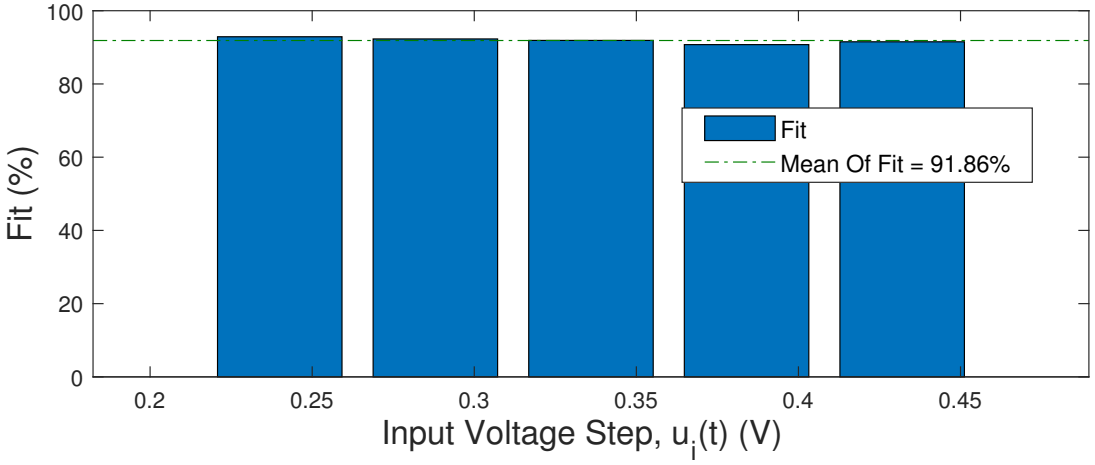

Figure 3.12. Inner gimbal simplified non-linear model position comparison with measured data sets.

3.3.3 Inner gimbal linear simulation model

The simplified non-linear simulation model was developed in order to arrive at this linear model. Further reduction of the simplified non-linear model uses the average of the data points used to determine (3.20) which is 3.4 V/V with the same low pass filter and input filter from the simplified non-linear simulation model Fig. 3.10. The dead zone function is removed.

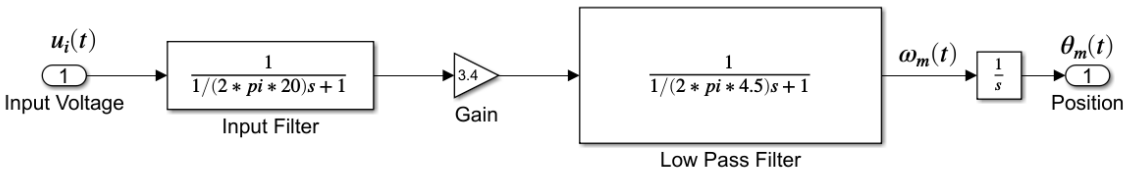

Figure 3.13. Inner gimbal approximated linear simulation model.

The linear simulation model is described by (3.23) and presented in Fig. 3.13. This linear model is used to analyse the response of the system and to develop the first controller.

$$\theta_m(s) = \frac{3.4}{s}\left(\frac{1}{1/(2\pi 4.5)s+1}\right)\left(\frac{1}{1/(2\pi 20)s+1}\right)E_i(s) \tag{3.23}$$

The simulation position and rate results from the linear model is shown in Fig. 3.14. It is compared with the measured position and rate data. The goodness of fit test (3.9) indicate that the linear model accuracy is less than the other models as presented in Fig. 3.15. The worst performance is at the lowest input voltage step of 0.24 V. The Matlab goodness of fit cost function used to determine the how well the simulated model matches the measured data determines a normalised RMS error value of 1.8363. The Matlab "compare" function determines the fit in % as shown in (3.9). With the equation as in (3.9) this results in a fit of -83.63 %. This indicates a very poor fit of measurement data and simulation data.

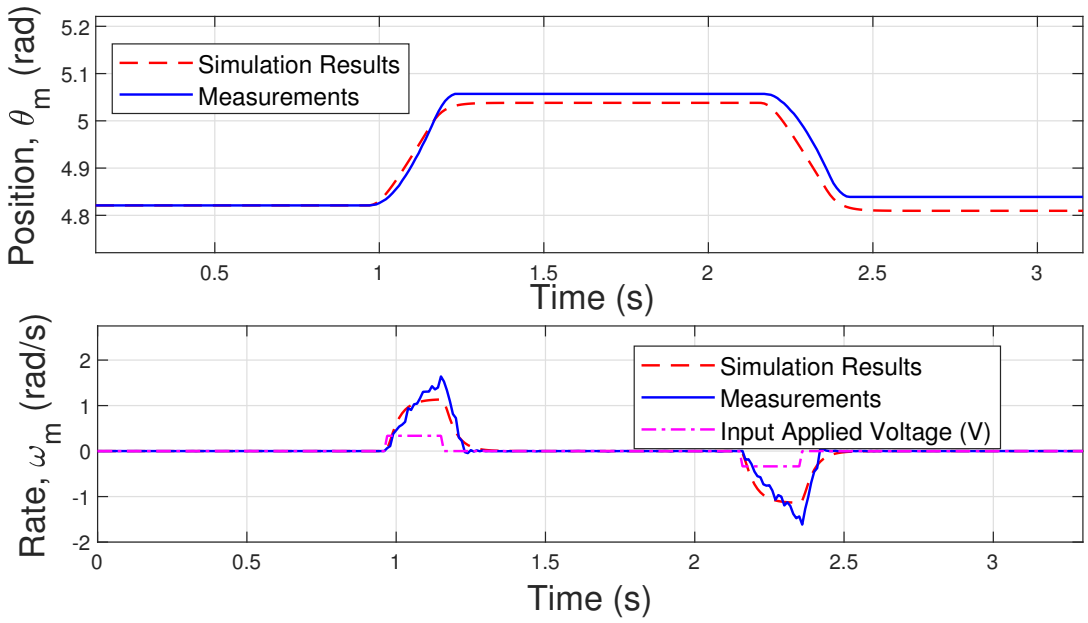

Figure 3.14. Inner gimbal linear model results with input voltage steps of $\pm$ 0.336 V.

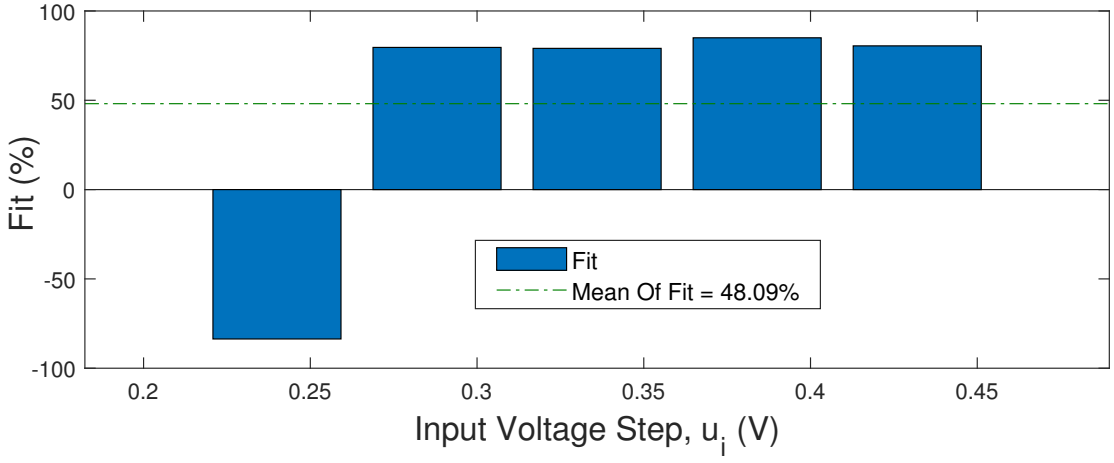

Figure 3.15. Inner gimbal linear model position fit with the measured inner gimbal data sets.

3.4 OUTER GIMBAL SIMULATION MODEL

The inner gimbal encoder and motor wires hang from the outer gimbal. The wires influence the outer gimbal acceleration and deceleration. Even though the outer gimbal is balanced, the wires still exert a non-linear force. The challenge to develop a model for the outer gimbal is to determine the effect of electrical wires hanging from it.

As with the inner gimbal, there are three simulation models, the first one contains non-linear effects closest to the real life situation. The second model is a simplified non-linear model and the third is a linear model. The linear model is analysed with the purpose of developing a controller.

3.4.1 Outer gimbal non-linear simulation model

This section shows development of the non-linear simulation model. The parameters are estimated using the dc motor equation (3.12) and block diagram Fig. 3.2. Several step tests are performed iteratively at different input voltages. As with the inner gimbal, operating test scenarios are limited to input voltages that are low enough to allow slower movements for proper data measurement. If the voltage is too high, the gimbal slams quickly into the limit switches and no reliable data measurements can happen.

The motor resistance R_a is determined as 1.0504 Ω. It is determined similar to how the resistance for the inner gimbal was determined. The motor inductance L_a stays the same as the data sheet value of 0.119 mH. The goodness of fit test result according to (3.9) is 93.57 %.

The motor rotational inertia and friction are determined similar to how these values are determined with the inner gimbal. The friction B_m is set at 0.025 Nms/rad, and the inertia J_m is set at 0.021 kgm^2. For these values the goodness of fit according to (3.9) is 89.75 %.

The outer gimbal non-linear simulation model contains an input filter which creates a delayed response time similar to the real system response

$$E_f(s) = \frac{1}{1/(2\pi 10)s+1} E_i(s). \tag{3.24}$$

The filtered signal is applied to the outer gimbal dead zone function $D_o(u_f(t))$ (V) as

$$D_o(u_f(t)) = \begin{cases} 0 & |u_f(t)| \leq 0.14\ V, \\ 1 & |u_f(t)| > 0.14\ V, \end{cases} \tag{3.25}$$

where the dead zone represents an area in which the gimbal does not move when the absolute filtered voltage $u_f(t)$ is below a certain value. The output signal from the dead zone function is fed into the dc motor simulation model as $u_a(t)$.

$$u_a(t) = D_o(u_f(t))u_f(t) \tag{3.26}$$

Similar to the inner gimbal, the outer gimbal load torque $T_{LG}(t)$ models the non-linear nature of the outer gimbal movement and responds differently to positive and negative input voltage step values. Therefore, the outer gimbal load torque $T_{LG}(t)$ is defined as

$$T_{LG}(t) = \begin{cases} t_5 & \omega_m(t) < 0\ rad/s,\ u_a(t) \neq 0\ V, \\ t_6\omega_m(t) & \omega_m(t) \geq 0\ rad/s,\ u_a(t) \neq 0\ V, \\ 0.001 & -0.005\ \text{rad}/s < \omega_m(t) < 0.005\ rad/s,\ u_a(t) = 0\ V, \\ t_1\omega_m(t) + t_2 & \omega_m(t) \leq -0.005\ rad/s,\ u_a(t) = 0\ V, \\ t_3\omega_m(t)^2 + t_7\omega_m(t) + t_4 & \omega_m(t) \geq 0.005\ rad/s,\ u_a(t) = 0\ V, \end{cases} \tag{3.27}$$

where the model nomenclature is given in Table 3.1.

The variables t_2, t_4, t_5, and t_6 are influenced by the change in applied voltage $\frac{du_a}{dt}$ (V/s), the rotational velocity $\omega_m(t)$, and the applied voltage u_a. The variables are given by

$$q(u_a) = [t_2, t_4, t_5, t_6] = \begin{cases} [t_{2_{-1}}, -0.0135, -0.003, 0.005] & \frac{du}{dt} > 0.0\ V/s, \omega_m < -0.005\ rad/s, \\ [0.018, t_{4_{-1}}, -0.003, 0.005] & \frac{du}{dt} < -0.10\ V/s, \omega_m > 0.005\ rad/s, \\ p(u_a) & \text{all other instances}, \end{cases} \tag{3.28}$$

where

$$p(u_a) = [t_2, t_4, t_5, t_6] = \begin{cases} [0.018, -0.0135, -0.003, 0.005] & |u_a| \leq 0.2\ V, \\ [0.018, -0.0135, 0.0015, -0.0175] & 0.2\ V < |u_a| \leq 0.4\ V, \\ [0.02, -0.0135, 0.001, -0.0175] & 0.4\ V < |u_a| \leq 0.45\ V, \\ [0.018, -0.0135, -0.0005, -0.005] & 0.45\ V < |u_a| \leq 0.5\ V, \\ [0.02, -0.0135, -0.0005, 0.0] & 0.5\ V < |u_a| \leq 0.55\ V, \\ [0.018, -0.0115, -0.0015, 0.0] & 0.55\ V < |u_a| \leq 0.6\ V, \\ [0.02, -0.015, -0.002, 0.02] & 0.6\ V < |u_a| \leq 0.65\ V, \\ [0.016, -0.011, -0.002, 0.001] & 0.65\ V < |u_a| \leq 0.7\ V, \\ [0.014, -0.0125, -0.0025, -0.01] & 0.7\ V < |u_a| \leq 0.75\ V, \\ [0.018, -0.0125, -0.0025, 0.01] & 0.75\ V < |u_a| \leq 0.8\ V, \\ [0.015, -0.01, -0.0025, -0.005] & 0.8\ V < |u_a| \leq 0.85\ V, \\ [0.0145, -0.0115, -0.0025, -0.005] & 0.85\ V < |u_a| \leq 0.89\ V, \\ [0.0145, -0.001, -0.0025, -0.005] & 0.89\ V < |u_a| \leq 0.92\ V, \\ [0.012, -0.007, -0.003, -0.001] & 0.92\ V < |u_a| \leq 0.98\ V, \\ [0.001, -0.001, -0.003, -0.001] & 0.98\ V < |u_a| \leq 2\ V, \\ [0.018, -0.0135, -0.003, 0.005] & |u_a| > 2\ V. \end{cases} \tag{3.29}$$

Table 3.1. Nomenclature for outer gimbal load torque function $T_{LG}(t)$ variables determined with trial and error.

Variable	Value
t_1	0.05 Nms/rad
t_2	$q(u_a)$ Nm
t_3	0.05 $\text{Nms}^2/\text{rad}^2$
t_4	$q(u_a)$ Nm
t_5	$q(u_a)$ Nm
t_6	$q(u_a)$ Nms/rad
t_7	0.015 Nms/rad

As seen in (3.28), in certain instances, the value of t_2 or t_4 equal their values from the previous simulation time step $t_{2_{-1}}$ or $t_{4_{-1}}$, respectively, in all cases t > 0.

The load torque function $T_{LG}(t)$ incorporates (3.27), (3.28), (3.29), as well as the constants as defined in Table 3.1, and is illustrated in Fig. 3.16. The load torque function variables are determined through trial and error process based on the stop and start movements of the outer gimbal. The goodness of fit according to (3.9) is 94.06 %.

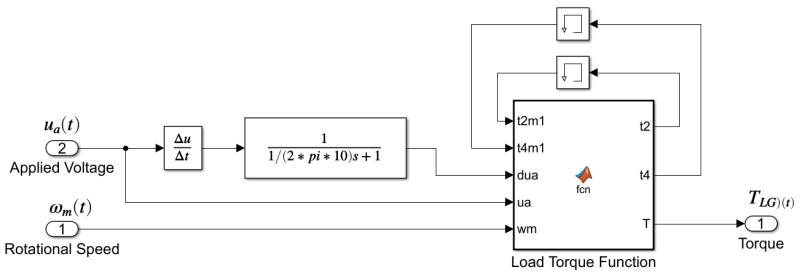

Figure 3.16. Outer gimbal non-linear simulation model gimbal load torque function.

The complete non-linear simulation model is shown in Fig. 3.17 where $T_{LS}(t)$ is given by (3.11), the applied voltage $u_a(u)$ by (3.26), and $T_{LG}(u)$ by (3.27).

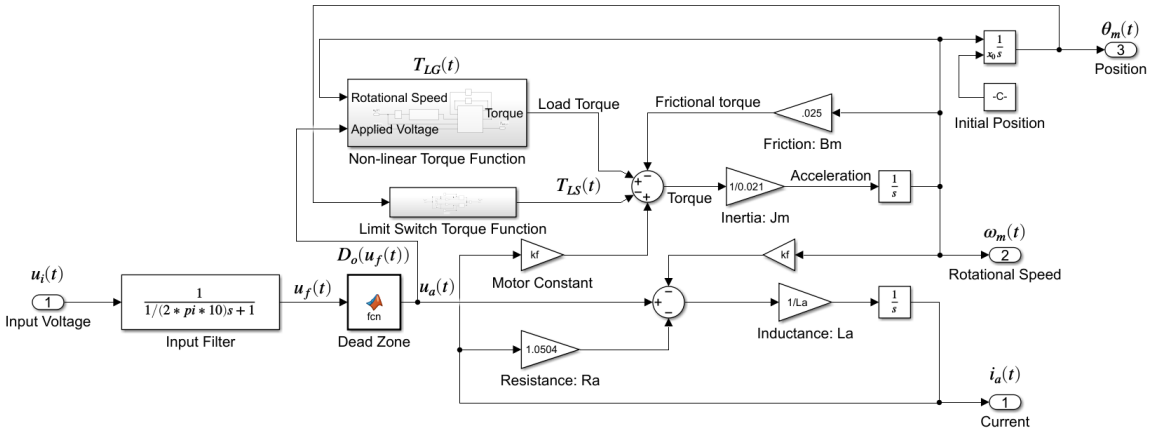

Figure 3.17. Outer gimbal non-linear simulation model.

Results from simulating the outer gimbal non-linear simulation model in Fig. 3.17 are shown in Fig. 3.18. It can be seen from the figure that the model output fits well onto measured data. Using (3.9) the goodness of fit of the non-linear simulation model position output is shown in Fig. 3.19. The non-linear simulation model position output is compared with the measured position data sets. The average of the goodness of fit between the measurement data as reference and the simulation data is 94.06%.

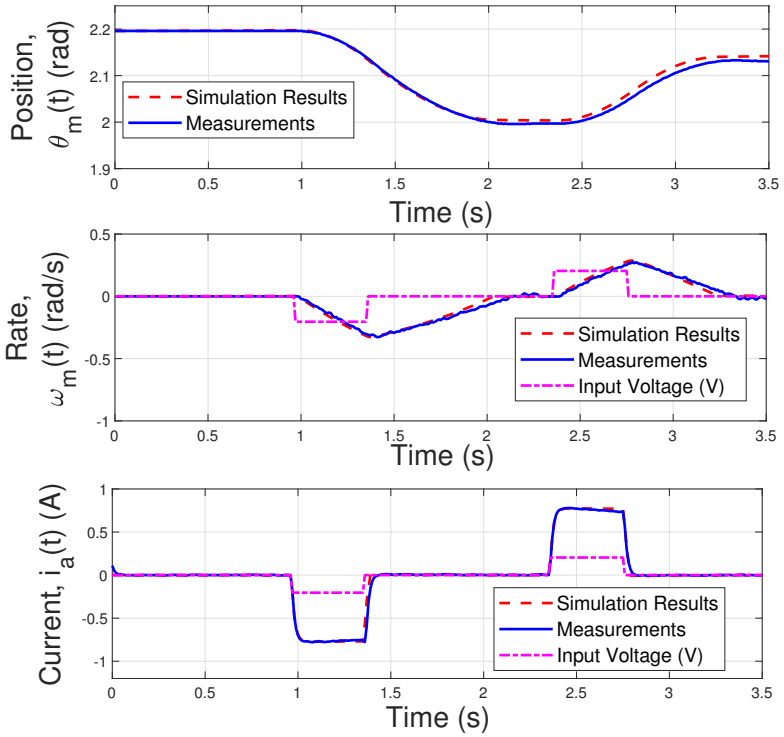

Figure 3.18. Outer gimbal non-linear model results with corresponding measured data set. The input voltage has values of $\pm$ 0.204 V.

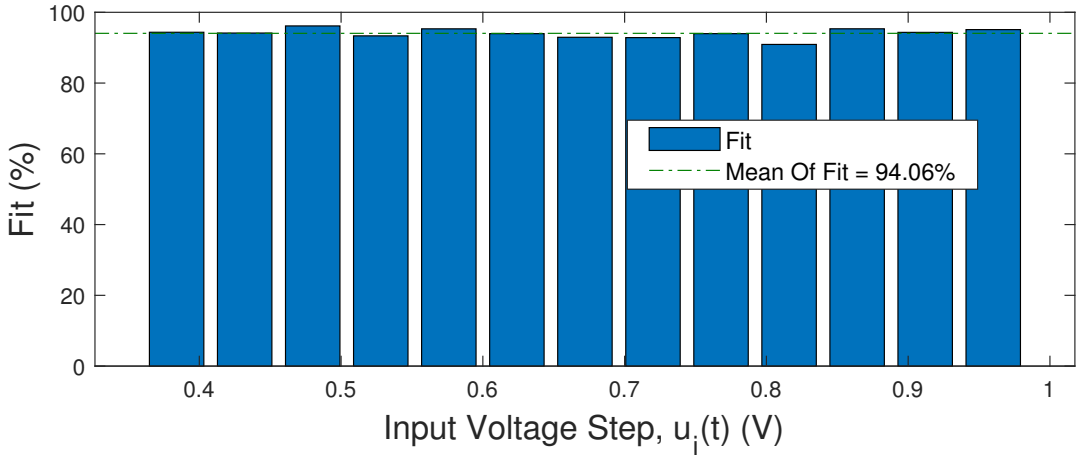

Figure 3.19. Outer gimbal non-linear model position fit.

3.4.2 Outer gimbal simplified non-linear model

The outer gimbal simplified non-linear model is a reduction of the non-linear model to a dead zone function, linear transfer functions, and a gain function. The gimbal reacts differently when it moves and when it comes to a standstill, which influences the accuracy of the simplified model.

The gain function $r(u_a)$ is derived by comparing simulation model position data sets onto measured position data sets until they correspond for different applied voltage steps. The gain values are presented graphically in Fig. 3.20, as they were obtained with tuning and trial and error processes for each applied voltage step value. Similar to the inner gimbal (3.20) there are two different functions for positive applied voltage steps and negative applied voltage steps. The polynomial gain functions in (3.30) for positive and negative voltages are obtained with Matlab basic fitting functions. The RMS difference between the polynomial equation and data points are 0.076 V/V for negative applied voltages and 0.1976 V/V for positive applied voltages and are computed using (2.8).

$$r(u_a) = \begin{cases} -1.923u_a^3 - 4.584u_a^2 - 3.701u_a - 0.3271 & u_a < 0\ V, \\ 0.4479u_a^3 - 3.173u_a^2 + 3.582u_a - 0.4804 & u_a > 0\ V. \end{cases} \tag{3.30}$$

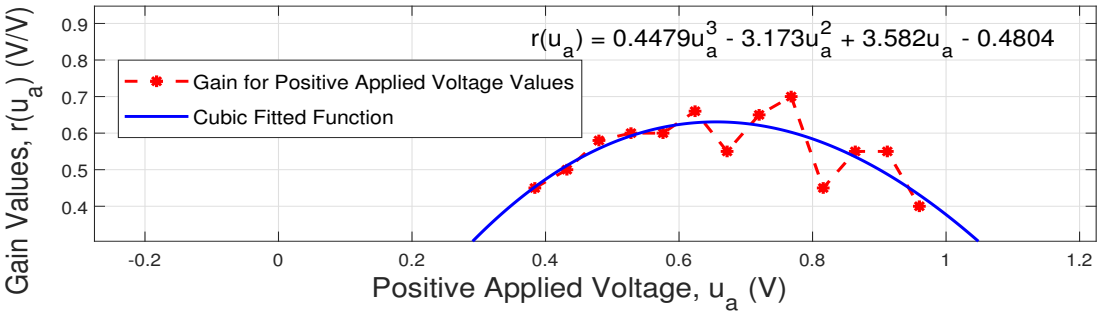

(a) Outer gimbal simplified non-linear model gain values for positive applied voltages.

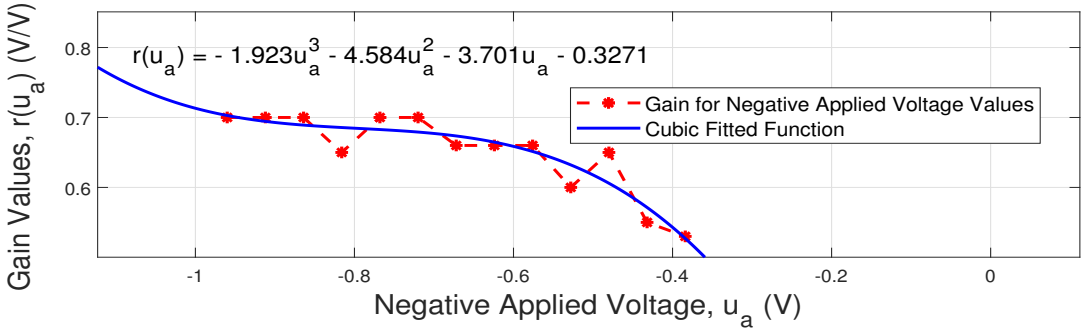

(b) Outer gimbal simplified non-linear model gain values for negative applied voltages.

Figure 3.20. Outer gimbal simplified non-linear model gain and its fitted gain function for positive applied voltages,(a), and negative applied voltages, (b).

Through tuning, a low pass filter (3.31) was derived at that allows for emulation of the simulation data and the measured data.

$$\frac{\theta_m(s)}{\Gamma(s)} = \frac{1}{s}\left(\frac{1}{1/(2\pi 0.6)s+1}\right), \tag{3.31}$$

$$\gamma(t) = r(u_a(t))u_a(t), \tag{3.32}$$

where $\gamma(t) = \mathcal{L}^{-1}(\Gamma(s))$ [V] is the applied voltage $u_a(t)$ amplified with $r(u_a(t))$ before it is passed to the low pass filter (3.31).

The simplified non-linear model is described in the following Fig. 3.21. The goodness of fit results are shown below. It includes the input filter (3.24), and the dead zone function (3.25), as well as the gain function with low pass filter (3.31) and the amplification function (3.32).

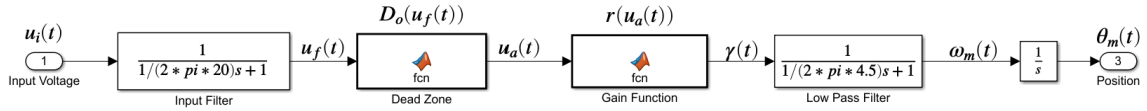

Figure 3.21. Outer gimbal simplified non-linear model.

The results from the simplified non-linear simulation model are shown in Fig. 3.22. It is clear that the model follows the measured data sets relatively accurately, but not as close as the non-linear model. The position data fit determined using (3.9) is shown in Fig. 3.23. The average of the fit is 83.75 % which is less accurate than the outer gimbal non-linear model.

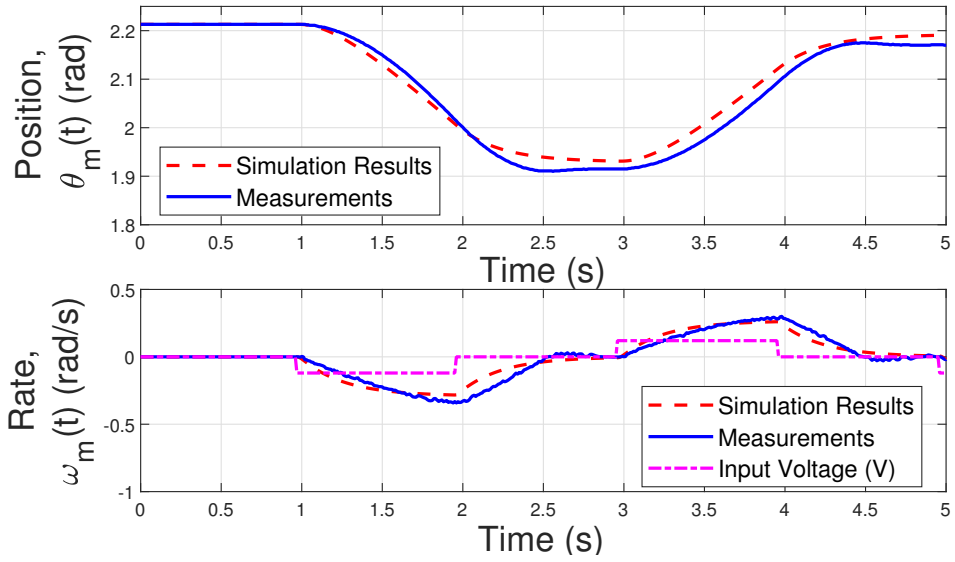

Figure 3.22. Outer gimbal simplified non-linear model results with $\pm$ 0.12 V input voltage steps.

3.4.3 Outer gimbal linear simulation model

The outer gimbal linear simulation model is approximated from the simplified non-linear model. It contains linear transfer functions with a linear gain.

The gain was determined as the average gain value from the data points used to determine (3.30), and has a value of 0.6038 V/V. The input filter (3.24) and (3.31) is maintained. The function of $r(u_a)$ is replaced with the gain of 0.6038 V/V. The resulting frequency domain equation for the linear model is given in (3.33). The corresponding outer gimbal linear model is shown in Fig. 3.24.

$$\theta_m(s) = \frac{0.6038}{s}\left(\frac{1}{1/(2\pi 10)s+1}\right)\left(\frac{1}{1/(2\pi 0.6)s+1}\right)E_i(s) \tag{3.33}$$

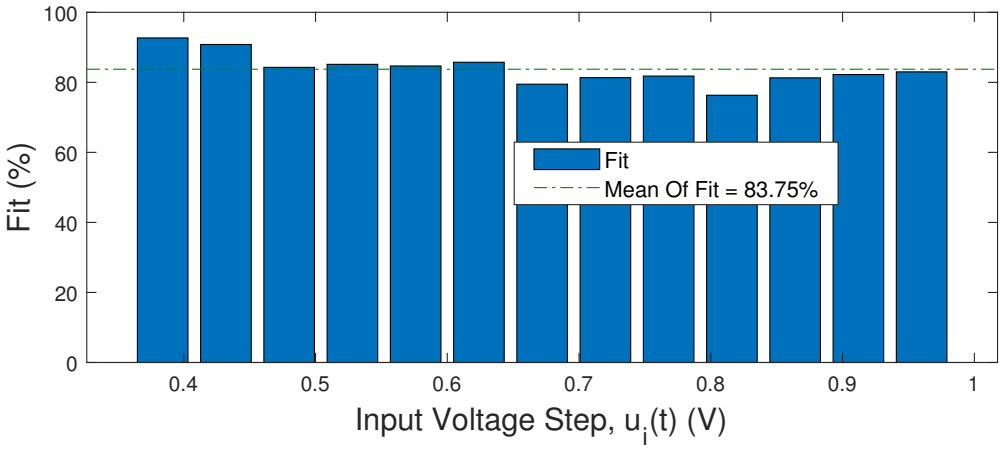

Figure 3.23. Outer gimbal simplified non-linear model position comparison with measured data sets. The input voltage shown is four times smaller.

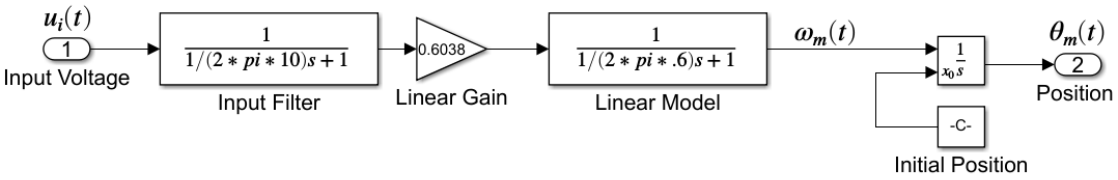

Figure 3.24. Outer gimbal approximated linear simulation model.

The results of the linear model are shown in Fig. 3.25. The fit as calculated using (3.9) is shown in Fig. 3.26. It is clear that the fit of 72.48 % is less than in the non-linear and simplified non-linear models of Fig. 3.17 and Fig. 3.21 respectively.

3.5 CONCLUSION

This section shows the development of three simulation models for each gimbal. The non-linear simulation model contains all the non-linear elements of the system and represents most accurately the movement of the gimbals. The accuracy of the models is determined by computing the fit between the position of the simulation model and the measured position of the gimbal for different input voltage steps. The simulation models are developed using a different set of measurements. Simplification of the non-linear simulation model leads to the simplified non-linear simulation model. The simplified non-linear simulation model contains non-linear gain functions and a linear transfer function.

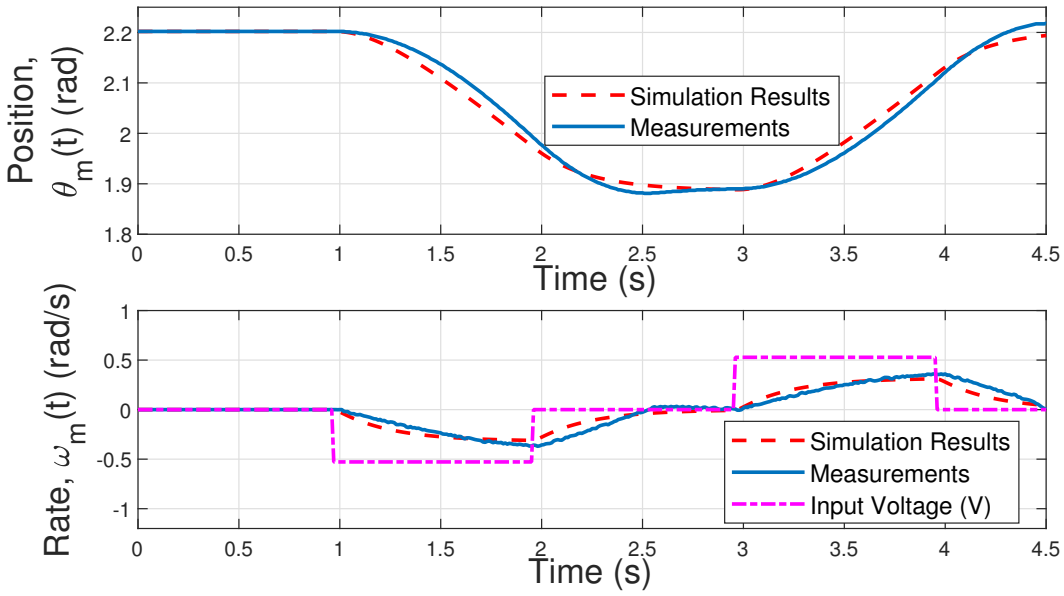

Figure 3.25. Outer gimbal linear model results with ± 0.528 V input voltage steps.

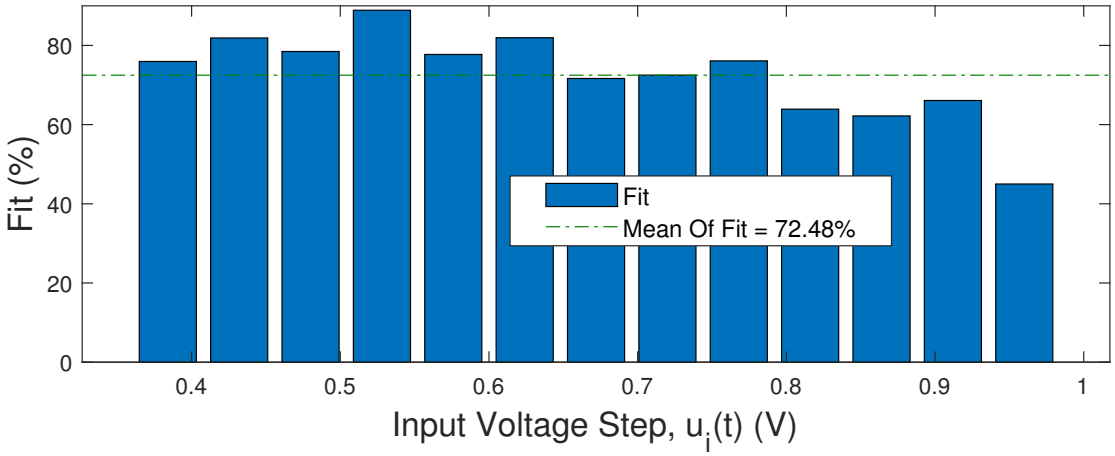

Figure 3.26. Outer gimbal linear model position comparison with measured data sets.

The linear simulation model uses the average gain value of the functions in the simplified non-linear simulation model.

The fit average values for all the models are summarised in Table 3.2 for the inner gimbal and Table 3.3 for the outer gimbal. The accuracy of the action of the gimbal models reduces with each reduction of model complexity and attempt at linearisation. The average fit values are the lowest for linear models.

Table 3.2. Inner gimbal model evaluation.

Model	Average fit
Non-linear model	94.17 %
Simplified non-linear model	91.86 %
Linear model	48.09 %

Table 3.3. Outer gimbal model evaluation.

Model	Average fit
Non-linear model	94.06 %
Simplified non-linear model	83.75 %
Linear model	72.48 %

On the inner gimbal, the fit for difference in position for a 0.24 V input voltage step is -83 %. This is the smallest input voltage value that falls out of the dead zone range. For all other step tests the fit values are above 79 %. The inaccurate movements of the lowest voltage reduce the model average fit value to 48.08 %. If that input voltage fit is left out of the dataset, the average fit result obtained would be 81.02 %.

Controller development is shown in Section 4. The simulation models developed in this section are used as the foundation of establishing control of the actual gimbals in order to emulate flare trajectory accurately.

CHAPTER 4 CONTROL

This section shows the development of controllers for each gimbal. The approach followed is similar to approaches outlined by (Golnaraghi and Kuo, 2003) and (Skogestad and Postlethwaite, 2007). Golnaraghi and Kuo (2003) describes a three-step process which starts with a review of the design specification. In this case the client requires flare trajectory emulation with the gimbals. The second step is to determine the control configuration, and the last step described byGolnaraghi and Kuo (2003) is to determine controller values to achieve the design goal of flare trajectory emulation with a specified maximum mRMS position error.

The control system design process outlined by Skogestad and Postlethwaite (2007) is more detailed. The process followed in this study is based on this process. Skogestad and Postlethwaite (2007) admits that it is not always necessary to execute all the steps. The steps outlined for this process were repeated until the results shown in this dissertation were obtained.

The process starts with studying and obtaining information of the gimbal system, and the flare trajectory to be emulated. The second step is modelling and simplification of the models. This is seen with the flare trajectory polynomial function definition on a gimbal scale, and the simplification of the gimbal models from non-linear models, to simplified non-linear models and finally to linear models. Thirdly, he suggests scaling variables and analysing the resulting model to determine its properties. This was briefly executed with the scaling the position of the gimbals, but it is not deemed helpful to show in the study.

The performance of the controller is measured in terms of its ability to emulate flare trajectory. This is based on the client requirement for flare trajectory emulation on a HILS platform.

Therefore, the gimbal position is chosen as the variable to be controlled. The performance of the controller is measured in terms of the maximum mRMS position error.

Next, the controller is designed as outlined in this section. During the initial phase of the study, a geared motor was selected instead of the gear-less one. Before the implementation of the geared motor, cascade control was developed, with an inner current feedback loop, middle velocity feedback loop, and outer position feedback loop. The current became negligibly small with the implementation of a geared motor to be used meaningfully with this controller. Some issues were experienced with the geared motor which included slow movement and low torque. It was also difficult to characterise the non-linear simulation model. Therefore, a decision was made to rather use the gear-less motor. At this stage, the controller developed was not changed back to cascade control, but position control was kept. One of the reasons was that the rate is derived from the position with an alpha-beta filter. The filter is less reliable than the encoder measurements on each gimbal. There is enough time in the system to sense position and to execute the control loop. This also place a smaller burden on the processor. So even though the gear-less motor consumes more current than the geared one, the controller was kept as a position controller.

The further developed control configuration is initially negative feedback control with initially only linear control in the forward path. The controller is modified in an attempt to compensate for the non-linear properties in the gimbal system. This shown is shown with implementation of gain scheduling controlling action in order to compensate for the different gains experienced when trying to control the gimbals. The controllers were analysed and finally a feed forward controlling action was chosen to be added to the control system. The controllers were evaluated using the simulation models, as well as with testing the respective controllers on the actual gimbals. The steps were repeated to achieve accurate positions.

The linear simulation model forms the foundation for the development of a linear controller. This controller is tested on the simplified non-linear simulation model, non-linear simulation model, and the actual gimbal. The simplified non-linear simulation model is the foundation for development of a second type of controller with non-linear elements in the form of a gain scheduling function. The gain scheduling function is applied with a PD compensator. The use of derivative control action improves the delayed response and off set in the error observed with the linear controller. The gain scheduling controller is tested on the non-linear simulation models and the actual gimbals.

Lastly, a final controller is developed using the non-linear simulation models. A feed-forward compensator is added to the control system path. The feed-forward compensator improves on precision over the gain scheduling and linear controllers. All the controllers are tested with the actual gimbals and compared to each other.

Accurate control is regarded as mRMS position error below 2.00 *m*rad for each gimbal. The aim is to control each gimbal as accurately as possible. This value corresponds to a position error of less than 0.367 m in the real world horizontal and vertical flare paths and implies an error of less than 0.60 % over the range of flare trajectory emulation.

4.1 CONTROL SYSTEMS STRATEGIES

Different controller strategies are evaluated in this study, and they contain linear or non-linear characteristics. Non-linear control techniques are necessary as the system displays significant non-linear behaviour.

Linear control techniques, such as different variants of the PID (Proportional-Integral-Derivative) controller are relatively simple to implement and is an effective control method widely used across industries in various applications (Golnaraghi and Kuo, 2003). PID controllers and its variations are frequently applied to provide dc motor control solutions (de Carvalho, Ganzaroli, do Couto, Dias and Calixto, 2017; Onawola, Adewunmi, Ehiagwina and Iromini, 2017; Bhatti, Daraz and Malik, 2016; Reynoso-Meza, Sanchis, Blasco and Freire, 2016; Zhang, Li, Luo and Shang, 2017; Ganzaroli, de Carvalho, Dias, Reis, Alves, Domingos and Calixto, 2015; Bai, 2015; Beltran-Carbajal, Valderrabano-Gonzalez, Rosas-Caro and Favela-Contreras, 2015b; Beltran-Carbajal, Valderrabano-Gonzalez and Rosas-Caro, 2015a; Zaki, El-Bardini, Soliman and Sharaf, 2018). Current studies focus on improving PI or PID controllers or other variations of the PID controller strategies by optimizing the controller tuning techniques (Azarmi, Tavakoli-Kakhki, Sedigh and Fatehi, 2016; Zaky, 2015; de Carvalho *et al.*, 2017; Reynoso-Meza *et al.*, 2016; Ganzaroli *et al.*, 2015) or developing adaptive or robust controllers (Zhang *et al.*, 2017; Bai, 2015; Zaki *et al.*, 2018; Xue and Li, 2018; El-Nagar, 2016; Rusnak, Hertz and Dana, 2016; Tepljakov, Gonzalez, Petlenkov, Belikov, Monje and Petráš, 2016; Ahmed, Mohan, Chauhan and Sharma, 2013; Yan, Wang, Jia and Li, 2012).

In systems that experience a time delay, feed-forward compensation is a type of linear control that acts

pre-emptively on changes in the set point. It has the capacity to start correcting errors, before they have even occurred. For a feed-forward controller a gain together with a high-pass filter provides this capability. This also improves precision of the control action (Chen, Rai and Tsao, 2019). Operation of feed-forward controllers should be in conjunction with a feedback controller, to allow the system to compensate for the effects of feed-forward control (Chen *et al.*, 2019; Imen and Shakeri, 2007).

The non-linear controller strategy investigated for implementation in this study is gain scheduling (Bett, 2004). Gain scheduling is a method of implementing control on a non-linear system. It is a control approach employable on mechatronic systems with position controllers. The method of gain scheduling comprises of interpolating between sets of linear controllers derived from the operating points of several linearised plant sets (Bett, 2004; Mehendale and Grigoriadis, 2004; Rugh and Shamma, 2000). Bett (2004) explains that the deduced controller is a linear system with variables, or gains, that are adapted, or scheduled, as a function of external parameters. This functionality allows the controller to adapt to changing operation scenarios.

According to Bett (2004), gain scheduling compensation guarantees closed loop stability in a local sense. The development of this Linear Parameter Varying (LPV) system involves implementing analytical methods to arrive at a scheduling law.

The idea behind gain scheduling is to linearise a non-linear plant around a set of operation scenarios. A satisfactory linear controller can then be designed for each linearised plant. Gain scheduling is then employed with interpolation of the linear controllers. Therefore, non-linear design is subdivided into simpler linearised designs.

Further strategies to optimize controller tuning include studying heuristic and deterministic techniques and comparing the results. Investigations with a Dynamic Matrix Control (DMC) controller (de Carvalho *et al.*, 2017), and another with a cascaded PI controller (Ganzaroli *et al.*, 2015), compared results between heuristic and deterministic optimization tuning. Both studies showed better results by employing the heuristic strategy. These studies were only tested in simulations and not on a practical system. Heuristic strategies include evolutionary algorithms such as Particle Swarm Optimization (PSO) (Kanojiya and Meshram, 2012), Genetic Algorithms (GA) (Kaya and Nalbantoğlu, 2016; Ganzaroli *et al.*, 2015; de Carvalho *et al.*, 2017), and other neural network strategies (El-Nagar, 2016; Zhang *et al.*, 2017; Bai, 2015; Zaki *et al.*, 2018).

El-Nagar (2016), employed an adaptive PI controller strategy to control a dc motor using a Type-2 Fuzzy Neural Network (IT2FNN). The study was conducted practically and demonstrated that the strategy shows an improvement of the system response. Dynamic neural network methods have been employed on brushed PM dc motors by Zhang *et al.* (2017), and proved the efficiency of adaptive optimal speed control for such motors with friction. According to Zhang *et al.* (2017) this is the first research which employs the method on brushed PM dc motors. The simulations show the promise of an efficient dynamic strategy. Bai (2015) investigates solving a tracking problem with a dc motor by employing an adaptive neural controller. Bai (2015) conducted the study at simulation level and suggested the design of an adaptive strategy with minimal parameters for future work.

Deterministic strategies investigated are Quasi-Newton (de Carvalho *et al.*, 2017), and Fractional Order (FO) methods (Azarmi *et al.*, 2016; Tepljakov *et al.*, 2016; Rahimian and Tavazoei, 2014), as well as adaptive control algorithm techniques (Rusnak *et al.*, 2016; Pathak and Adhyaru, 2016) and a mini-max approach (Yassine, Messaoud and Sofiane, 2015). The FO tuning optimization strategy is favourably implemented on practical dc motor applications. Future work can be expanded to work in different applications (Azarmi *et al.*, 2016; Tepljakov *et al.*, 2016).

Further literature in this field focusses on different control strategies and comparisons between the controllers (Bhatti *et al.*, 2016; Yassine *et al.*, 2015; Shrivastva and Singh, 2014; Stinean, Preitl, Precup, Dragos, Petriu and Radac, 2013), as well as investigating control solutions for the tracking problem with dc motors (Beltran-Carbajal *et al.*, 2015b; Beltran-Carbajal, Favela-Contreras, Valderrabano-Gonzalez and Rosas-Caro, 2014; Morales, Somolinos and Sira-Ramírez, 2014). The study from Bhatti *et al.* (2016) recommends future work on evolutionary computing control using heuristic methods. Reynoso-Meza *et al.* (2016) utilized evolutionary multi-objective optimization for tuning PI controller parameters in multivariable systems, but cites these algorithms as useful in single input single output systems and that future work should focus on developing progressive techniques and more practical applications could make this work feasible. From these studies it is evident that investigation of more adaptive, optimized, and robust strategies is a field of growing interest.

4.2 LINEAR MODEL CONTROL SYSTEM

In order to develop a controller for the gimbal linear models, Matlab Root Locus and Bode plot tools are used. These tools assist with design of the compensator by determining placement of compensator poles and zeroes.

The aim of the control system is to enable each gimbal to follow a distinct flare trajectory path, such as shown in Section 2.4.2. In the following subsection a linear controller is developed using these tools as well as the flare trajectory set point for the inner gimbal (2.9). Linear controller development for the outer gimbal follows after the inner gimbal, using the same tools and the flare trajectory set point for the outer gimbal (2.10). Linear controllers are tested on the simplified non-linear models as well as the non-linear models, and are evaluated on the actual gimbals.

4.2.1 Inner gimbal linear controller

The inner gimbal linear model from Section 3.3.3, (3.23) is simplified into a single transfer function as shown here.

$$G(s) = \frac{\theta_m(s)}{E_a(s)} = \frac{3.4}{0.0002814s^3 + 0.0433s^2 + s} \tag{4.1}$$

The roots of the characteristic equation of (4.1) show that the model has three left half plane poles, and it is a marginally stable system. The pole at 0 rad/s represents integral action present in the plant. The contribution of the pole at -125 rad/s is small in relation to the dominant pole at -28 rad/s. The dominant pole at -28 rad/s is a relatively fast pole and indicates that no compensation is required. A proportional controller should be sufficient.

The Bode plot of the linear model transfer function (4.1) in Fig. 4.1 shows the Gain Margin (GM) is 33.1 dB and the Phase Margin (PM) is 81.7 °. The GM and PM have large values and indicate that the plant is more sluggish, and less oscillatory. This means the plant is relatively stable.

For the development of the controller a proportional gain P of 2.4 V/rad is implemented (4.2). The control system as applied here is a closed loop negative feedback system with the plant (4.1) in the forward branch.

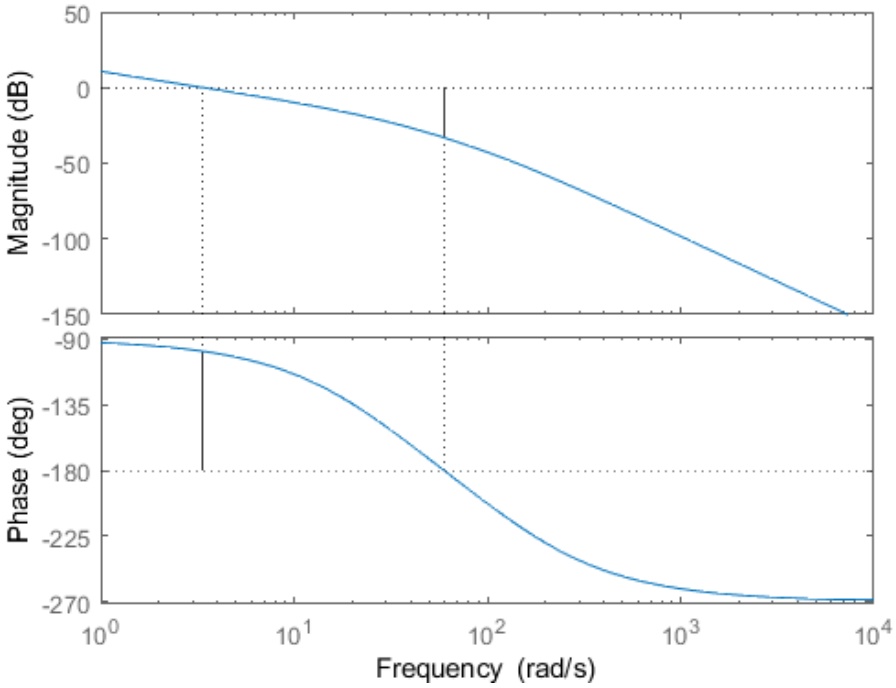

Figure 4.1. Inner gimbal linear model plant transfer function Bode plot with GM equal to 33.1 dB at 59.6 rad/s and PM equal to 81.7 ° at 3.37 rad/s.

$$\theta_e(s) = \theta_{sp}(s) - \theta_m(s) \tag{4.2a}$$

$$E_i(s) = P\theta_e(s) \tag{4.2b}$$

$$\theta_m(s) = PG(s)\theta_e(s) \tag{4.2c}$$

$$\theta_m(s) = 2.4\frac{3.4}{0.0002814s^3 + 0.0433s^2 + s}\theta_e(s) \tag{4.2d}$$

The position error $\theta_e(s)$ is the difference between the measured position $\theta_m(s)$ and position set point $\theta_{sp}(s)$. The controller is shown in Fig. 4.2. A proportional gain value of 2.4 V/rad results in the most satisfactory response in terms of quickest settling time and most stable reaction, when a step input voltage is applied. This corresponds to the principle of placing closed-loop poles midway between second order open loop poles. For a step input the rise time is 0.182 s, as shown in Fig. 4.3.

The linear controller is implemented with a flare trajectory set point on all three models and the actual inner gimbal. Due to the nature of the flare trajectory and the differences between each of the models and the gimbal, the gain is adjusted until the best response is obtained.

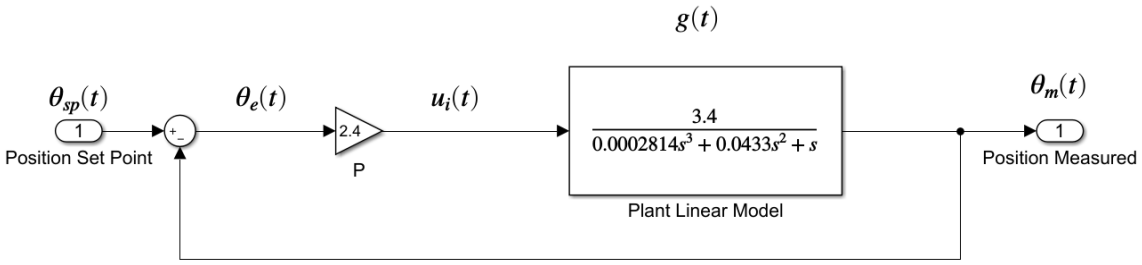

Figure 4.2. Inner gimbal linear model control.

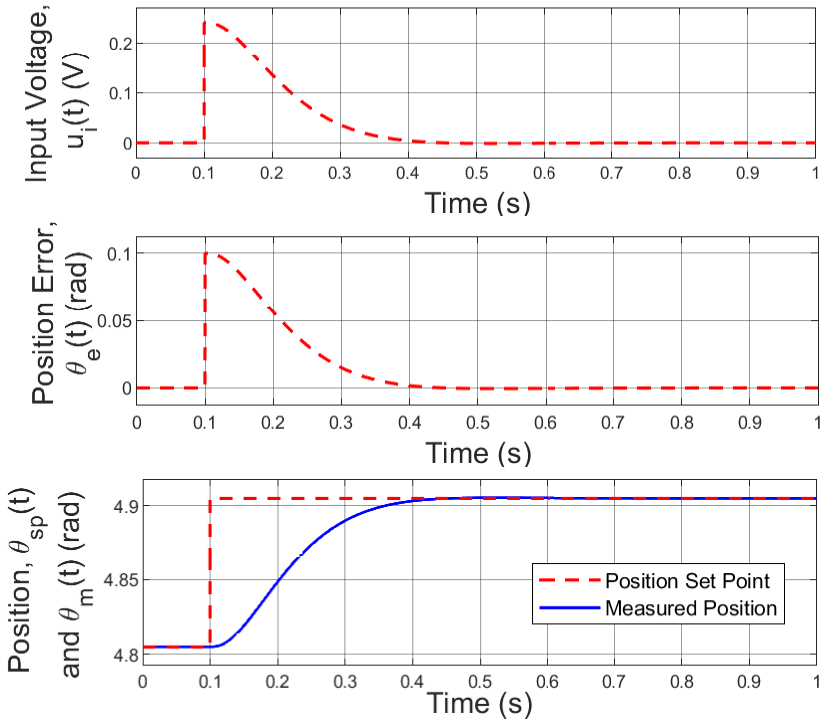

Figure 4.3. Inner gimbal linear model with proportional control and a step input set point.

This adjustment of the gain results in an increase of the gain for each model and the gimbal. This is necessary in order obtain a good response in terms of the required flare trajectory specification. The increase in gain might result in an unstable system if a step input is applied to the linear model, but since the requirement is that of a flare trajectory, and different models are used, as well as the gimbal, this is not applicable. Therefore, the gain can be increased to achieve satisfactory results for a flare trajectory set point. Some oscillatory behaviour is observed in the models and the gimbal, but since this is so small, it is not observable with the eye, and the oscillatory behaviour is not observed when the trajectory is complete. This might be attributed to limit cycling within the system.

The linear controller does not provide satisfactory results on the models or the gimbal, but forms the foundation for further development of a controller for each gimbal.

The results of linear control action on the linear model for flare trajectory set point (2.9) are shown in Fig.4.4. Due to the ramp nature of the flare trajectory, the proportional gain can be increased significantly. The internal model principle dictates that a double integrator is required in the loop, when the input is a ramp function. However, the reference signal is not a pure ramp, but also contains step behaviour and therefore an additional integrator was not used, but instead the loop gain was increased. On the linear model a gain P of 20 V/rad, gives the result as shown in Fig. 4.4. The best results are the responses that are stable and give the smallest error. Proportional control developed using the linear

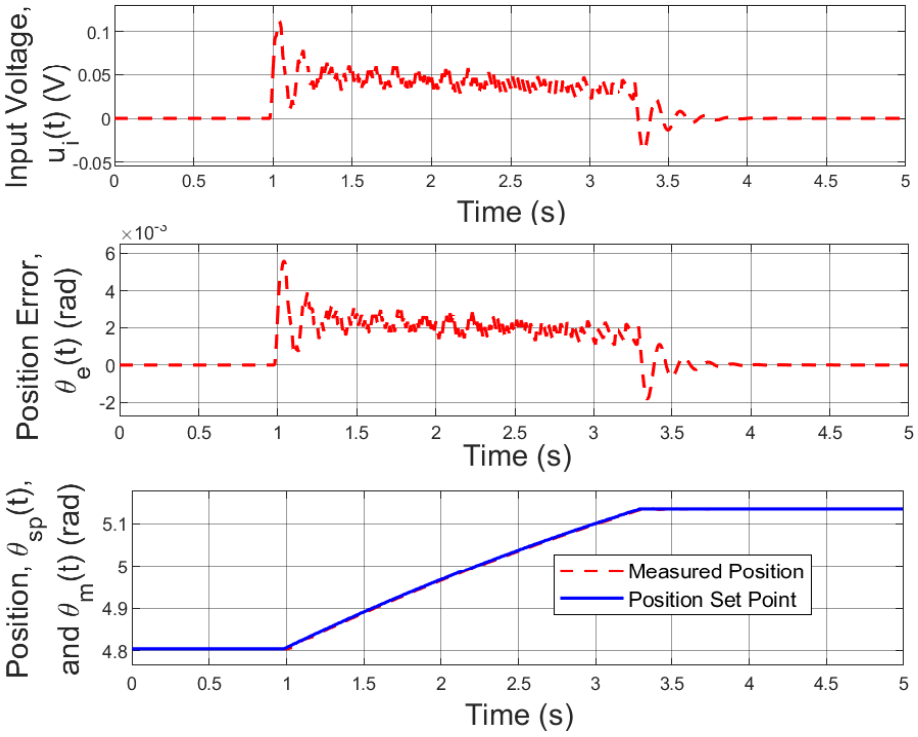

Figure 4.4. Inner gimbal linear model with proportional control and a flare trajectory set point.

model is tested on the simplified non-linear model Fig. 3.10 from Section 3.3.2 and the non-linear model Fig. 3.6 from Section 3.3.1. In both these models, their respective functions replace $G(s)$ as $\frac{\theta_m(s)}{E_i(s)}$ in (4.2). Results of both models following a flare trajectory set point (2.9) are shown in Fig. 4.5. The proportional gain of the simplified non-linear model delivers best results at 60 V/rad, and the non-linear model at a gain of 70 V/rad.

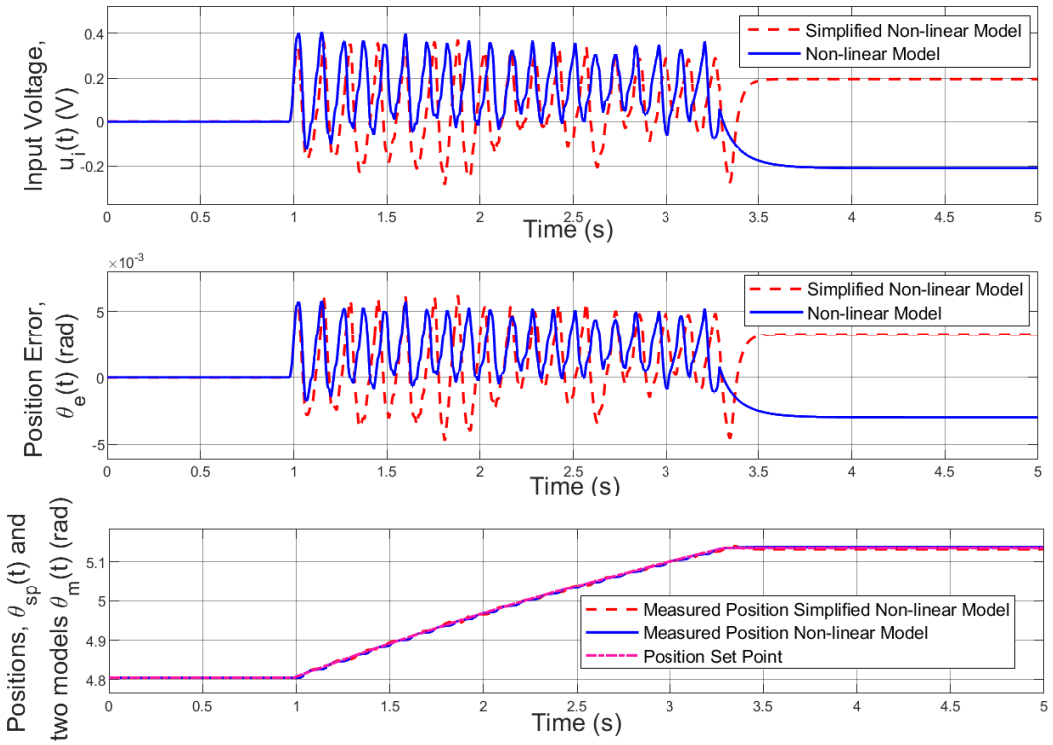

Figure 4.5. Inner gimbal linear controller results with a flare trajectory set point tested on the simplified non-linear model and the non-linear model.

The linear model proportional position controller is implemented on the actual inner gimbal. Results of linear control on the inner gimbal are shown in Fig. 4.6 with a flare trajectory set point. A gain of 70 V/rad on the actual inner gimbal results in the smallest error and most stable performance.

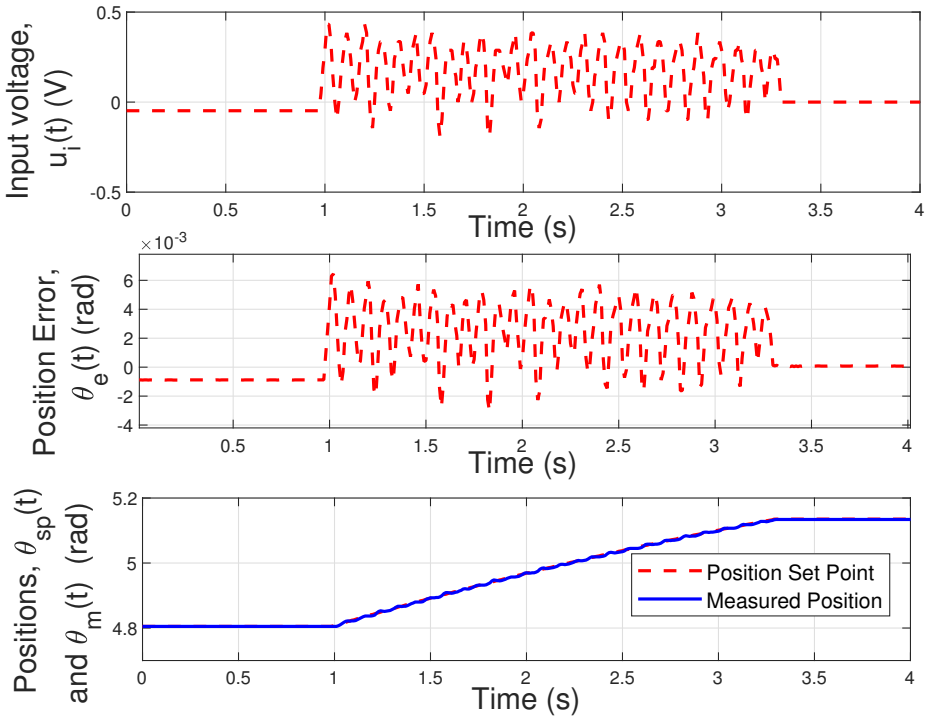

Figure 4.6. Inner gimbal linear controller results tested on the actual gimbal.

The mRMS position error is calculated using (4.3), it is implemented in Simulink with the "Moving RMS" block. It is a moving mRMS position error calculation with a 0.5 s window sample period and is calculated as follows

$$mRMS\,position\,error[k] = \sqrt{\frac{\sum_{n=max(1,k-N+1)}^{k}(\theta_e[n])^2}{min(k,N)}}, \tag{4.3}$$

where N is 50 samples, k is the sample, n is the count, and $\theta_e[k]$ is the position error. The samples occur every 0.01 s, which sets the moving window at 0.5 s.

The mRMS position error is shown in Fig. 4.7 for all four implementations discussed in this section. The maximum mRMS position error on the actual inner gimbal is more than the desired accuracy of less than 2.00 *m*rad and sits around 3.50 *m*rad. The maximum mRMS position error for the flare trajectory set point on the linear model with linear control is 2.80 *m*rad.

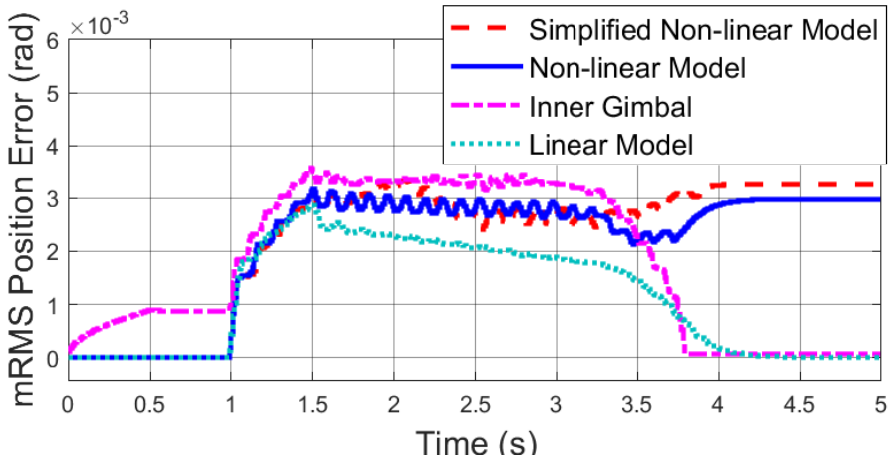

Figure 4.7. Linear controller mRMS position errors for the simplified non-linear model, non-linear model, actual inner gimbal, and linear model.

4.2.2 Outer gimbal linear controller

The linear model of the outer gimbal (3.33) as derived in Section 3.4.3 is converted into a single transfer function shown here.

$$G(s) = \frac{\theta_m(s)}{E_a(s)} = \frac{0.6038}{0.00422s^3 + 0.2812s^2 + s} \tag{4.4}$$

The roots of its characteristic equation stipulate poles in the left half plane of its Root Locus plot, which means it is marginally stable. Similar to the inner gimbal, there is a pole at 0 rad/s which is indicative of integral action present in the plant. There is an insignificant pole at -63 rad/s which does not exert much influence on system response. The third pole is the dominant pole and sits at -3 rad/s, which makes the system almost 10 times slower than the inner gimbal. The outer gimbal plant model is similar to the inner gimbal, but exhibits a slower response, which requires compensation.

The Bode plot of the plant in Fig. 4.8 shows the outer gimbal linear model plant has a GM of 40.9 dB and a PM of 80.5 °. The large GM and PM values indicate the plant has a stable, but sluggish response. The Matlab control system designer tool facilitates compensator development with placement of poles and zeros on the Root Locus of the closed loop function. The closed loop system under consideration is a negative feedback system with the plant (4.4) in the forward path. At first the dominant pole is cancelled by placing an equal zero at -3.74 rad/s. This compensates for slow responsive action.

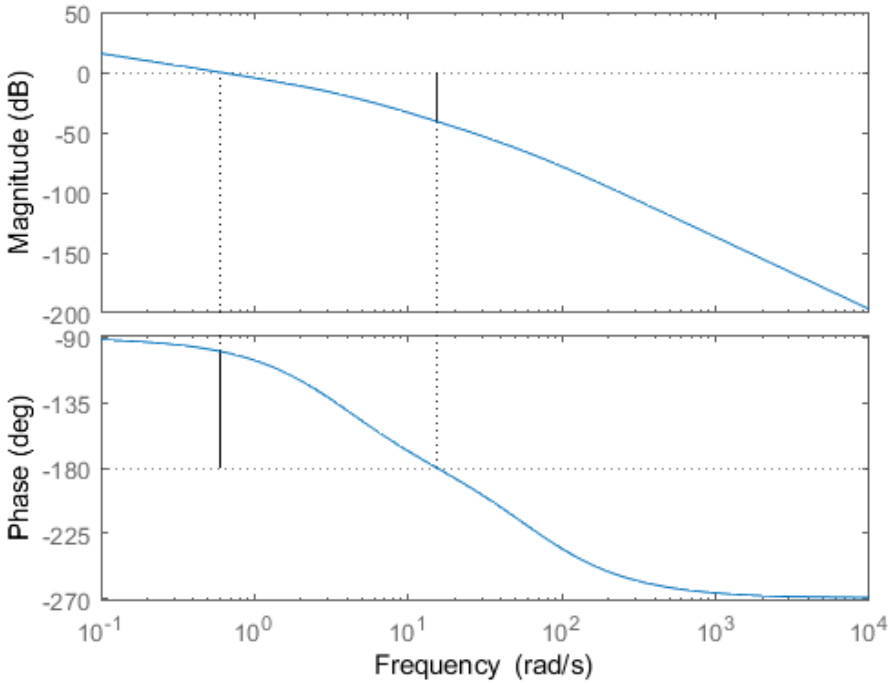

Figure 4.8. Outer gimbal linear model plant Bode plot of its transfer function showing GM equal to 40.9 dB (at 15.4 rad/s), and a PM equal to 80.5 °(at 0.596 rad/s.

Another pole is added at -20 rad/s. This dominant pole is placed almost seven times more to the left than the original dominant pole. This increases system response time. The aim with this is to achieve a similar, but slightly slower, response than with the inner gimbal. This is due to the fact that the outer gimbal is bigger and moves slower than the inner gimbal. The addition of this dominant pole results in a control signal of more than 24 V, which is above the motor driver rails. To reduce control voltage below 24 V, an additional pole is placed at -40 rad/s. This pole does not have a significant effect on the dynamic response of the closed loop, but reduces control voltage to below 24 V. With a gain of 8 V/rad, a desired similar response, albeit slightly slower, is achieved in comparison to the inner gimbal.

The resultant controller function is shown in (4.5) and is applied in the control system (4.6), as shown in Fig. 4.9.

$$C(s) = 8\frac{(1+0.27s)}{(1+0.05s)(1+0.025s)} \tag{4.5}$$

$$\theta_e(s) = \theta_{sp}(s) - \theta_m(s) \tag{4.6a}$$

$$\theta_m(s) = C(s)G(s)\theta_e(s) \tag{4.6b}$$

$$\theta_m(s) = 8\frac{(1+0.27s)}{(1+0.05s)(1+0.025s)}\frac{0.6038}{0.00422s^3+0.2812s^2+s}\theta_e(s) \tag{4.6c}$$

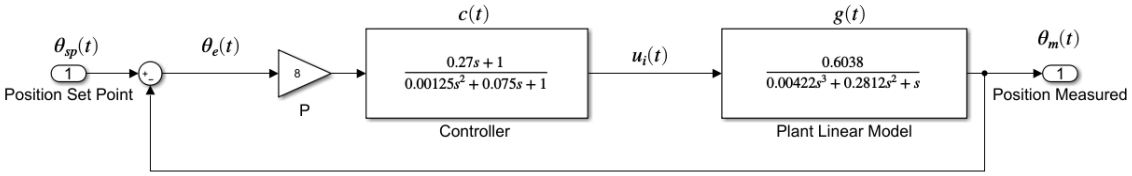

Figure 4.9. Outer gimbal linear controller.

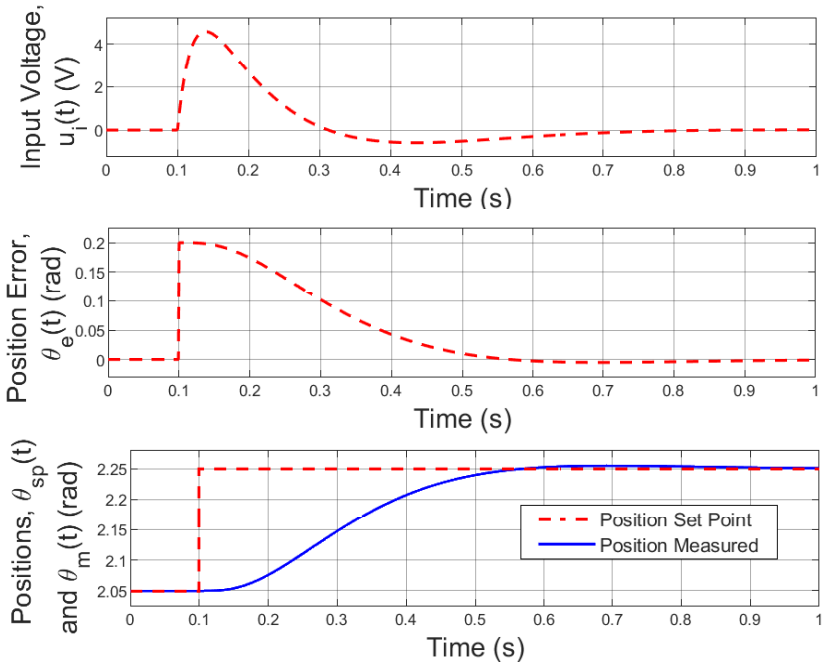

Figure 4.10. Outer gimbal linear control tested on the linear model with a step input.

The controller function performance is similar to the inner gimbal compensator performance. For a position change step input, the rise time is 0.268 s and the settling time is 0.656 s, as shown in Fig. 4.10.

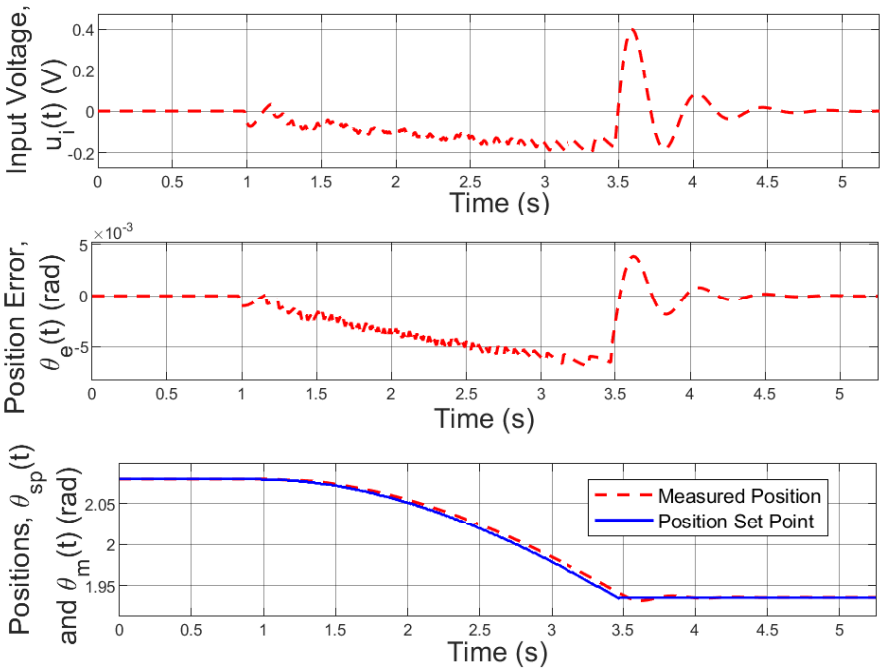

Figure 4.11. Outer gimbal linear control tested on the linear model with a flare trajectory set point.

The linear model with the linear controller (4.6) is simulated with a flare trajectory set point (2.10) and results are shown in Fig. 4.11. Similar to the inner gimbal linear controller, the gain is increased to improve the performance of the system for a flare trajectory set point. A gain value of 25 V/rad delivers the best results in terms of oscillations and responsiveness.

Fig. 4.12 shows the results of implementing linear control (4.5) with a flare trajectory set point (2.10) on the simplified non-linear model Fig. 3.21, of Section 3.4.2, and non-linear model Fig. 3.17, of Section 3.4.1. These functions respectively replace $G(s)$ in the form of $\frac{\theta_m(s)}{E_i(s)}$ in (4.6). Some oscillations are observed with the non-linear model. This can be attributed to non-linear elements in the plant. A gain of 45 V/rad for the simplified non-linear model and 65 V/rad on the non-linear model provides the best results in terms of stability and speed.

The linear controller (4.5) is implemented on the actual outer gimbal. To implement (4.5) in firmware it is discretised using Matlab $''c2d''$ function, with the $''tustin''$ option. The discretised equation is shown in (4.7). In the discretised controller equation (4.7), $[k]$ represents the current time step, $[k-1]$, the previous time step, and $[k-2]$ two time steps back.

$$u_i[k] = 8(2.011\theta_e[k-1] - 1.163\theta_e[k-2] + 0.1537u_i[k-1] - 0.002479u_i[k-2]) \quad (4.7)$$

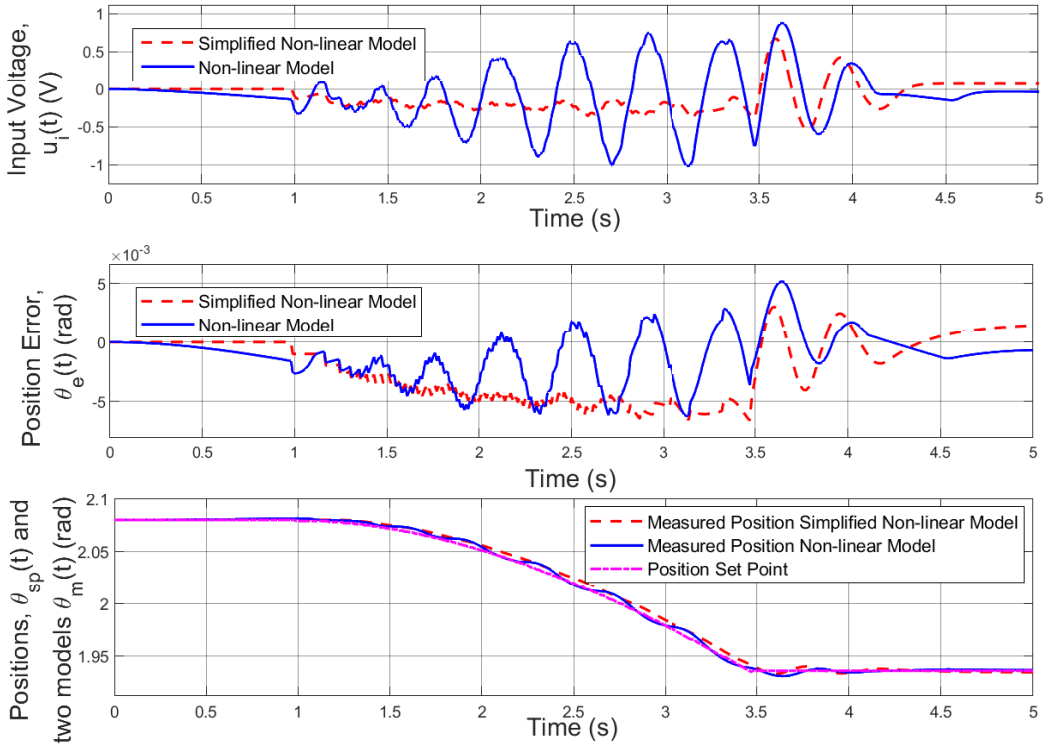

Figure 4.12. Outer gimbal linear controller tested on the simplified non-linear model and non-linear model with a flare trajectory set point.

The gain of 8 V/rad is adjusted in firmware until the desired response is obtained from the outer gimbal. A gain value of 80 V/rad delivers the best results. Fig. 4.13 shows the results of the linear controller on the actual outer gimbal. The same oscillatory behaviour observed in the non-linear model is also present with the actual outer gimbal. This is attributed to non-linear characteristics of the plant.

The mRMS position error values of the outer gimbal linear model, simplified non-linear model, non-linear model, and actual gimbal is shown together on Fig. 4.14 as obtained with the linear controller and calculated with (4.3). The maximum mRMS position error on the outer gimbal is 7.50 *m*rad, which falls outside the range of the desired accuracy of less than 2.00 *m*rad.

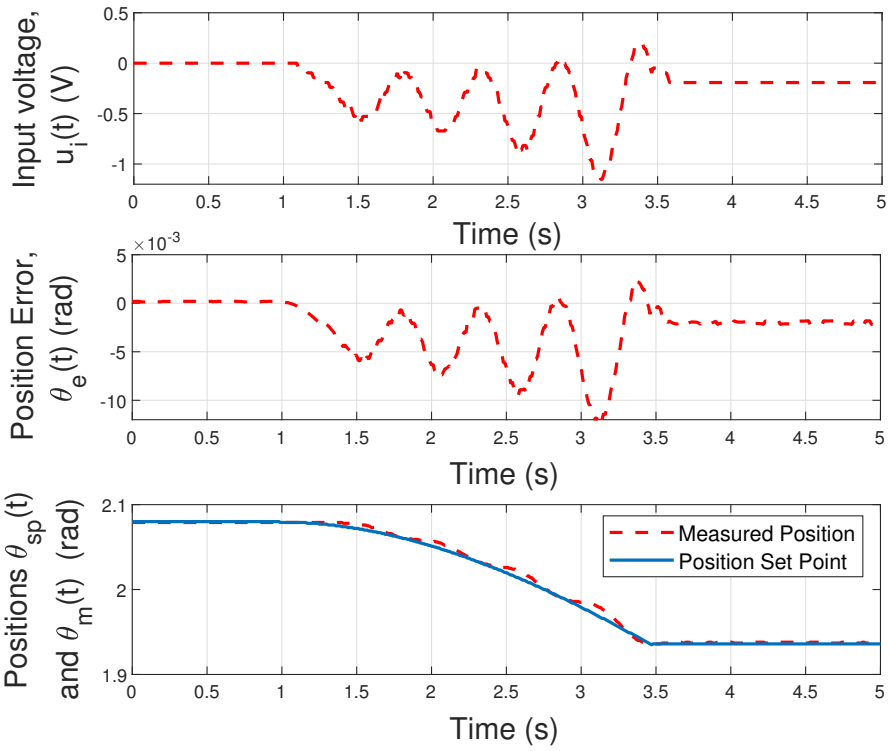

Figure 4.13. Outer gimbal linear controller tested on the actual gimbal with a flare trajectory set point.

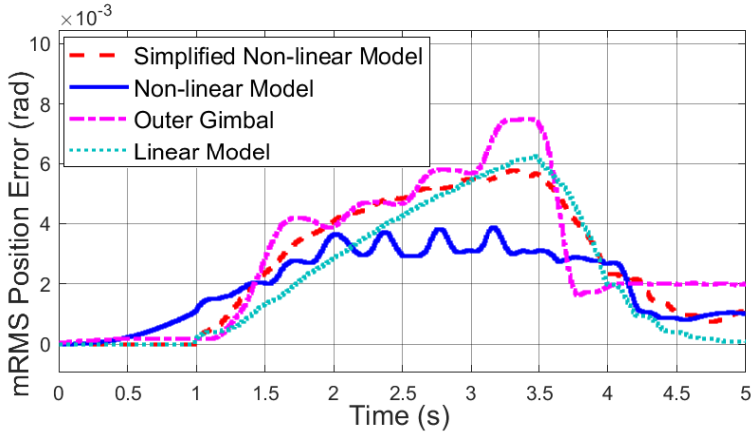

Figure 4.14. Outer gimbal linear control mRMS position error of the different outer gimbal models and actual outer gimbal with a flare trajectory set point.

4.3 GAIN SCHEDULING CONTROLLER

Gain scheduling development takes place by determining the inverse of the non-linear gain functions in the simplified non-linear model. The simplified non-linear model and its non-linear functions are discussed in Sections 3.3.2 and 3.3.2.

The inner and outer gimbals both have a non-linear gain function in their respective simplified non-linear models. The limits of the gain functions have to be considered. The limits of the values are a result of the small range of applied voltages available to take measurements with on each gimbal. The inverse of the gain functions employed in the simplified non-linear model are utilised as a method to compensate for the non-linear behaviour of the gimbals. The range of the inverse gain function is dependent on the range of available applied voltages to take measurements with. The values of the inverse gain functions are also limited due to this restriction.

The following sections show the inverse gain functions for each gimbal. It shows how each gimbal controller utilises the inverse gain function in the gain scheduling controller. The linear controller results are compared with the gain scheduling controller results for each actual gimbal.

4.3.1 Inner gimbal gain scheduling control

The simplified non-linear model Fig. 3.10 repeated in Fig. 4.15 for convenience, contains a non-linear gain function $v(u_a(t))$ that depends on the applied voltage. The non-linear gain functions (3.20) for positive and negative voltages are repeated in Fig. 4.16 for convenience.

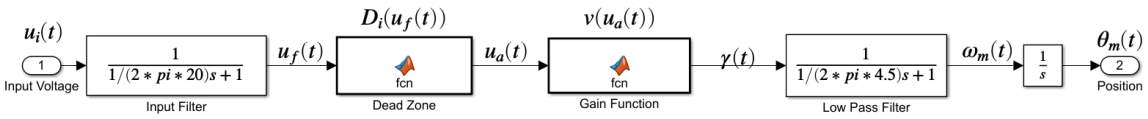

Figure 4.15. Inner gimbal simplified non-linear model.

The inverse gain is determined by computing the inverse of each non-linear gain data point from Fig. 4.16 and plotting it on a graph. The inverse gain values for positive and negative applied voltages respectively are shown in Fig. 4.17.

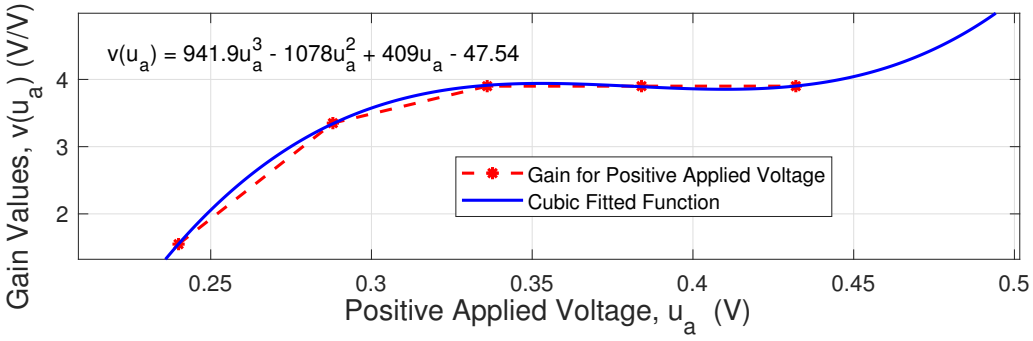

(a) Inner gimbal simplified non-linear model gain values for positive applied voltages.

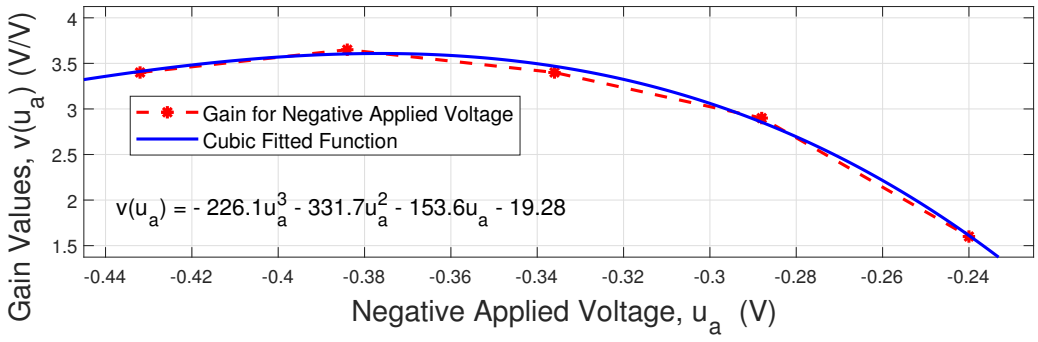

(b) Inner gimbal simplified non-linear model gain values for negative applied voltages.

Figure 4.16. Inner gimbal simplified non-linear model gain and its fitted gain function for positive applied voltages, (a), and negative applied voltages, (b).

The polynomial functions (4.8) for the inverse gain values are determined with the Matlab fitting tool. The RMS error of the fitment is 0.02494 V/V for the negative applied voltages and 0.02634 V/V for the fitment of the positive applied voltages. Due to the fact that gain values are only determined within a defined range of applied voltages, the inverse gain functions are limited to 0.65 V/V and 0.25 V/V. If the values are not limited, the polynomial functions will cause instability in the system.

$$v_{inv}(u_a) = \begin{cases} -229.5u_a^3 + 254.1u_a^2 - 92.96u_a + 11.49 & u_a > 0.22\ V, \\ 142.5u_a^3 + 163.3u_a^2 + 61.84u_a + 8.03 & u_a < -0.22\ V, \\ 0.65 & |u_a| \leq 0.22\ V, \end{cases} \tag{4.8}$$

and

$$MIN(v_{inv}(u_a)) = 0.25 \tag{4.9a}$$

$$MAX(v_{inv}(u_a)) = 0.65 \tag{4.9b}$$

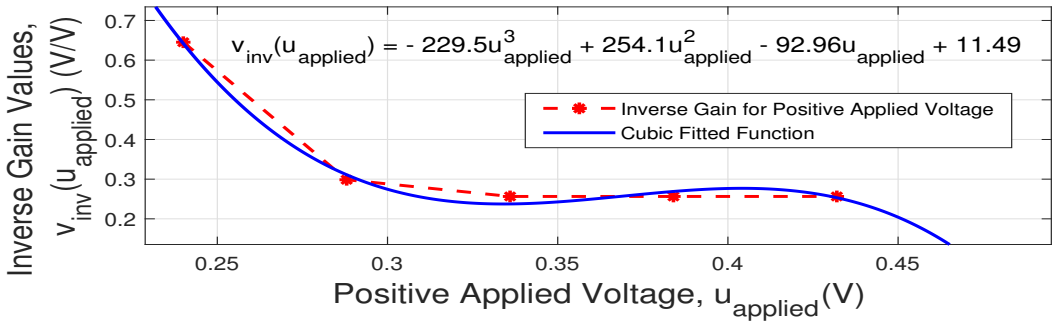

(a) Inner gimbal simplified non-linear model inverse gain values for positive applied voltages.

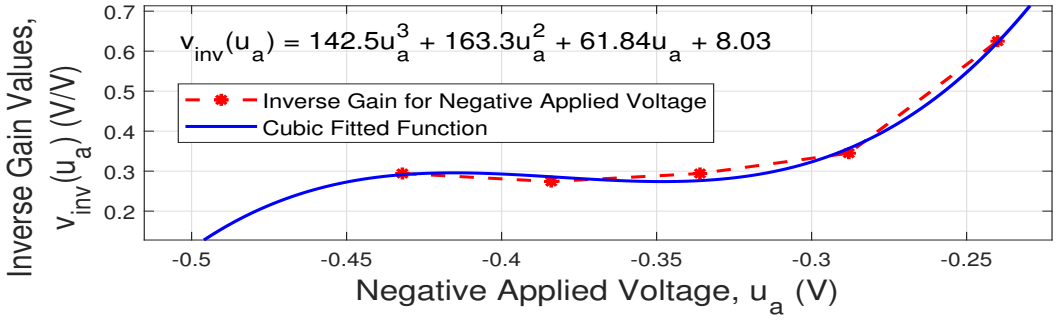

(b) Inner gimbal simplified non-linear model inverse gain values for negative applied voltages.

Figure 4.17. Inner gimbal simplified non-linear model inverse gain and its fitted gain function for positive applied voltages, (a), and negative applied voltages, (b).

The inverse gain function is utilised in the controller shown in (4.10) in the simplified non-linear model with PD control action. The inverse gain function value is determined by the output signal $C(s)$ of the PD controller $C_{PD}(s)$, and will therefore be rewritten as $v_{inv}(C(s))$. It is limited to 0.25 V/V and 0.65 V/V. Integral action is not required as it is already present in the plant. Derivative action reduces deviation from the required set point by acting on the rate of change of the error. This is required as the proportional control with inverse gain function displays a lagging behaviour behind the set point. The added derivative term compensates for this effect. The controller is given with (4.10), and shown in Fig. 4.18.

$$C_{PD}(s) = k_P + \frac{k_D s}{(1/k_N)s+1} \tag{4.10a}$$

$$c(t) = c_{PD}(t)\theta_e(t) \tag{4.10b}$$

$$u_i(s) = c(t)v_{inv}(c(t)) \tag{4.10c}$$

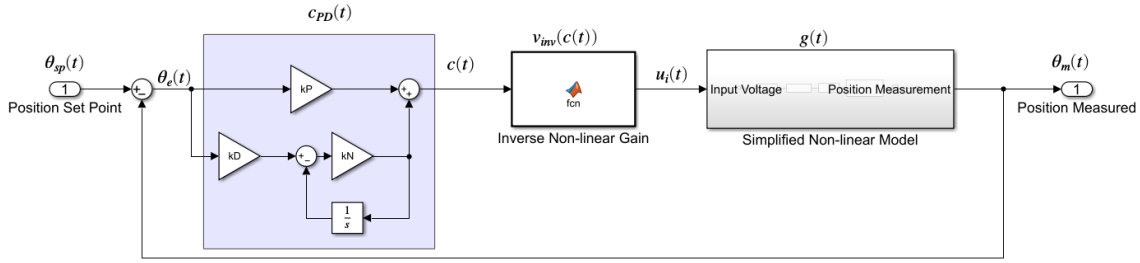

Figure 4.18. Inner gimbal simplified non-linear model with gain scheduling control.

The values of the PD controller are given in Table 4.1. The values are obtained with a tuning process.

Table 4.1. Inner gimbal simplified non-linear model PD controller values.

Variable	Value
k_N	$30\ V/V$
k_D	$12\ V/rad$
k_P	$125\ V/rad$

Fig. 4.19 displays the results of gain scheduling controller (4.10) with a flare trajectory set point (2.9) tested on the simplified non-linear model Fig. 3.10. These results are compared to the results of the linear controller (4.2) on the simplified non-linear model, as developed in Section 4.2.1.

Gain scheduling control (4.10) is implemented on the non-linear model Fig. 3.6. It is implemented with PD controller values indicated in Table 4.2, which are obtained with tuning the respective parameters. The values of the PD controller in Table 4.2, are larger when compared to the simplified non-linear model PD controller values. This corresponds to the linear controller where the proportional gain value P (4.2) is also larger when tuned for the non-linear model than for the simplified non-linear model.

The results of the gain scheduling controller on the inner gimbal non-linear model Fig. 3.6 for a flare trajectory set point (2.9) are compared with the results of the linear controller (4.2) on the non-linear model. It is shown in Fig. 4.20.

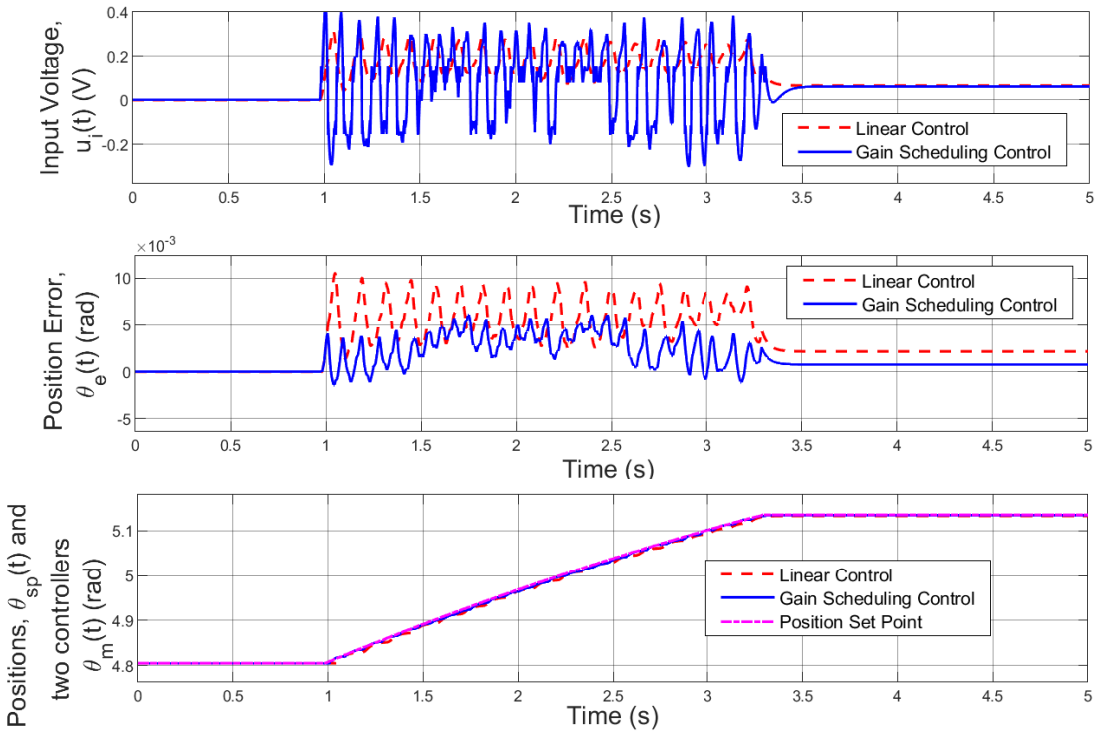

Figure 4.19. Comparison between linear control and gain scheduling control as tested on the inner gimbal simplified non-linear model using a flare trajectory set point.

Table 4.2. PD controller values as tested on the inner gimbal non-linear model.

Variable	Value
k_N	$60\ V/V$
k_D	$16\ V/rad$
k_P	$250\ V/rad$

The gain scheduling controller (4.10) is implemented on the actual gimbal. The PD equation is discretised using Matlab $''c2d''$ function, with the $''tustin''$ option. The gain scheduling action is implemented using (4.8). The PD control values with the best results are listed in Table 4.3. The values were obtained by tuning the parameters. The PD controller function (4.11a) is obtained by simplifying (4.10a), with the values shown in Table 4.3. The high frequency gain is necessary as this is a slow system with a low bandwidth. Big coefficients are required to actuate the gimbals.

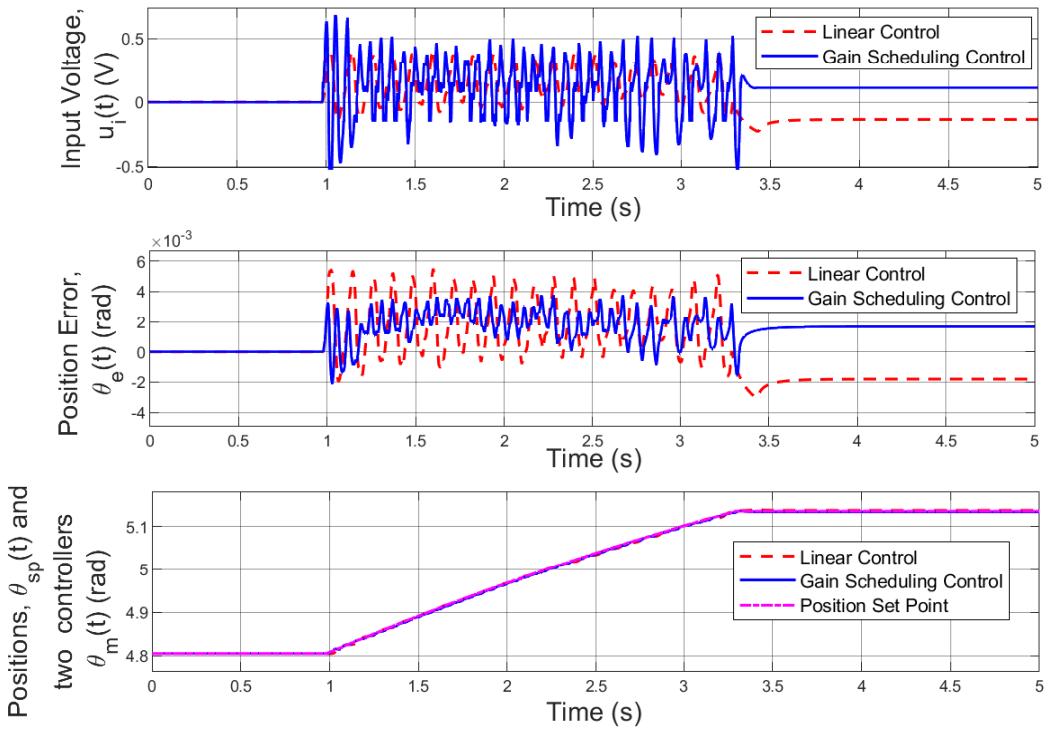

Figure 4.20. Comparison between linear control and gain scheduling control as tested on the inner gimbal non-linear model using a flare trajectory set point.

The discrete PD transfer function from (4.11b) is implemented in the firmware as (4.11c) and is derived from the PD transfer function (4.11a).

Table 4.3. Actual inner gimbal PD controller values.

Variable	Value
k_N	$50\ V/V$
k_D	$4.125\ V/rad$
k_P	$205\ V/rad$

$$C_{PD}(s) = \frac{8.225s + 205}{0.02s + 1} \tag{4.11a}$$

$$C_{PD}[z] = \frac{370 - 288z^{-1}}{1 - 0.6z^{-1}} \tag{4.11b}$$

$$c[k] = 0.6c[k-1] + 370\theta_e[k] - 288\theta_e[k-1] \tag{4.11c}$$

Results of gain scheduling control with PD compensation applied to the inner gimbal is shown in Fig. 4.21 in comparison with the linear control and a flare trajectory set point (2.9).

The mRMS position error, determined with the help of (4.3), for both controllers in Fig. 4.22 shows that the performance of the inner gimbal with gain scheduling is not improved upon significantly. Therefore, the inverse non-linear gain function does not suffice to improve on position control over the linear controller on the inner gimbal. This could possibly be attributed to the smaller size and quicker reaction time of the inner gimbal, which causes the gain scheduling to not have a significant effect on compensating for the non-linear effects such as friction.

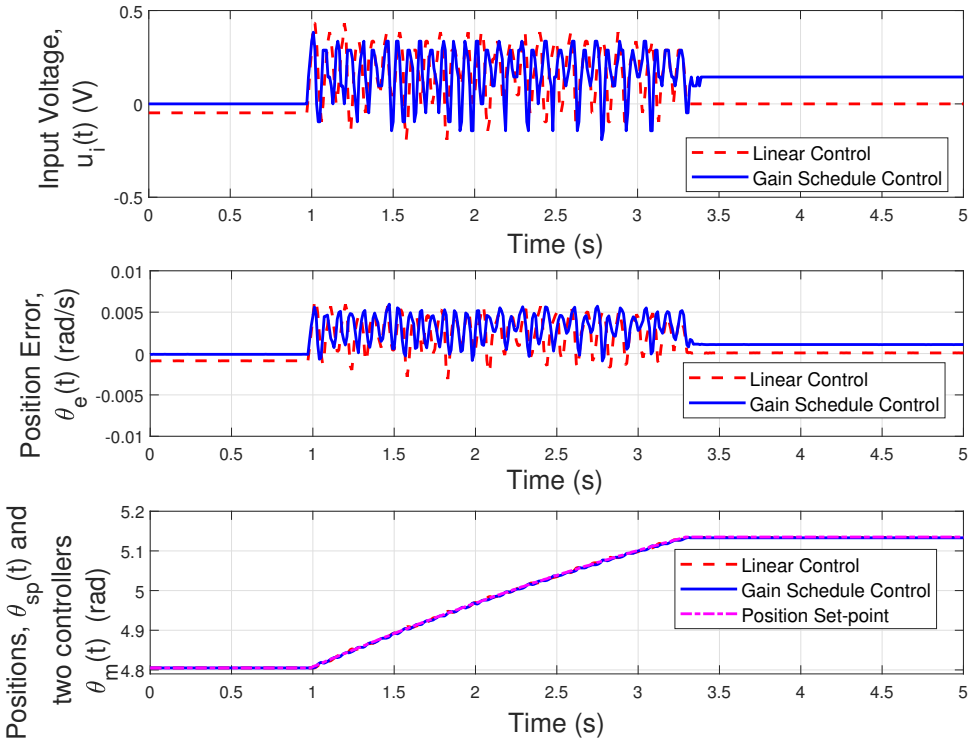

Figure 4.21. Actual inner gimbal with gain scheduling control compared to linear control with a flare trajectory set point.

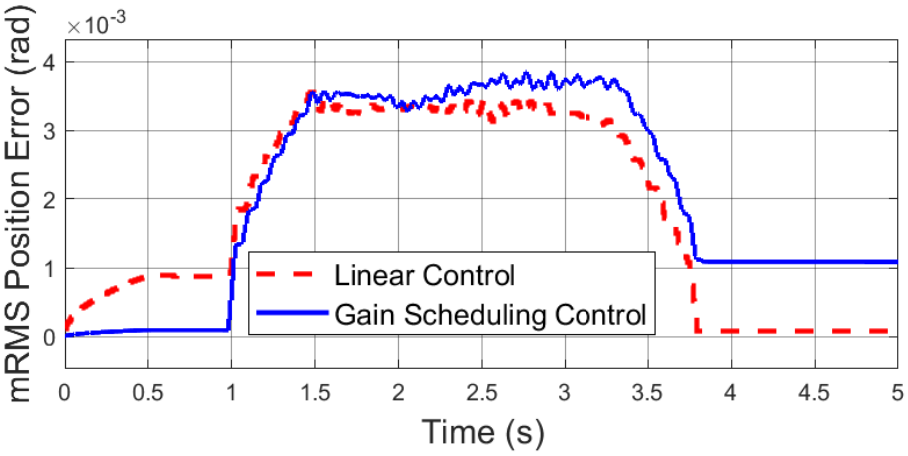

Figure 4.22. Actual inner gimbal mRMS position error values with gain scheduling control compared to linear control using a flare trajectory set point.

4.3.2 Outer gimbal gain scheduling control

The outer gimbal simplified non-linear model Fig. 3.21, repeated with Fig. 4.23 for convenience, contains an input filter and linear plant model, each described with a transfer function. It is identical to the inner gimbal simplified non-linear model.

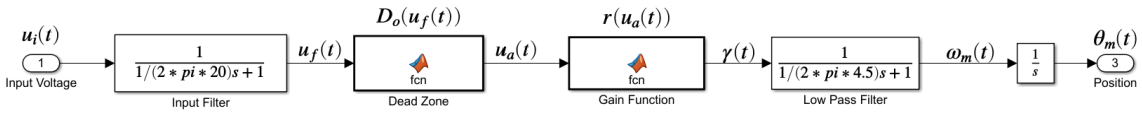

Figure 4.23. Outer gimbal simplified non-linear model.

To apply gain scheduling, the non-linear gain functions are used. The inverse values of the data points in Fig. 3.20 are shown in Fig. 4.24. Polynomial functions (4.12) are derived using Matlab basic plotting tools. Extra data points are added that follows the path of the determined data points. The addition of extra data points improves performance of gain scheduling control on the outer gimbal. However, this does not improve performance of gain scheduling control on the inner gimbal.

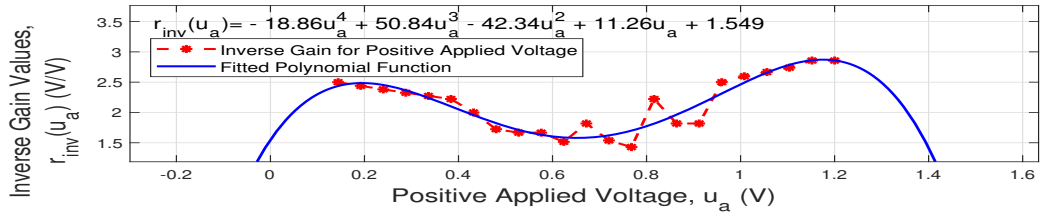

(a) Outer gimbal simplified non-linear model inverse gain values for positive applied voltages.

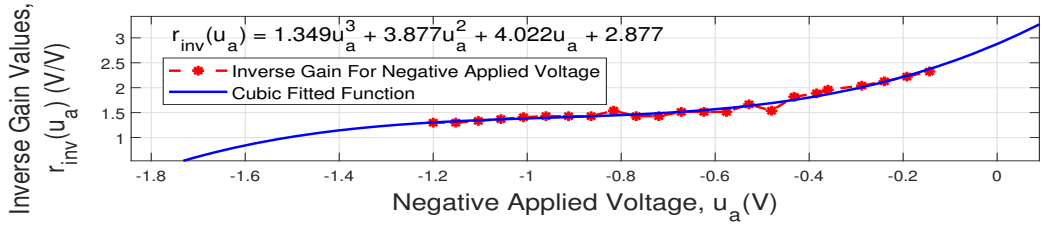

(b) Outer gimbal simplified non-linear model inverse gain values for negative applied voltages.

Figure 4.24. Outer gimbal simplified non-linear model inverse gain and its fitted functions for positive applied voltages, (a), and negative applied voltages, (b).

$$r_{inv}(u_a) = \begin{cases} 1.349u_a^3 + 3.877u_a^2 + 4.022u_a + 2.877 & u_a < 0\ V, \\ 2.5 & u_a = 0\ V, \\ -18.86u_a^4 + 50.84u_a^3 - 42.34u_a^2 + 11.26u_a + 1.549 & \\ & 0\ V < u_a < 1.2\ V, \\ 2.859 & u_a \geq 1.2\ V, \end{cases} \tag{4.12}$$

and

$$MIN(r_{inv}(u_a)) = 1.3 \tag{4.13a}$$

$$MAX(r_{inv}(u_a)) = 2.527 \tag{4.13b}$$

In the case with a negative applied voltage step, the $r_{inv}(u_a)$ function is limited to 1.3 V/V and 2.527 V/V. In the case with a positive applied voltage step between 0 V and 1.2 V, the $r_{inv}(u_a)$ value is limited to 2.5 V/V. The limitations are necessary otherwise the polynomial functions will cause instability. The accuracy of the polynomial equations to the inverse data points are 0.7191 V/V for positive applied voltages and 0.2597 V/V for negative applied voltages.

These functions in (4.12) are applied for gain scheduling control. The gain scheduling controller is given with (4.14) and is shown in Fig. 4.25 on the simplified non-linear model Fig. 3.21.

$$C_{PD}(s) = k_P + \frac{k_D s}{(1/k_N)s+1} \tag{4.14a}$$

$$c(t) = c_{PD}(t)\theta_e(t) \tag{4.14b}$$

$$u_i(t) = c(t)r_{inv}(c(t)) \tag{4.14c}$$

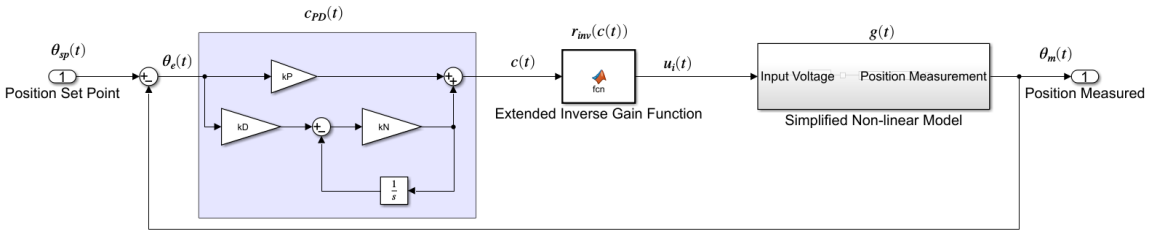

Figure 4.25. Outer gimbal simplified non-linear model with gain scheduling and PD control.

The gain scheduling function with PD control (4.14) is compared with the performance of the linear controller (4.6) on the simplified non-linear model using flare trajectory set point (2.10). The PD controller values are shown in Table 4.4 and are determined with a tuning process. The results in Fig. 4.26 show significant improvement in terms of stability and reduction in error size with the gain scheduling controller.

Table 4.4. Outer gimbal simplified non-linear model PD controller values.

Variable	Value
k_N	$50\ V/V$
k_D	$25\ V/rad$
k_P	$25\ V/rad$

The gain scheduling action with PD compensation (4.14) is tested on the non-linear model Fig. 3.17. Its results are compared with the results of the linear controller (4.6) and is shown in Fig. 4.27. Table 4.5 shows the PD controller values implemented on the non-linear model. The PD controller values are significantly larger than the simplified non-linear model PD controller values. This follows the same trend as the inner gimbal models.

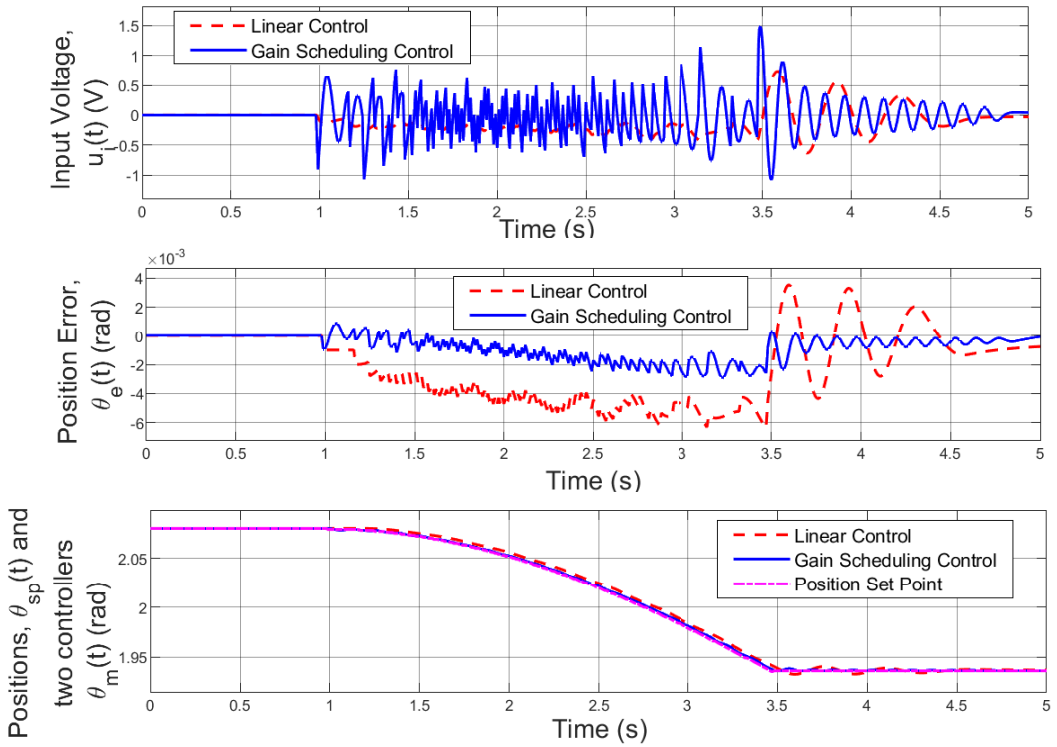

Figure 4.26. Comparison between linear control and gain scheduling control as tested on the outer gimbal simplified non-linear model using a flare trajectory set point.

Table 4.5. Outer gimbal non-linear model PD controller values.

Variable	Value
k_N	$72\ V/V$
k_D	$31.5\ V/rad$
k_P	$175\ V/rad$

The final test is the implementation of the gain scheduling with PD control on the actual gimbal. The PD controller is implemented similarly to the inner gimbal, with values as in Table 4.6. These values are smaller than the non-linear model PD controller values. The difference can be attributed to the non-linear effects present in the system.

The controller transfer function (4.15a) is discretised using Matlab $''c2d''$ function, with the $''tustin''$ option, to arrive at the discrete transfer function (4.15b). It is applied in the firmware using (4.15c).

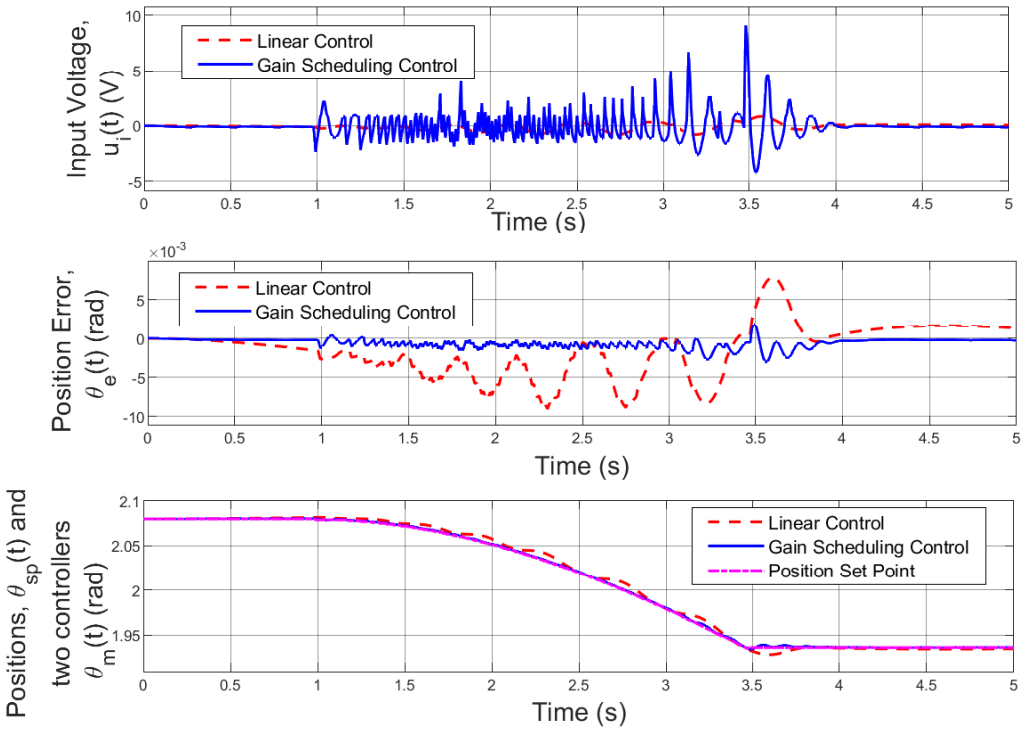

Figure 4.27. Outer gimbal non-linear model with gain scheduling controller and linear controller results.

Table 4.6. Actual outer gimbal PD controller values.

Variable	Value
k_N	$60\ V/V$
k_D	$9\ V/rad$
k_P	$55\ V/rad$

$$C_{PD}(s) = \frac{595s + 3300}{s + 60} \tag{4.15a}$$

$$C_{PD}[z] = \frac{70.4 - 445z^{-1}}{1 - 0.5385z^{-1}} \tag{4.15b}$$

$$c[k] = 0.5385c[k-1] + 70.4\theta_e[k] - 445\theta_e[k-1] \tag{4.15c}$$

The results of the gain scheduling on the actual gimbal is compared with the linear controller in Fig. 4.28.

When the mRMS position error, as determined using (4.3) is compared between the gain scheduling control and linear control, a significant improvement is observed in Fig. 4.29. The gain scheduling control does not achieve the required maximum mRMS position error of 2.00 *m*rad, but decreases from 7.50 *m*rad to 3.45 *m*rad.

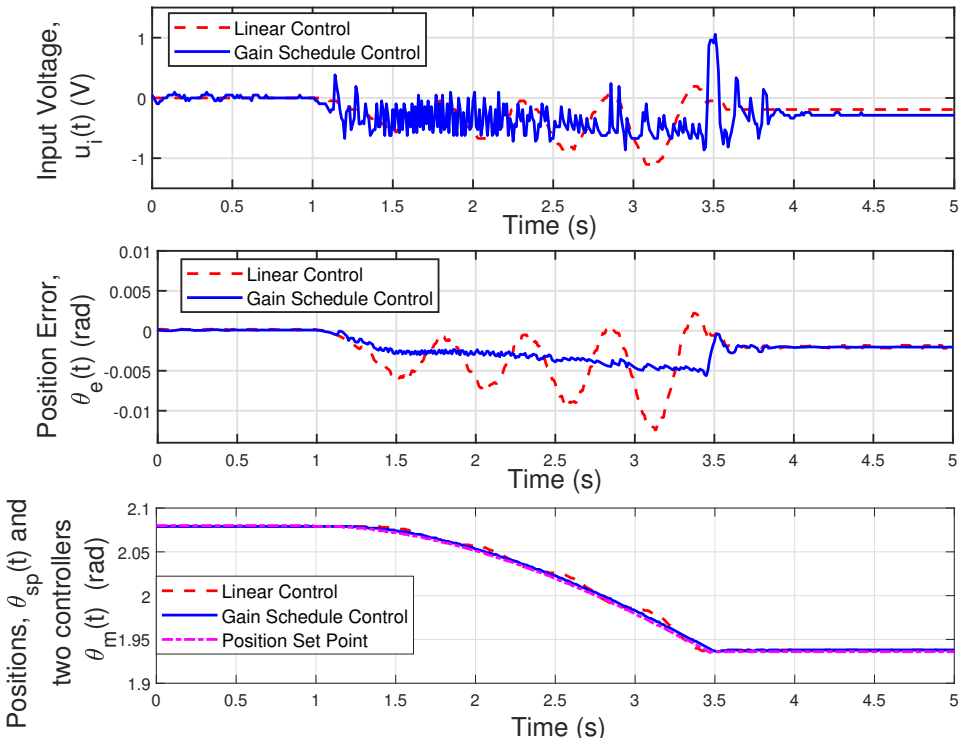

Figure 4.28. Outer gimbal with gain scheduling control compared with the linear controller response.

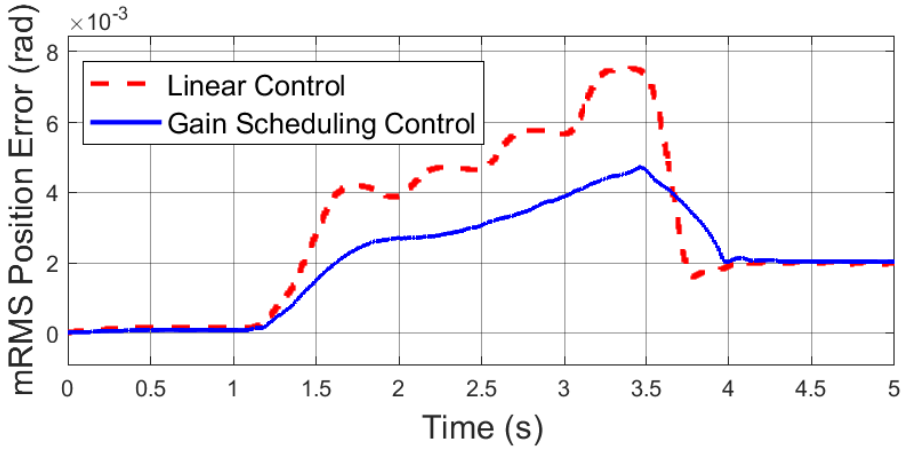

Figure 4.29. Outer gimbal mRMS position error values with gain scheduling control and linear control respectively.

4.4 FINAL CONTROLLER

4.4.1 Inner gimbal final control

Due to the off set in position error exhibited when the flare trajectory motion starts, a feed-forward controller $C_{FF}(s)$ (4.16a) is implemented with PD control $C_{PD}(s)$ (4.16b) as a final controller $C(s)$ (4.16c). The feed-forward control acts to compensate pre-emptively for changes in the set point and can improve precision. Gain scheduling is left out, as it did not improve inner gimbal controller performance.

$$C_{FF}(s) = k_{FF}\frac{s}{s+2\pi 60} \tag{4.16a}$$

$$C_{PD}(s) = k_P + \frac{k_D s}{(1/k_N)s+1} \tag{4.16b}$$

$$E_i(s) = C(s) = C_{FF}(s)\theta_{sp}(s) + C_{PD}(s)\theta_e(s) \tag{4.16c}$$

The final control system (4.17) on the inner gimbal non-linear simulation model Fig. 3.6is implemented as follows.

$$g(t) = \frac{\theta_m(t)}{u_i(t)} \tag{4.17a}$$

$$\theta_m(t) = g(t)(c_{FF}(t)\theta_{sp}(t) + c_{PD}(t)\theta_e(t)) \tag{4.17b}$$

It is presented in Fig. 4.30 and contains a PD controller with feed-forward compensator.

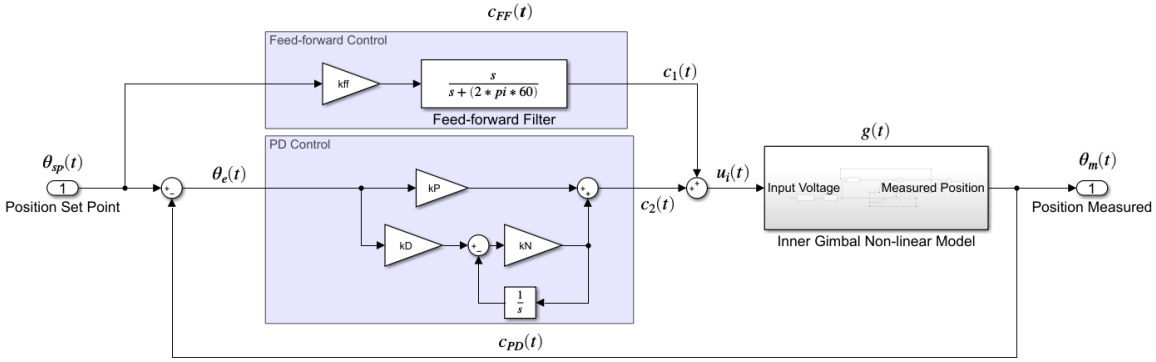

Figure 4.30. Inner gimbal non-linear model with feed-forward and PD compensation.

Table 4.7 contains tuned variables of the PD and feed-forward controller on the non-linear model. The derivative control action is a lot smaller than in the gain scheduling controller. This is possibly due to the pre-emptive effect of feed-forward control. Therefore, the derivative action carries a lot less weight in the controller.

Table 4.7. Inner gimbal non-linear model final controller values.

Variable	Value
k_N	$15\ V/V$
k_D	$0.8\ V/rad$
k_P	$100\ V/rad$
k_{FF}	$300\ V/rad$

Fig. 4.31 compares the results of the final controller to the gain scheduling controller on the non-linear model. The mRMS position error, obtained using (4.3), in Fig. 4.32 displays that the final controller is an improvement over the gain scheduling controller during the initial part of the flare trajectory with the non-linear model. The desired maximum mRMS position error below 2.00 *m*rad is not achieved even though the performance of the final controller shows improvement from the gain scheduling controller during the initial movement of the inner gimbal non-linear model.

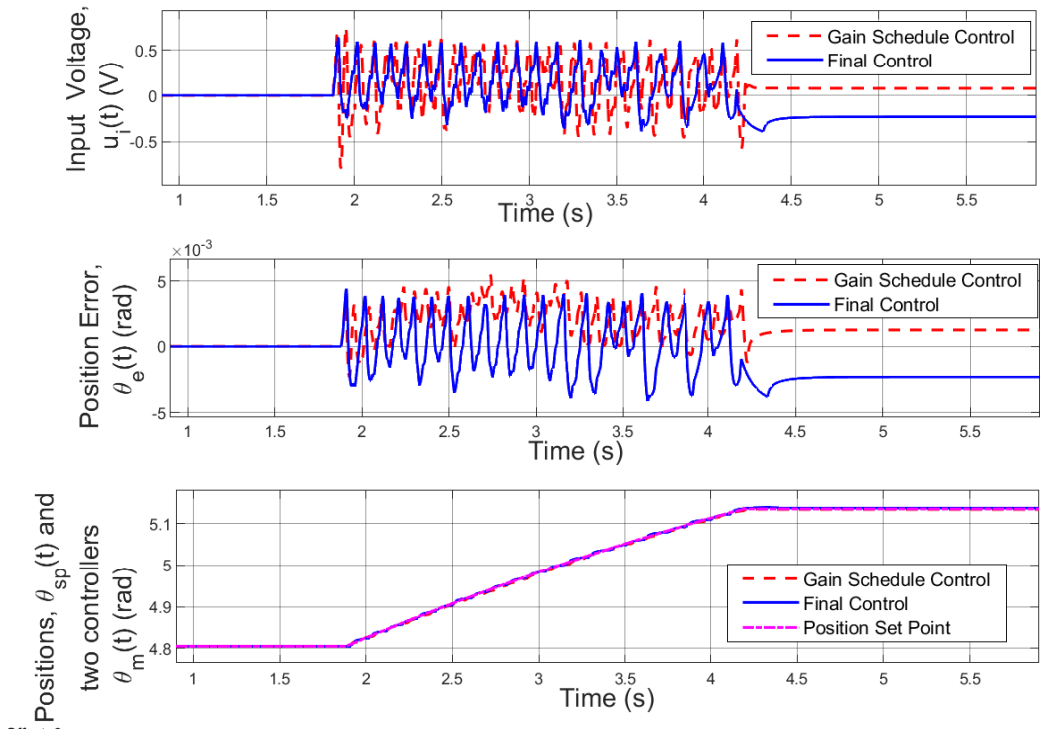

Figure 4.31. Inner gimbal non-linear model with gain scheduling control compared to the final controller for a flare trajectory set point.

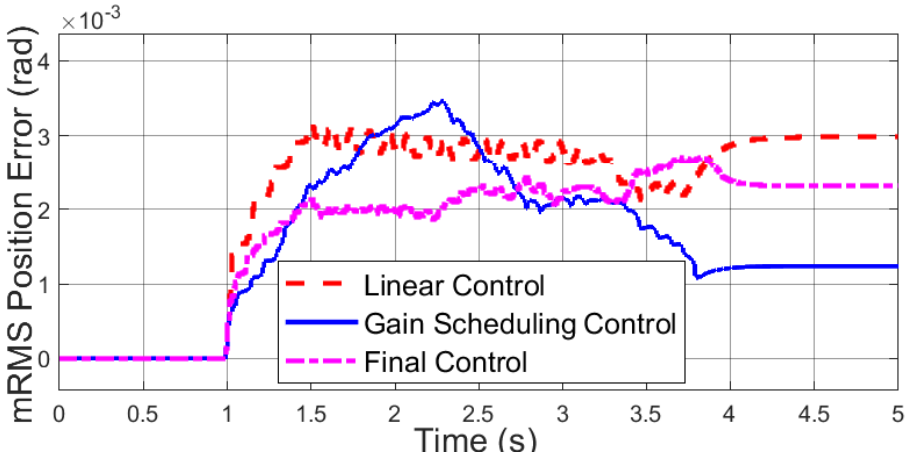

Figure 4.32. Inner gimbal non-linear model mRMS position error values with gain scheduling control compared to the final controller for a flare trajectory set point.

Final controller functionality is implemented on the firmware by discretising (4.16). The table with final PD and feed-forward values that deliver the best results are shown in Table 4.8.

Table 4.8. Inner gimbal final controller values.

Variable	Value
k_N	$10\ V/V$
k_D	$0.2\ V/rad$
k_P	$45\ V/rad$
k_{FF}	$250\ V/rad$

The PD controller is implemented similar to previous PD controllers discussed in the gain scheduling section. The PD controller continuous and discrete transfer functions are given in (4.18).

$$C_{PD}(s) = \frac{4.7s+45}{0.1s+1} \tag{4.18a}$$

$$C_{PD}[z] = \frac{46.9-42.62z^{-1}}{1-0.9048z^{-1}} \tag{4.18b}$$

The feed-forward controller continuous and discrete transfer functions are given in (4.19).

$$C_{FF}(s) = \frac{250s}{s+377} \tag{4.19a}$$

$$C_{FF}[z] = \frac{86.66-86.66z^{-1}}{1+0.3067z^{-1}} \tag{4.19b}$$

The transfer functions of $C_{FF}(s)$ and $C_{PD}(s)$ are discretised using Matlab $''c2d''$ function, with the $''tustin''$ option. They are implemented as two control signals, $c_1[k]$ is the control signal generated with feed-forward control and $c_2[k]$ is the control signal generated with PD control. The code implementation is shown here.

$$c_1[k] = 86.66\theta_{sp}[k] - 86.66\theta_{sp}[k-1] - 0.3067c_1[k-1] \tag{4.20a}$$

$$c_2[k] = 46.9\theta_e[k] - 42.62\theta_e[k-1] + 0.9048c_2[k-1] \tag{4.20b}$$

$$c[k] = c_1[k] + c_2[k] \tag{4.20c}$$

The values of the equations are determined by starting testing with the values obtained during the simulation of the non-linear model. The values are adjusted until best results are obtained. The corner frequency of the feed-forward high pass filter is 60 Hz. This relates to a period of 104.7 *m*s. This implies that the feed-forward controller will act pre-emptively in the first 100 *m*s from when the set point starts changing. Therefore, it compensates for the lagging behaviour of the gimbal corrective action.

The final controller results found on the actual gimbal are compared with the gain scheduled controller results on the actual gimbal, Fig. 4.33. Lastly the mRMS position error values determined with (4.3) are shown for the three controllers, linear, gain scheduling, and the final controller in Fig. 4.34 on the inner gimbal. This graph shows clearly that feed-forward control with PD controller action delivers the smallest mRMS position error. The controller does not achieve the desired accuracy of a maximum mRMS position error below 2.00 *m*rad. It however, decreases to 2.60 *m*rad.

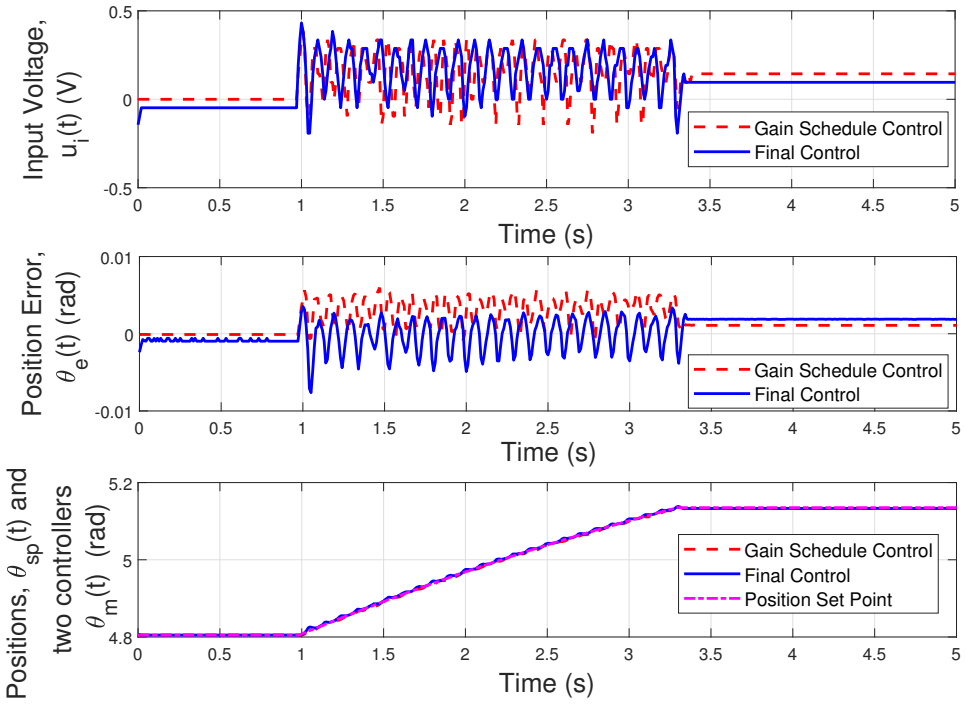

Figure 4.33. Actual inner gimbal results with final controller and gain scheduling controller.

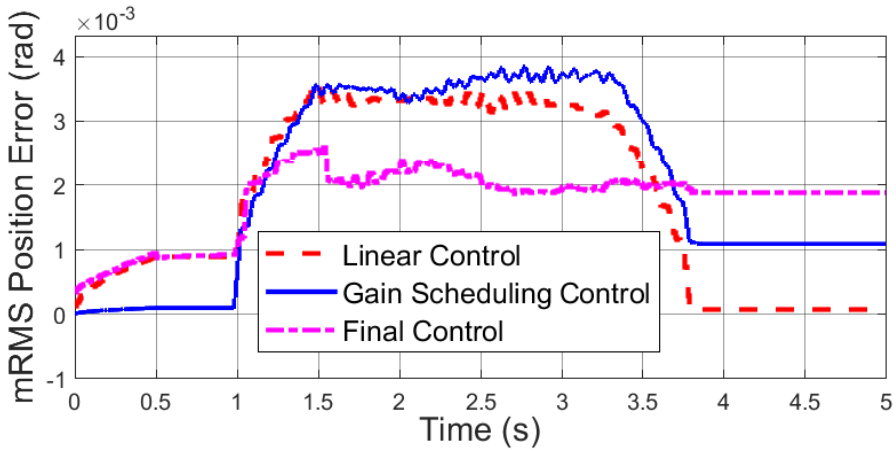

Figure 4.34. Actual inner gimbal mRMS position error values for the three controllers.

4.4.2 Outer gimbal final control

A similar process is followed with the outer gimbal final control as with the inner gimbal final control. Feed-forward control action (4.21b) is added in addition to PD control action (4.21c).

$$c(t) = c_{FF}(t)\theta_{sp}(t) + c_{PD}(t)\theta_e(t) \tag{4.21a}$$

$$C_{FF}(s) = k_{FF}\frac{s}{s+2\pi 10} \tag{4.21b}$$

$$C_{PD}(s) = k_P + \frac{k_D s}{(1/k_N)s+1} \tag{4.21c}$$

However, as the gain scheduling controller (4.12) exhibited superior performance over the linear controller, the gain scheduling control action is kept in the loop of the outer gimbal control system. The controller (4.21a) shown in (4.22) and Fig. 4.35 is implemented on the non-linear model Fig. 3.17.

$$g(t) = \frac{\theta_m(t)}{u_i(t)} \tag{4.22a}$$

$$u_i(t) = c(t)r_{inv}(c(t)) \tag{4.22b}$$

$$\theta_m(t) = g(t)c(t)r_{inv}(c(t)) \tag{4.22c}$$

The feed-forward control values and PD control values are given in Table 4.9. The results of the final controller is compared with the results from gain scheduling control in Fig. 4.36 on the non-linear model. An improvement in position error is observed in the graph.

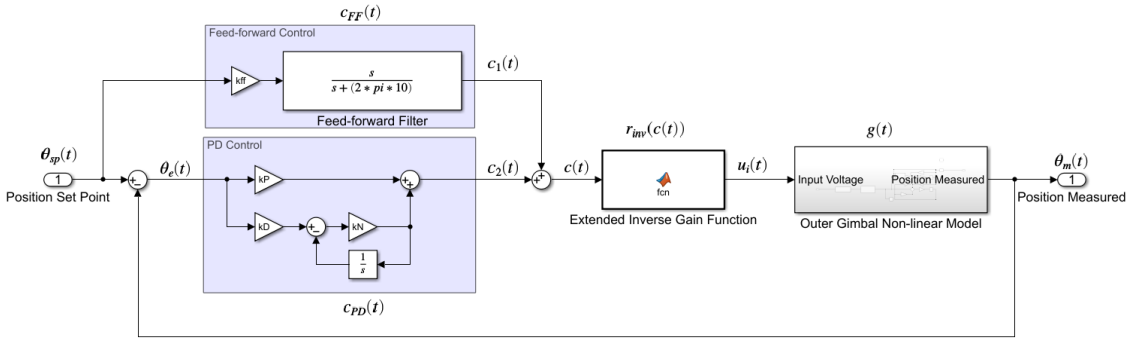

Figure 4.35. Outer gimbal non-linear model final controller.

Table 4.9. Outer gimbal non-linear model final controller values.

Variable	Value
k_N	$72\ V/V$
k_D	$31.5\ V/rad$
k_P	$175\ V/rad$
k_{FF}	$130\ V/rad$

The mRMS position error values are determined using (4.3) for the final controller and compared with the gain scheduling controller as well as linear controller shown in Fig. 4.37 on the outer gimbal non-linear model. It shows that both controllers satisfy the required mRMS position error of less than 2.00 *m*rad, and that the final control is the superior controller in terms of position error.

The outer gimbal final controller is implemented similar to the implementation of the inner gimbal final controller. The exception is that gain scheduling is also implemented as shown in (4.12). The PD and feed-forward control values in Table 4.10 are the values obtained through testing and tuning that delivers best results, in terms of stability and speed.

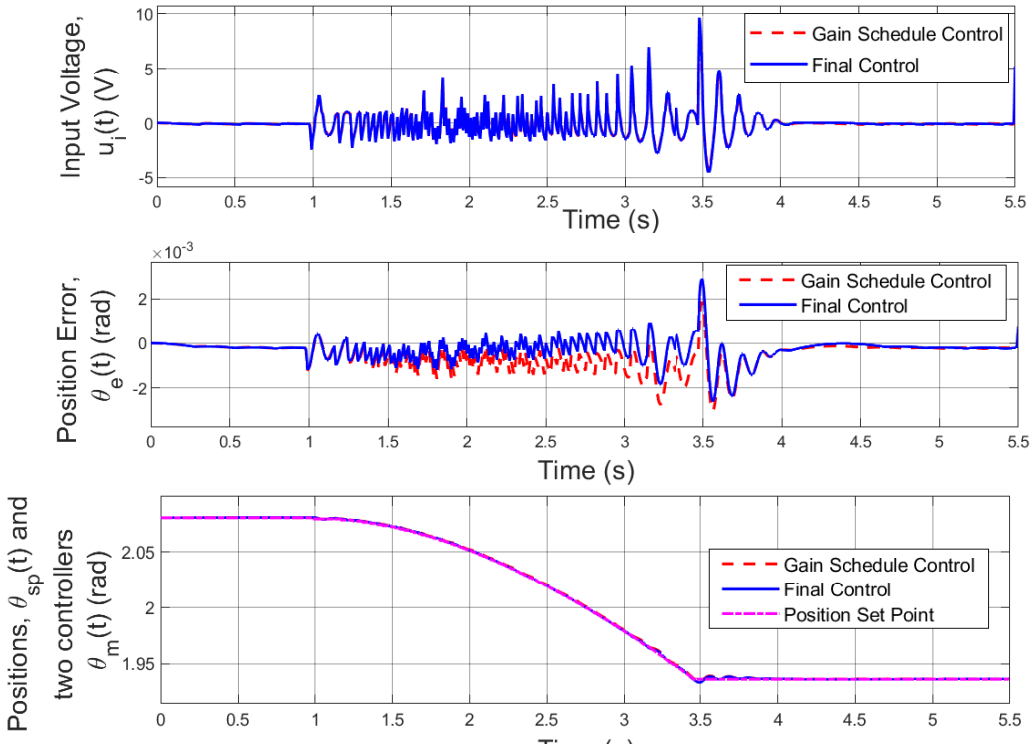

Figure 4.36. Outer gimbal non-linear model results with final controller compared with results from the gain scheduling controller.

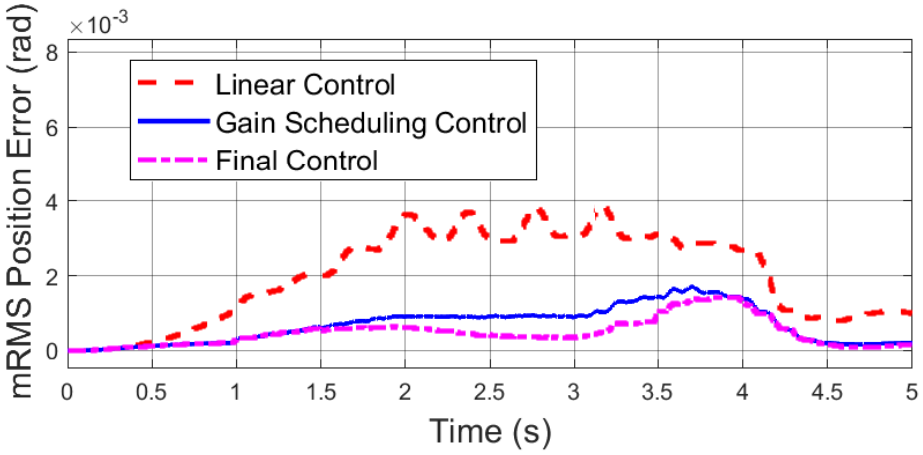

Figure 4.37. Outer gimbal non-linear model mRMS position error values for the three controllers for a flare trajectory set point.

Table 4.10. Actual outer gimbal final controller values.

Variable	Value
k_N	$72\ V/V$
k_D	$9\ V/rad$
k_P	$70\ V/rad$
k_{FF}	$150\ V/rad$

The continuous and discrete functions that describe final PD control action are

$$C_{PD}(s) = \frac{718s + 5040}{s + 72} \tag{4.23a}$$

$$C_{PD}[z] = \frac{546.5 - 509z^{-1}}{1 - 0.4706z^{-1}}. \tag{4.23b}$$

The feed-forward controller transfer functions are

$$C_{FF}(s) = \frac{150s}{s + 62.83} \tag{4.24a}$$

$$C_{FF}[z] = \frac{114.1 - 114.1z^{-1}}{1 + 0.5219z^{-1}}. \tag{4.24b}$$

The discrete functions are implemented on firmware as

$$c_1[k] = 114.1\theta_{sp}[k] - 114.1\theta_{sp}[k-1] - 0.5219c_1[k-1] \tag{4.25a}$$

$$c_2[k] = 546.5\theta_e[k] - 509\theta_e[k-1] + 0.4706c_2[k-1] \tag{4.25b}$$

$$c[k] = c_1[k] + c_2[k] \tag{4.25c}$$

$$u_i[k] = c[k]r_{inv}(c[k]), \tag{4.25d}$$

where $c[k]$ is the sum of the control signals $c_1[k]$ and $c_2[k]$. The results from implementing final control on the actual outer gimbal are compared in Fig. 4.38 with the results from gain scheduling controller.

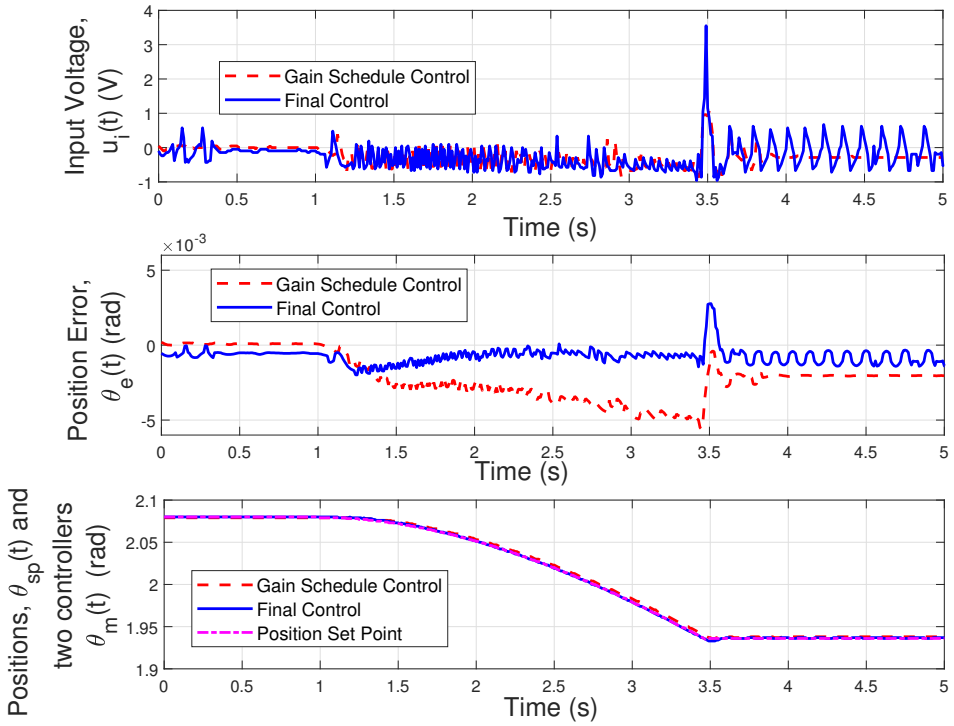

Figure 4.38. Actual outer gimbal results with gain scheduling control and the final controller for a flare trajectory set point.

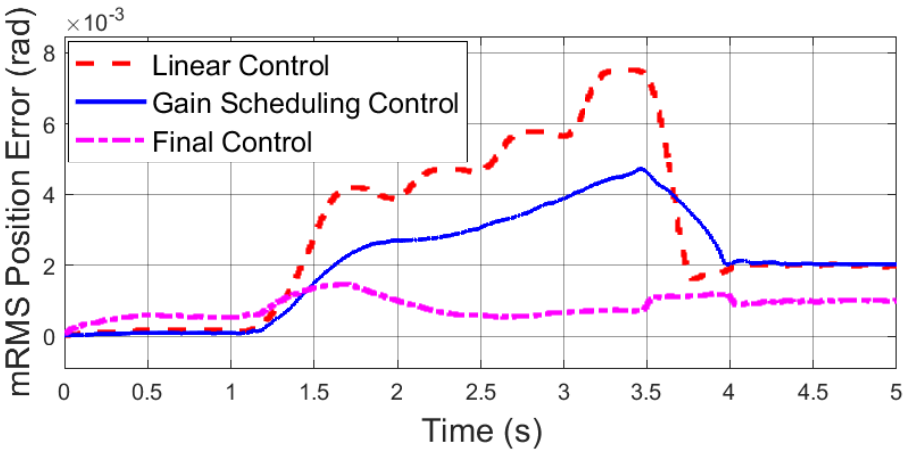

Figure 4.39. Actual outer gimbal mRMS position error for the three controllers with a flare trajectory set point.

The mRMS position error, calculated with (4.3), for all three controllers with a flare trajectory set point are shown in Fig. 4.39. It shows that the final controller performs the best of all the controllers, and that its mRMS position error remains below 2.00 *m*rad.

The control of the outer gimbal is better than the control of the inner gimbal. The inner gimbal final controller uses the same principles, but struggles to meet the requirements during the first stage of trajectory movement.

4.5 RESULTS

The results from the final controllers on both gimbals are converted back into real world parameters to show what the flare trajectory will look like on the HILS platform. Conversion happens in reverse from Section 2.4.2 where the mathematical model results are converted into gimbal units. A comparison between the inner gimbal result and horizontal flare path (2.9) shown in Fig. 4.40 shows that the inner gimbal emulates flare trajectory accurately and is stable for the horizontal flare path (2.7a). Fig.4.40(a) shows the results from the actual gimbal compared to the set point in gimbal units, where Fig. 4.40(b) shows the gimbal results converted to real world parameters and compared against the real world mathematical model.

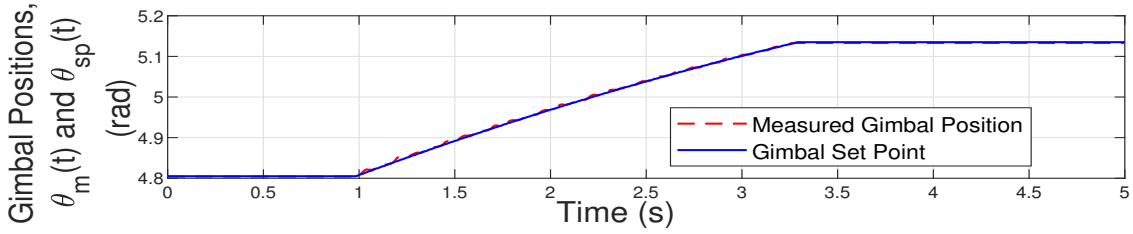

(a) Measured position on the inner gimbal with the firmware position set point.

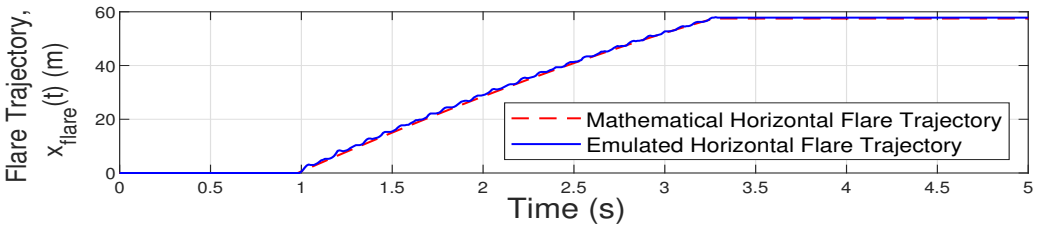

(b) Measured position on the inner gimbal scaled to a flare trajectory with the horizontal mathematical flare trajectory.

Figure 4.40. Horizontal flare trajectory final results from inner gimbal measurements, (a), scaled to the real world, (b).

Similarly Fig. 4.41 shows that the outer gimbal imitates vertical flare trajectory (2.10) relatively accurately when compared with the results from the mathematical model (2.7b). Fig.4.41(a) shows the

results from the actual gimbal compared to the set point in gimbal units, where Fig. 4.41(b) shows the gimbal results converted to real world parameters and compared against the real world mathematical model.

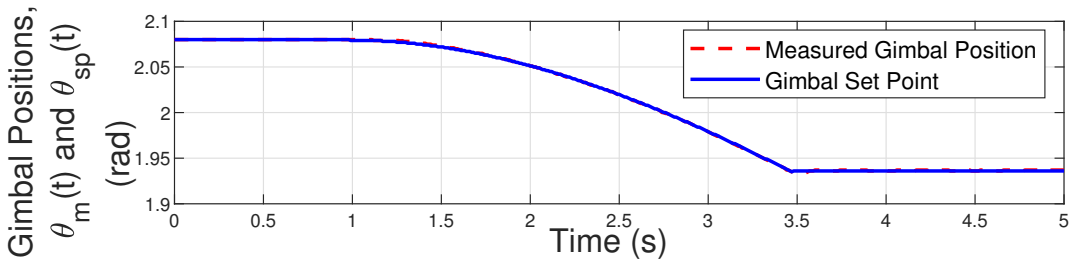

(a) Measured position on the outer gimbal with the firmware position set point.

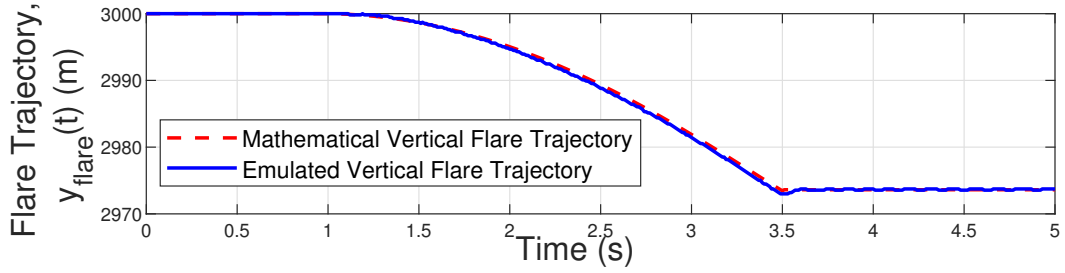

(b) Measured position on the outer gimbal scaled to a flare trajectory with the vertical mathematical flare trajectory.

Figure 4.41. Vertical flare trajectory final results from outer gimbal measurements, (a), scaled to the real world, (b).

Horizontal and vertical real world flight paths are shown together in Fig. 4.42. The results from the gimbal simulation are shown with results from the mathematical study. The fit of the emulated flare trajectory onto the horizontal and vertical flare paths is 95.60 %.

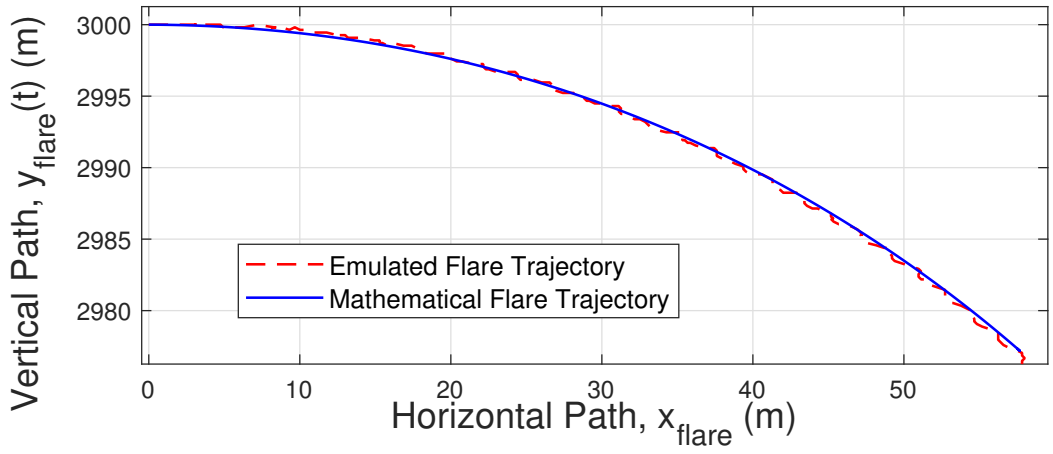

Figure 4.42. Emulated flare trajectory generated with the gimbals shown with flare trajectory from the mathematical model.

4.6 CONCLUSION

The inner gimbal is smaller and reacts quicker than the outer gimbal. It requires a less complex linear controller, and proportional control is sufficient. The outer gimbal requires a more complex linear controller as it is bigger and slower. It is also more sensitive to non-linear effects introduced by wires attached to it. Linear control for each gimbal is developed using Matlab tools. The linear control results on the actual gimbals are not satisfactory for both gimbals.

Gain scheduling is introduced in order to compensate for non-linearities as parametrised with the simplified non-linear model. From the results it is apparent that gain scheduling does not significantly improve the control of the inner gimbal, but does improve results on the outer gimbal. This is probably due to the fact that the inner gimbal requires smaller voltages for actuation and the non-linear effects are larger such as when the system operates using smaller voltages. Therefore gain scheduling does not compensate properly for non-linear elements in the system. On the other hand, the outer gimbal requires larger actuation voltages, and therefore enough energy is present in the system to overcome non-linear effects that are compensated for with gain scheduling.

Lastly, a final controller is developed for each gimbal. For the inner gimbal this controller consists of PD control and a feed-forward compensator. The addition of the feed-forward compensator allows the gimbal to compensate quicker when the set point starts changing. The final controller for the outer gimbal is a PD controller with feed-forward action and gain scheduling. The control of the outer gimbal is more accurate than the control of the inner gimbal.

Table 4.11 summarises the maximum mRMS position error values determined with (4.3) generated with the inner gimbal for the different controllers. Table 4.12 summarises the maximum mRMS position errors generated with the outer gimbal for the different controllers.

Table 4.11. Inner gimbal controller evaluation with the mRMS position error results.

Model	Maximum mRMS position error
Linear control	3.50 *m*rad
Gain scheduling control	3.80 *m*rad
Final control	2.60 *m*rad

Table 4.12. Outer gimbal controller evaluation with the mRMS position error results.

Model	Maximum mRMS position error
Linear control	7.50 *m*rad
Gain scheduling control	4.70 *m*rad
Final control	1.47 *m*rad

CHAPTER 5 CONCLUSION

For this study a mathematical flare model is developed for hardware implementation on a HILS platform. The flare model is converted into a position set point in two dimensions, the horizontal and vertical directions of movement of the flare. Two gimbals are actuated with dc motors, and the goal of the study is to emulate flare trajectory with these two gimbals as accurately as possible.

The first step of the study is the investigation of flare dynamic models. A position set point in terms of flare trajectory is developed from the models. Using fitting and scaling functions, the flare trajectory is converted for utilisation on the two gimbals in a target motion simulation system. The second step is modelling of the two gimbals with the aim of developing a controller for flare trajectory emulation. There are non-linear elements present in both gimbals. The inner gimbal portrays horizontal movement and is mounted on the inside of the outer gimbal which portrays vertical movement. The inner gimbal actuation is affected in a non-linear way with friction, partly due to its small operating range and the small actuation voltage required to move it. It is the smaller gimbal of the two and responds quicker to input voltage signals. The outer gimbal is bigger and reacts slower than the inner gimbal. Non-linear elements in the outer gimbal is attributed to a wire harness connected to it that are associated with the inner gimbal, as well as friction properties present in the dc motor.

An accurate non-linear model is developed for both gimbals. The average fit for the inner gimbal non-linear simulation model is 94.17 %, and 94.06 % for the outer gimbal. The models are reduced to a simplified non-linear model which contains a non-linear gain function in order to simulate the non-linear elements affecting movement of the gimbals. The average fit for the inner gimbal simplified non-linear simulation model is 91.86 %, and 83.75 % for the outer gimbal. The simplified non-linear models display reduced accuracy when compared with actual gimbals, as can be expected.

Lastly, linear models are deduced from the simplified non-linear models. The non-linear gain function is reduced to a single gain which is derived from the average of the gain values in the simplified non-linear model. The average fit for the inner gimbal linear simulation model is 48.09 %, and 72.48 % for the outer gimbal.

There are three different controller developments. The first controller design was developed on the linear model. The linear controller provides the least satisfactory results of the three controllers. Its maximum mRMS position error is 3.50 *m*rad on the inner gimbal and 7.50 *m*rad on the outer gimbal. The second controller was developed with the simplified non-linear model, and employs gain scheduling as method to compensate for non-linear effects in the gimbals. For the outer gimbal, gain scheduling shows improvement over linear control. For the inner gimbal, gain scheduling did not show any benefit. This could be attributed to the short range with which gain values are determined for functions on the inner gimbal as well as the low actuation voltages utilised on the inner gimbal. The outer gimbal model can employ a larger range of input voltage values. An extended gain scheduling function is employed on the outer gimbal with success. The gain scheduling controller maximum mRMS position error is 3.80 *m*rad on the inner gimbal and 4.70 *m*rad on the outer gimbal.

The last controller adds feed-forward control to a version of one of the two previous controllers. For the inner gimbal, feed-forward control is added with PD compensation. For the outer gimbal feed-forward control is added to PD compensation with the gain scheduling function. This provides the best results of all the controllers, and performs better than the inner gimbal controller. The final controller maximum mRMS position error is 2.60 *m*rad on the inner gimbal and 1.47 *m*rad on the outer gimbal.

Even though the maximum mRMS position error exceeds the preferred specification of 2.00 *m*rad on the inner gimbal, it is deemed as acceptable in as such that the flare trajectory set point is followed on the HILS platform. When the mRMS position error is less than 2.00 *m*rad, it means that in real world the error is always less than 0.377 m, which implies an error of less than 0.6 %. When the maximum error increases to 2.60 *m*rad, it implies that on a real-world scale the maximum error is 0.488 m. This result implies an error of less than 0.8 %. This is deemed as acceptable in terms of the flare trajectory simulation on the HILS platform.

This study contributes to the control environment by detailing the system identification process in order to develop a suitable controller for a gimbal actuated with a dc motor. It analyses methods for

controlling hardware with portions of non-linear elements which influences its operation.

It allows implementation of a mathematical model on hardware in order to provide additional capability for countermeasures evaluations. It contributes to the HILS environment with development of a flare trajectory. This give the HILS platform the ability to evaluate the counter-countermeasures of its missiles.

Although a single flare trajectory result is shown in this study, it has the ability to showcase more flare ejection scenarios by following the same procedure as outlined in the modelling section. For future work more flare trajectories can be implemented and evaluated on the hardware.

REFERENCES

Ahmed, A., Mohan, Y., Chauhan, A. and Sharma, P. (2013). Comparative study of speed control of dc motor using PI, IP, and fuzzy controller, *International Journal of Advanced Research in Computer and Communication Engineering* **2**(7): 2693–2697.

Al-Jarrah, M. and Hasan, M. (2011). HILS setup of dynamic flight path planning in 3D environment with flexible mission planning using Ground Station, *Journal of the Franklin Institute* **348**(1): 45–65.

Azarmi, R., Tavakoli-Kakhki, M., Sedigh, A. K. and Fatehi, A. (2016). Robust fractional order PI controller tuning based on Bode's ideal transfer function, *IFAC-PapersOnLine* **49**(9): 158–163.

Bacic, M. (2005). On hardware-in-the-loop simulation, *Proceedings of the 44th IEEE Conference on Decision and Control, 15 December 2005, Seville, Spain*, pp. 3194–3198.

Bai, R. (2015). Neural network control-based adaptive design for a class of dc motor systems with the full state constraints, *Neurocomputing* **168**: 65–69.

Baqar, S. (2008). *Low-cost PC-based high-fidelity infrared signature modelling and simulation*, Master's thesis, Cranfield University.

Beltran-Carbajal, F., Favela-Contreras, A., Valderrabano-Gonzalez, A. and Rosas-Caro, J. C. (2014). Output feedback control for robust tracking of position trajectories for dc electric motors, *Electric Power Systems Research* **107**: 183–189.

Beltran-Carbajal, F., Valderrabano-Gonzalez, A. and Rosas-Caro, J. C. (2015a). Signal differentiation in position tracking control of dc motors, *Journal of Physics: Conference Series*, Vol. 582, IOP Publishing, pp. 1–8.

Beltran-Carbajal, F., Valderrabano-Gonzalez, A., Rosas-Caro, J. and Favela-Contreras, A. (2015b). An asymptotic differentiation approach of signals in velocity tracking control of dc motors, *Electric Power Systems Research* **122**: 218–223.

Ben-David, E. and Cabib, D. (1992). IR simulation of missile closing on a moving textured object with a textured background and EO countermeasure, *in* D. Clement and W. R. Watkins (eds), *Characterization, Propagation, and Simulation of Sources and Backgrounds II, 21 September 1992*, Vol. 1687, International Society for Optics and Photonics, pp. 509–521.

Bett, C. J. (2004). *The Electrical Engineering Handbook*, Elsevier Academic Press, chapter Gain-scheduled controllers, pp. 1107–1114.

Bhatti, S. A., Daraz, A. and Malik, S. A. (2016). Comparison of P-I and I-P controller by using Ziegler-Nichols tuning method for speed control of dc motor, *2016 International Conference on Intelligent Systems Engineering (ICISE), 15-17 January 2017, Islamabad, Pakistan*, IEEE, pp. 330–334.

Bingtao, G., Xiaorui, W., Yujiao, C., Zhaohui, L. and Jianlei, Z. (2015). High-accuracy infrared simulation model based on establishing the linear relationship between the outputs of different infrared imaging systems, *Infrared Physics & Technology* **69**: 155–163.

Bouscayrol, A. (2008). Different types of hardware-in-the-loop simulation for electric drives, *2008 IEEE International Symposium on Industrial Electronics, 30 June - 2 July 2008, Cambridge, UK*, IEEE, pp. 2146–2151.

Buccella, C., Cecati, C. and Latafat, H. (2012). Digital control of power converters—A survey, *IEEE Transactions on Industrial Informatics* **8**(3): 437–447.

Bullock, D., Johnson, B., Wells, R. B., Kyte, M. and Li, Z. (2004). Hardware-in-the-loop simulation, *Transportation Research Part C: Emerging Technologies* **12**(1): 73–89.

Carter, J. M. and Willis, K. E. (1998). History of flight motion simulators used for hardware-in-the-loop testing of missile systems, *Technologies for Synthetic Environments: Hardware-in-the-Loop Testing III*, Vol. 3368, International Society for Optics and Photonics, pp. 425–431.

Chemring (2017). MTV-Flare CM 118 Mk3 Type 1. https://www.chemring.co.uk/what-we-do/countermeasures-and-energetics/conventional-flares/uk/mtv-flare-cm-118-mk3-type-1. Last accessed on 13 November 2020.

Chen, C., Rai, S. and Tsao, T. (2019). Iterative learning of dynamic inverse filters for feedforward tracking control, *IEEE/ASME Transactions on Mechatronics* **25**(1): 349–359.

CMM Optic (2021). CMM Optic Two Axis Gimbal. https://www.cmmoptic.com/two-axis-gimbal/. Last accessed on 5 September 2021.

Cole Jr., J. S. and Jolly, A. C. (1996). Hardware-in-the-loop simulation at the U.S. Army Missile Command, *Technologies for Synthetic Environments: Hardware-in-the-Loop Testing, 24 May 1996, Orlando, FL, USA*, Vol. 2741 of *Aerospace/Defense Sensing and Controls*, International Society for Optics and Photonics, pp. 14–19.

Corpino, S. and Stesina, F. (2014). Verification of a CubeSat via hardware-in-the-loop simulation, *IEEE Transactions on Aerospace and Electronic Systems,* **50(4)**(4): pp. 2807–2818.

Courtney, R. A. and Huber Jr., E. G. (1997). Now-term solutions to spatial, spectral, and temporal IR simulation with Wright Laboratory's Dynamic Infrared Missile Evaluator (DIME), *Technologies for Synthetic Environments: Hardware-in-the-Loop Testing II, 15 July 1997, Orlando, FL, USA*, Vol. 3084 of *AeroSense 1997*, International Society for Optics and Photonics, pp. 104 – 110.

de Carvalho, D. F., Ganzaroli, C. A., do Couto, L. A., Dias, R. N. H. M. and Calixto, W. P. (2017). Hybrid optimization process applied to tuning of dynamic matrix control: Study case with dc motor, *Transactions on Environment and Electrical Engineering* **2**(2): 24–30.

DiMarco, J. S., Kemper Jr., P. J. and Pringle, L. N. (1999). Closed-loop guidance of imaging infrared missile seekers, *Infrared Imaging Systems: Design, Analysis, Modeling, and Testing X, 12 July 1999, Orlando, FL, USA*, Vol. 3701 of *AeroSense 1999*, International Society for Optics and Photonics, pp. 254–265.

Dixit, V., Xu, Z., Wang, M., Zhang, F., Jin, S., Zhang, J. and Zhao, X. (2017). PaTAVTT: A hardware-in-the-loop scaled platform for testing autonomous vehicle trajectory tracking, *Journal of Advanced Transportation* **2017**(1): 1–12.

Edwards, C. and Penney, D. (2000). *Elementary Differential Equations with Boundary Value Problems*, Prentice Hall.

El-Nagar, A. M. (2016). Embedded intelligent adaptive PI controller for an electromechanical system, *ISA Transactions* **64**: 314–327.

Ganzaroli, C. A., de Carvalho, D. F., Dias, R. N. H. M., Reis, M. R. C., Alves, A. J., Domingos, J. L. and Calixto, W. P. (2015). Heuristic and deterministic strategies applied on cascade PI controller tuning for speed control of a dc motor, *2015 CHILEAN Conference on Electrical, Electronics Engineering, Information and Communication Technologies (CHILECON), 28 - 30 October 2015, Santiago, Chile*, IEEE, pp. 101–106.

Golnaraghi, F. and Kuo, B. C. (2003). *Automatic Control Systems*, Eight edn, John Wiley & Sons.

Gross, S. (1999). BGT hardware-in-the-loop simulation facility, *Technologies for Synthetic Environments: Hardware-in-the-Loop Testing IV, 19 July 1999, Orlando, FL, USA*, Vol. 3697 of *AeroSense 1999*, International Society for Optics and Photonics, pp. 2–10.

Hunter, M. P., Roe, M. and Wu, S. K. (2010). Hardware-in-the-loop simulation evaluation of adaptive signal control, *Transportation Research Record* **2192**(1): 167–176.

Imen, S. J. and Shakeri, M. (2007). Feed forward adaptive control of a linear brushless dc motor, *SICE Annual Conference 2007, 17 - 20 September 2007, Takamatsu, Japan*, IEEE, pp. 2200–2204.

Jackman, J. (2012). *Pre-emptive infrared countermeasures*, PhD thesis, Cranfield University.

Kanojiya, R. G. and Meshram, P. M. (2012). Optimal tuning of PI controller for speed control of dc motor drive using particle swarm optimization, *2012 International Conference on Advances in Power Conversion and Energy Technologies (APCET), 2 - 4 August 2012, Mylavaram, India*, IEEE, pp. 1–6.

Kaya, İ. and Nalbantoğlu, M. (2016). Simultaneous tuning of cascaded controller design using genetic algorithm, *Electrical Engineering* **98**(3): 299–305.

Khan, H. S. and Kadri, M. B. (2013). DC motor speed control by embedded PI controller with hardware-in-loop simulation, *2013 3rd IEEE International Conference on Computer, Control and Communication (IC4), 25 - 26 September 2013, Karachi, Pakistan*, IEEE, pp. 1–4.

Koch, E. (2006). Pyrotechnic countermeasures: II. Advanced aerial infrared countermeasures, *Propellants, Explosives, Pyrotechnics: An International Journal Dealing with Scientific and Technological Aspects of Energetic Materials* **31**(1): 3–19.

Labonté, G. and Deck, W. C. (2010). Infrared target-flare discrimination using a ZISC hardware neural network, *Journal of Real-Time Image Processing* **5**(1): 11–32.

Li, N., Hua, W., Wang, S. and Ren, L. (2016). A real-time infrared imaging simulation method with physical effects modeling of infrared sensors, *Infrared Physics & Technology* **78**: 45–57.

Li, Z., Kyte, M. and Johnson, B. (2004). Hardware-in-the-loop real-time simulation interface software design, *Proceedings. The 7th International IEEE Conference on Intelligent Transportation Systems (IEEE Cat. No.04TH8749), 3 - 6 October 2004, Washington, WA, USA*, IEEE, pp. 1012–1017.

Lin, C.-F., Tseng, C.-Y. and Tseng, T.-W. (2006). A hardware-in-the-loop dynamics simulator for motorcycle rapid controller prototyping, *Control Engineering Practice* **14**(12): 1467–1476.

Mathworks (R2020b). Matlab simulink.

Mehendale, C. S. and Grigoriadis, K. M. (2004). A new approach to LPV gain-scheduling design and implementation, *2004 43rd IEEE Conference on Decision and Control (CDC)(IEEE Cat. No. 04CH37601), 14 - 17 December 2014, Nassau, Bahamas*, Vol. 3, IEEE, pp. 2942–2947.

Morales, R., Somolinos, J. and Sira-Ramírez, H. (2014). Control of a DC motor using algebraic derivative estimation with real time experiments, *Measurement* **47**: 401–417.

Morin, A. and Lessard, P. (1999). Development of an infrared imaging seeker emulator for counter-measure studies, *in* M. K. Masten and L. A. Stockum (eds), *Acquisition, Tracking, and Pointing XIII*, Vol. 3692, International Society for Optics and Photonics, pp. 255–268.

Mudau, A., Willers, C., Hlakola, M., le Roux, F., Theron, B., Calitz, J. and Plooy, M. D. (2011). Optronic measurement, testing and the need for valid results: Example of infrared measurements for defence countermeasures, *NCSLI Measure* **6**(2): 42–49.

Newport (2021). Motorized Gimbal Mounts. https://www.newport.com/s/motorized-gimbal-mounts. Last accessed on 5 September 2021.

Nissimagoudar, P., Mane, V., Gireesha, H. and Iyer, N. C. (2020). Hardware-in-the-loop (HIL) simulation technique for an automotive electronics course, *Procedia Computer Science* **172**: 1047–1052.

Noda, Y., Tsujita, T., Abiko, S., Sato, D. and Nenchev, D. N. (2020). HILS using a minimum number of joint module testbeds for analyzing a multi-DoF manipulator, *2020 IEEE/ASME International Conference on Advanced Intelligent Mechatronics (AIM), 6 - 9 July 2020, Boston, MA, USA*, IEEE, pp. 1772–1779.

Olsson, H., Astrom, K. J., de Wit, C. C., Gefvert, M. and Lischinsky, P. (1998). Friction models and friction compensation, *European Journal of Control* **4**(3): 176–195.

Onawola, H. J., Adewunmi, O. T., Ehiagwina, F. O. and Iromini, N. A. (2017). Analytical description of dc motor with determination of rotor damping constant (B) of 12V dc motor, *The International Journal of Engineering and Science (IJES)* **6**(6): 37–42.

Pathak, K. B. and Adhyaru, D. M. (2016). MRAC based dc servo motor motion control, *International Journal of Advanced Research in Engineering and Technology (IJARET)* **7**(2): 53–63.

Pennestri, E., Rossi, V., Salvini, P. and Valentini, P. P. (2016). Review and comparison of dry friction force models, *Nonlinear dynamics* **83**(4): 1785–1801.

Polasek, M., Nemecek, J. and Pham, I. Q. (2016). Counter countermeasure method for missile's imaging infrared seeker, *2016 IEEE/AIAA 35th Digital Avionics Systems Conference (DASC), 25 - 29 September 2016, Sacramento, CA, USA*, IEEE, pp. 1–8.

Ragesh, R., Ratnoo, A. and Ghose, D. (2016). Decoy launch envelopes for survivability in an interceptor–target engagement, *Journal of Guidance, Control, and Dynamics* **39**(3): 667–676.

Rahimian, M. A. and Tavazoei, M. S. (2014). Improving integral square error performance with implementable fractional-order PI controllers, *Optimal Control Applications and Methods* **35**(3): 303–323.

Ramaswamy, S., Vaitekunas, D. A., Gunter, W. H. and February, F. J. (2017). Improvements to the ShipIR/NTCS adaptive track gate algorithm and 3D flare particle model, *in* G. C. Holst and K. A. Krapels (eds), *Infrared Imaging Systems: Design, Analysis, Modeling, and Testing XXVIII, 3 May2017, Anaheim, CA, USA*, Vol. 10178, International Society for Optics and Photonics, pp. 77–88.

Ren, W., Sloderbeck, M., Steurer, M., Dinavahi, V., Noda, T., Filizadeh, S., Chevrefils, A. R., Matar, M., Iravani, R., Dufour, C., Belanger, J., Faruque, M. O., Strunz, K. and Martinez, J. A. (2011). Interfacing issues in real-time digital simulators, *IEEE Transactions on Power Delivery* **26**(2): 1221–1230.

Reynoso-Meza, G., Sanchis, J., Blasco, X. and Freire, R. Z. (2016). Evolutionary multi-objective optimisation with preferences for multivariable PI controller tuning, *Expert Systems with Applications* **51**: 120–133.

Robinzon, R., Motovilov, D., Mangoubi, S. and Ben-David, E. (1993). Infrared scene generator for a

flight-motion simulator, *in* B. F. Andresen and F. D. Shepherd (eds), *Infrared Technology XIX, 1 November 1993, San Diego, CA, USA*, Vol. 2020 of *SPIE's 1993 International Symposium on Optics, Imaging and Instrumentation*, International Society for Optics and Photonics, pp. 150–160.

Rugh, W. J. and Shamma, J. S. (2000). Research on gain scheduling, *Automatica* **36**(10): 1401–1425.

Rusnak, I., Hertz, O. and Dana, Y. (2016). Real-time implementation of simple adaptive control algorithm to two axes gimbal, *2016 IEEE International Conference on the Science of Electrical Engineering (ICSEE), 16 - 18 November 2016, Eilat, Israel*, IEEE, pp. 1–5.

Schildkraut, E., Flanagan, J. A., Lewis, H. and Dillon, J. E. (1988). A generalized IR Scene Simulator (IRSS) for dynamic, hardware-in-the-loop testing, *in* R. B. Johnson and M. J. Triplett (eds), *Infrared Scene Simulation: Systems, Requirements, Calibration, Devices, and Modeling, 14 July 1988, Orlando, FL, USA*, Vol. 940 of *1988 Technical Symposium on Optics, Electro-Optics, and Sensors*, International Society for Optics and Photonics, pp. 73–79.

Short, M. and Pont, M. J. (2008). Assessment of high-integrity embedded automotive control systems using hardware in the loop simulation, *Journal of Systems and Software* **81**(7): 1163–1183.

Shrivastva, V. and Singh, R. (2014). Performance analysis of speed control of direct current (dc) motor using traditional tuning controller, *International Journal of Emerging Technology and Advanced Engineering (IJETAE)* **4**(5): 119–125.

Sidery, C. J. and Pyle, A. (2001). Facility for testing infrared imaging seekers in a countermeasures environment, *in* R. L. Murrer Jr. (ed.), *Technologies for Synthetic Environments: Hardware-in-the-Loop Testing VI, 31 August 2001, Orlando, FL, USA*, Vol. 4366 of *Aerospace/Defence Sensing, Simulation, and Controls*, International Society for Optics and Photonics, pp. 54–64.

Skogestad, S. and Postlethwaite, I. (2007). *Multivariable feedback control: analysis and design*, Vol. 2, Citeseer.

Stevanovic, A., Abdel-Rahim, A., Zlatkovic, M. and Amin, E. (2009). Microscopic modeling of traffic

signal operations: Comparative evaluation of hardware-in-the-loop and software-in-the-loop simulations, *Transportation Research Record* **2128**(1): 143–151.

Stinean, A.-I., Preitl, S., Precup, R.-E., Dragos, C.-A., Petriu, E. M. and Radac, M. (2013). Choosing a proper control structure for a mechatronic system with variable parameters, *IFAC Proceedings Volume* **46**(6): 23–31.

Tepljakov, A., Gonzalez, E. A., Petlenkov, E., Belikov, J., Monje, C. A. and Petráš, I. (2016). Incorporation of fractional-order dynamics into an existing PI/PID dc motor control loop, *ISA Transactions* **60**: 262–273.

Toothman, H. and Loughmiller, C. M. (1971). F-4B and F-8 Flare Effectiveness Against the ATOLL Missile (AA-2), *Technical report*, Naval Research Lab Washington DC, Fort Belvoir.

Van der Auweraer, H., Anthonis, J., De Bruyne, S. and Leuridan, J. (2013). Virtual engineering at work: the challenges for designing mechatronic products, *Engineering with Computers* **29**(3): 389–408.

Virgala, I., Frankovsky, P. and Kenderova, M. (2013). Friction effect analysis of a dc motor, *American Journal of Mechanical Engineering* **1**(1): 1–5.

Wein, S. J., Targove, J. D., Menikoff, A., Bowler, D. P. and Korwan, D. J. (2011). High accuracy optical pointing apparatus. US Patent 7.894.144.

Willers, M. S. and Willers, C. J. (2012). Key considerations in infrared simulations of the missile-aircraft engagement, *in* D. H. Titterton and M. A. Richardson (eds), *Technologies for Optical Countermeasures IX, 8 November 2012, Edinburgh, UK*, Vol. 8543 of *SPIE Security and Defence*, International Society for Optics and Photonics, pp. 180–195.

Wolff, S. (2013). *Methodological Guidelines for Modelling and Design of Embedded Systems*, PhD thesis, Aarhus University, Aarhus, Denmark.

Wu, Y., Lu, H., Zhao, F. and Zhang, Z. (2016). Simulation of the infrared signature of exo-atmosphere micro-motion object, *2016 Progress in Electromagnetic Research Symposium (PIERS), 8 - 10*

August 2016, Shanghai, China, IEEE, Shanghai, China, pp. 500–504.

Xu, X., Li, G., Yang, M., Ju, R. and Huang, K. (2016). Towards the integration of engagement and engineering-level simulation over real-time and heterogeneous systems, *Concurrency and Computation: Practice and Experience* **28**(12): 3390–3408.

Xue, D. and Li, T. (2018). An approach to design controllers for MIMO fractional-order plants based on parameter optimization algorithm, *ISA Transactions* **82**: 145–152.

Yan, W., Wang, D., Jia, P. and Li, W. (2012). The PWM speed regulation of dc motor based on intelligent control, *Systems Engineering Procedia* **3**: 259–267.

Yassine, Y., Messaoud, B. and Sofiane, M. (2015). Comparative analysis of single and double PI speed controlled dc drive performance improvement using Mini-Max approach, *2015 4th International Conference on Electrical Engineering (ICEE), 13 - 15 December 2015, Bourmedes, Algeria*, IEEE, pp. 1–4.

Zaki, A. M., El-Bardini, M., Soliman, F. and Sharaf, M. M. (2018). Embedded two level direct adaptive fuzzy controller for dc motor speed control, *Ain Shams Engineering Journal* **9**(1): 65–75.

Zaky, M. S. (2015). A self-tuning PI controller for the speed control of electrical motor drives, *Electric Power Systems Research* **119**: 293–303.

Zhang, J., Jia, G., Mkumbuzi, S. G. and Wu, Y. (2020). Dynamic aerothermal analysis of a cone-cylinder flight body, *International Journal of Aerospace Engineering* **2020**(1): 1–10.

Zhang, Y., Li, S., Luo, X. and Shang, M. (2017). A dynamic neural controller for adaptive optimal control of permanent magnet dc motors, *2017 International Joint Conference on Neural Networks (IJCNN), 14 - 19 May 2017, Anchorage, AK, USA*, IEEE, pp. 839–844.

Zhou, Y., Wang, Q., Li, T. and Hu, H. (2017). A numerical simulation method for aircraft infrared imaging, *Infrared Physics & Technology* **83**(1): 68–77.